RADIO FREQUENCY PULSED SIGNAL TRANSMITTER UTILIZING RADIOISOTOPE-POWERED SELF-TRIGGERED ELECTROSTATIC DISCHARGE SYSTEM

A Dissertation

Presented to the Faculty of the Graduate School

of Cornell University

in Partial Fulfillment of the Requirements for the Degree of

Doctor of Philosophy

by

Steven Tin

January 2012

RADIO FREQUENCY PULSED SIGNAL TRANSMITTER UTILIZING RADIOISOTOPE-POWERED SELF-TRIGGERED ELECTROSTATIC DISCHARGE SYSTEM

Steven Tin, Ph.D.

Cornell University 2012

A critical requirement for the success of autonomous remote systems is the realization of miniature power sources with long lifetimes, especially for sensor networks working in harsh, inaccessible environments where battery replacement would be expensive or impossible. Applications include environmental monitoring, civil infrastructure health monitoring, and implantable medical devices such as pacemakers and intra cranial implants. To achieve high-energy long-lifetime miniature power sources, we need to use fuels with high energy density that can perform reliably in harsh environments.

Low energy beta radioisotopes such as Nickel-63, Promethium-147 have energy density several orders of magnitude higher than electrochemical, lithium-ion, and hydrocarbon fuels, and their emitted electrons can be easily shielded with low radiation and chemical risks. Furthermore, the radiation process is independent of the surrounding environment, which makes it a great candidate to power device working in harsh environments. The choice of the radioisotope depends on the application requirements. In this dissertation, since we are focused on long term sensing applications, we will focus our studies on Nickel-63, which has a half life of 100.2 years.

For remote wireless sensing and communication applications, continuous signal transmission is often not required with data acquisition once every minute or over

longer durations is sufficient. However, RF power ranging from 1mW to hundreds of mW is required for signal transmission to reach receiver that maybe located at distant places. Furthermore, we need to use minimum amount of Nickel-63 for both cost and safety reasons. To achieve both requirements, a pulsed power generating system is designed and implemented. In the system, inside a vacuum chamber, a conducting cantilever is placed above a Nickel-63 radioactive source. As the emitted electrons are collected on the cantilever charging it with negative charge, the Nickel-63 source gets positively charged. As the voltage across the gap increases,the cantilever is pulled toward the source. Electrostatic discharge occurs when the electric field across the gap exceed the break down limit. Although the cantilever pull down process can take several minutes, the discharge process occurs in nanoseconds. A pulsed power amplification is thus achieved. With 1.5mCi input, output RF signal with hundreds of milliwatts have been demonstrated.

The pulsed RF power generator is further characterized both theoretically and experimental to achieve the application-determined output RF frequency and power. The RF frequency is found to be determined with the equivalent capacitance and inductance of the system. A capacitive humidity sensor is integrated with system, and a fully self-powered wireless humidity sensor node with decades of life time was demonstrated with ambient humidity level coded in the output RF signal. To have a high quality factor RF signal with well-defined frequency for long distance wireless RF communication, a surface acoustic wave (SAW) resonator is integrated into the system as a frequency selector, and RF output signal with equivalent quality factor over 1000 have been demonstrated.

For applications that requires decades of continuous power, this dissertation also reports on an 11.2% ultra-high efficiency 50um-thick thinned-down silicon carbide betavoltaics under (Nickel-63 irradiation. The efficiency can be further

increased to 23.6%, while the device thickness can be decreased to below 30um. Comparing to the best SiC betavoltaics reported so far, our devices have an efficiency improvement of 3-4X, with a fuel fill factor improvement of 8-10X, which will lead to an overall power density improvement of 30-40X. Comparing to the best available planar silicon betavoltaics, our devices have power density improvements of 100X (6X in efficiency, and 16X improvement in fuel fill factor.)

BIOGRAPHICAL SKETCH

Steven Tin was born and brought up in Shandong, China. He studied engineering at City College of San Francisco and University of California, Davis. In 2004, he received his Bachelor's degree in electrical engineering with high honors from Davis. In the same year, he entered Cornell University to pursue Ph.D. degree in electrical engineering.

To my parents

For all the love and support

ACKNOWLEDGEMENTS

It is impossible for us to accomplish anything by ourselves alone. We move forward by building on other people's prior works with the guidance and help of our mentors, colleagues, and friends. I cannot reach this point without all their helps.

First and for most, I want to express my deepest gratitude and appreciation to my advisor, Professor Amit Lal, for all his patience, support, and guidance both in academics and in life. It is his optimistic attitude and continuous innovative visions that inspires me and drives my research project forward. I would be the first to admit it has been a long process not without many struggles. It is Professor Lal's patience and guidance through those struggles that makes me a better researcher and more evened person. I also grateful to Professor Sunil Bhave and Professor Cliff Pollock for serving on my committee and for the knowledge and advises they have offered.

I want to thank all my previous and current colleagues for their friendship, help, and collaboration. It was from all those last-night working together and heated discussions that I have learned the most. In particular, I would like to thank Rajesh Duggirala, Janet Shen, Yue Shi, Nori Yoshimizu, Abihishek Ramkumar, Alper Bozkurt, Siva Pulla, Yueru Lu, Hui Li, Serhan Ardanuc, Kusard Araz, Shankar Radhakrishnan, Kwame Amponsah, Hadi Hosseinzadegan, Savarni Piratla, Hengky Chandrahalim, Shyi-Herng Kan, Abhijit Sathaye, and Xi Chen.

Last but not least, I want to thank all the friends I have gotten the pleasure to know in Ithaca for all the wonderful memories.

TABLE OF CONTENTS

Biographical Sketch . . . iii
Dedication . . . iv
Acknowledgements . . . v
Table of Contents . . . vi
List of Figures . . . ix
List of Tables . . . xiv

1 Overview of Radioisotope Power Generation 1
1.1 Energy Density of Different Fuels . . . 1
1.2 Radioisotopes for Micro Power Generation . . . 2
1.2.1 Safety of Radioisotope Fuels [12] . . . 3
1.2.2 Low Energy β-emitters . . . 4
1.3 ^{63}Ni Radioactive Decay Energy Conversion . . . 5
1.4 Outline of the thesis . . . 5

2 Radioisotope-Powered Self-Triggered Electrostatic Discharge System 8
2.1 Introduction . . . 8
2.2 Radioactive powered discharge system . . . 9
2.3 Study of cantilever pull down process . . . 11
2.3.1 Voltage-controlled cantilever actuation . . . 12
2.3.2 Ideal charge-controlled cantilever actuation . . . 13
2.3.3 Charge-controlled cantilever actuation with parasitic capacitance . . . 18
2.3.4 Charge leakage in the system . . . 23
2.3.5 Energy conversion in the pull-down process . . . 25
2.4 Vacuum electrostatic discharge conditions for radioisotope-powered system . . . 27
2.4.1 Introduction to electrostatic discharge . . . 28
2.5 Study of current and radiated electromagnetic field from radioisotope-powered electrostatic discharge system . . . 30
2.5.1 Electrostatic discharge Current . . . 32
2.5.2 Electromagnetic radiation from electrostatic discharge . . . 35
2.6 System implementation and simulation . . . 37
2.7 Testing of the radioactive powered discharge system . . . 39
2.8 Efficiency study of the radioactive powered discharge system . . . 40
2.9 Micro-fabricated discharge system . . . 42
2.10 Vacuum study of the radioactive powered discharge system . . . 45
2.10.1 Experiment Setup . . . 46
2.10.2 Experiment Results . . . 46
2.10.3 Radiation Current Measurement . . . 48

3 Radioisotope-Powered RFID and Sensors **52**
3.1 Introduction . . . 52
3.2 Radioisotope powered discharge system with external capacitances . 53
3.3 Radioactive powered wireless sensors . . . 55

4 SAW-Based Radioisotope-Powered RF Transponder **58**
4.1 Introduction . . . 58
4.2 Principle of operation . . . 59
4.3 Macro-size implementation and experimentally results . . . 62
4.4 Micro-size implementation and experimentally results . . . 63
4.5 Radioisotope-powered SAW sensor study . . . 66
4.6 Efficiency study of the integrated SAW RF transponder . . . 67

5 Ultrahigh Efficiency and Power Density Micromachined Thin Silicon-Carbide Betavoltaics **70**
5.1 Introduction . . . 70
5.2 Fabrication of SiC betavoltaics . . . 72
5.3 Experiment results of thinned-down betavoltaics . . . 74
5.4 Conclusion . . . 76

6 Microfabricated Ultrasonic Motor **78**
6.1 Introduction to the ultrasonic motor . . . 79
6.2 Fabrication of the ultrasonic micromotor . . . 79
6.3 Experimental setup . . . 80
6.4 Linear vibration of the stator . . . 82
6.5 Nonlinear vibration of the stator . . . 83
6.5.1 Optical Interferometer Measurement . . . 83
6.5.2 Direct Optical Measurement . . . 85
6.6 Experimental measurements of the micro ultrasonic motor . . . 86
6.7 Motor optimization study with various hub diameters . . . 89
6.8 Rotor with integrated mirrors . . . 91
6.9 Conclusion . . . 93

7 Carbon Materials Study for MEMS Applications **96**
7.1 Thin-Films of C60 . . . 96
7.1.1 Introduction . . . 96
7.1.2 Device Fabrication . . . 98
7.1.3 Experiment setup and results . . . 102
7.1.4 Conclusion . . . 106
7.2 Photoresist-Pyrolyzed Carbon Film . . . 106
7.2.1 Introduction . . . 107
7.2.2 Properties of pyrolyzed carbon thin films . . . 107
7.2.3 Experiment setup and results . . . 108

A Radioactive True Random Number Generator with Uniformly Distributed Integer Output **112**
A.1 Introduction . . . 112
A.2 Uniformly distributed random numbers from a Poisson Process . . . 114
A.3 Design and implementation of radioactive TRNG . . . 117
A.4 Results and discussion . . . 118
A.4.1 Uniformity test . . . 118
A.5 Conclusions . . . 120

B Integratable Zero-Power Voltage Bias for Sensor Applications **122**
B.1 Design and Analysis . . . 122
B.2 Fabrication and Testing . . . 125
B.3 Conclusion . . . 129

Bibliography **130**

LIST OF FIGURES

1.1 Illustration of radioactive-to-electrical energy conversion mechanisms for ^{63}Ni 6

2.1 Schematic illustrating the sensor nodes operating in harsh and inaccessible environments 9
2.2 Schematic illustrating the working principle of a pulsed-power generator 10
2.3 Schematic illustrating the radioisotope actuated reciprocation of metal cantilevers 11
2.4 Voltage-controlled actuation model of the discharge system 12
2.5 Normalized voltage needed for normalized displacement with voltage-controlled pull down 14
2.6 Charge-controlled actuation model of the discharge system 15
2.7 Normalized cantilever displacement (with respect to initial gap)versus normalized charge time (with respect to pull-down time) 16
2.8 Normalized charge across the gap during cantilever pull-down versus its normalized displacement 16
2.9 Relative voltage across the gap during cantilever pull-down versus its displacement 18
2.10 Charge-controlled actuation model of the discharge system with parasitic capacitances 19
2.11 Normalized charge across the gap during cantilever pull-down versus its normalized displacement 21
2.12 Normalized time required for cantilever to be pulled down to a normalized displacement with various parasitic capacitors 22
2.13 Charge-controlled actuation model of the discharge system with parasitic capacitances and leakage current 23
2.14 The electrostatic energy stored in gap capacitor and parasitic capacitor, and the potential energy stored in the cantilever with respect to the normal displacement 26
2.15 Electric field versus cantilever pull-down displacement with 500μm initial gap 28
2.16 Schematic illustrating the significance of the surface and avalanche process [27] 30
2.17 Typical waveform of the output current of the ESD generator . . . 31
2.18 Schematic illustrating the moving cantilever in the discharge system 34
2.19 Photograph of the self-powered wireless discharge system 38
2.20 (a)schematic, and (b) equivalent LC circuit of the self-powered wireless discharge system 38
2.21 Magnitude and frequency of the remotely detected RF signal of the arc discharge system 40

2.22 Resonance response of the arc discharge system from SPICE simulation and experimental measurement 41
2.23 Measured pull-in time of the discharge system at different gap sizes 42
2.24 Measured discharge system output energy at different gap sizes at 320MHz 43
2.25 Schematic illustrating the integration and packaging of the micro-RF transmitter 43
2.26 (a) Fabrication process and (b) photo of the microfabricated RF transmitter 44
2.27 Waveform and frequency of the RF signal from a transmitter with 5mm long cantilever 45
2.28 Schematic illustrating the testing setup for the discharge system with 47pF load capacitor and antenna connected to cantilever output with vacuum controlled by leak valve 47
2.29 Experimental RF signal output of the discharge system with short electromagnetic radiation signal and pulse current induced LC signal at 306.5MHz 48
2.30 Reciprocation period of the system at different vacuum levels. Multiple data points are recorded at each vacuum level 49
2.31 Schematic illustrating the discharge mechanisms of the vacuum breakdown at different vacuum levels [43] 50
2.32 Schematic illustrating the testing setup for the radiation current measurement with a high impedance current meter(Keithley 2400) 50
2.33 Experimental measurement of radiation current at under different vacuum condition with a 1.5mCi source 51

3.1 (a) Photograph, (b) equivalent LC circuit of the self-powered wireless discharge system with external capacitance 54
3.2 Magnitude and frequency of the remotely detected RF signal with 20pF external capacitance wireless RF sensor node 54
3.3 Resonance response of system with 20pF external capacitor from SPICE simulation and experimental measurement 55
3.4 Experimental and simulated RF signal frequency with different external capacitance 56
3.5 Measured humidity sensor capacitance at different relative humidity levels 57
3.6 Measured remotely detected RF signal frequency at different relative humidity levels 57

4.1 Schematic illustrating operation principle of the SAW-based radioisotope-powered RF transponder 60
4.2 The equivalent circuit model of the SAW transponder 61
4.3 Photograph of the prototype radioisotope-powered SAW transponder 62

4.4 Measured RF signal waveform with 315MHz SAW resonator connected . . . 63
4.5 Frequency of the RF signal with 315MHz Saw resonator connected 64
4.6 Bandpass-filtered signals illustrating the SAW resonator signal delay 64
4.7 Photograph of the microfabricated integrated RFID device inside a 1 inch^2 vacuum package . . . 65
4.8 Schematic illustrating the measurement set for the RF signals from SAW and discharge system . . . 66
4.9 RF discharge signal measured at the discharge cantilever compared to the signal from the SAW devices show a 750ns SAW delay . . . 67
4.10 Schematic illustrating the SAW resonator with mass-loading between input port and one of the output ports . . . 68
4.11 Measured RF signal frequencies at both output ports of the SAW resonator whose resonant frequency is about 100MHz . . . 68

5.1 Schematics illustrating the design and advantages of the thin SiC betavoltaic design . . . 72
5.2 Fabrication Process of the thin SiC betavoltaics . . . 73
5.3 Measured IV characteristic of regular-thickness SiC betavoltaic under ^{63}Ni electron irradiation . . . 74
5.4 Measured conversion efficiency and EHPs multiplication factor at different input electron energy for the regular-thickness device . . . 76
5.5 Photograph and measured IV characteristic of 50μ m-thick SiC betavoltaic under ^{63}Ni electron irradiation . . . 77

6.1 Schematic illustrating the ultrasonic micromotor with optical and sensing components integrated on the rotor for directional sensing and communication . . . 80
6.2 (a) Photo of the micromotor (b) Cross section view of the motor measurement setup . . . 81
6.3 Schematic illustrating the energy transfer in the ultrasonic motor actuation process . . . 83
6.4 Measured impedance of the PZT plate with and without silicon die attached on the bottom, demonstrating the thickness mode at around 4 MHz . . . 84
6.5 (a) Simulated and (b) measured vibrated mode of a micromotor with 820μm stator actuated at 3.78MHz . . . 84
6.6 Waveform and frequency of the subharmonic signal for the stator with 820μm diameter while PZT is actuated at 3.78MHz . . . 86
6.7 (a) Mode shape at 3.78MHz actuation frequency when nonlinear vibration exists (b) Mode shape at 1.78 MHz subharmonic frequency, (c) Mode shape at 2 MHz subharmonic frequency (d) Simulated mode stator mode shape at 2.0 MHz . . . 87

6.8 Optical image of (a) (5,1) linear vibration mode shape, (b) (c) (1,13) nonlinear traveling wave mode shape. (d) Finite element simulation of mode shape at 1.78 MHz 88
6.9 Rotation speed of the prototype motor at different actuation voltages. Motor actuated at 3.78 MHz 89
6.10 Rotation angle of the motor actuated by 3.78MHz sinusoidal signal bursts with various number of sinusoidal cycles. Rotation accuracy of 0.1 degree is achieved 90
6.11 (5, 1) mode resonant frequencies for motors with different stator sizes 92
6.12 Subharmonic frequencies of the motors with different stator diameters 92
6.13 Measured rotation speed vs. excitation voltage for motors with varies stator sizes 93
6.14 Optical image of a micro-ultrasonic motor integrated with reflective mirrors on the rotor, (a) mirrors down, (b) mirrors up and locked in place 94
6.15 The vibration amplitude of the 585μm stator driven at different frequencies, and the modal shape of the stator driven around 600kHz while the motor is rotating 94

7.1 This figure shows the ordering of C60 molecules onto silicon and germanium [62] 99
7.2 (a) Fabrication process (b) SEM images of the C60 clamped-clamped and clamped-free beams 101
7.3 Raman spectra of the C60 microstructure measured using Nanonics MV1000 102
7.4 Optically scanned3rd overtone mode shape, and the side view sketch of the C60 clamped-free cantilever motion 103
7.5 Mechanical motion spectra of the C60 cantilever (L=30m), and the substrate near it. Inset shows the expanded 3rd overtone mode with resonance frequency 1.12MHz, where the substrate motion is negligible 104
7.6 Experimentally measured C-60 cantilever3rd overtone mode resonant frequencies with different length 105
7.7 Experimentally measured C60 cantilever second-mode resonant frequencies as a function of (1/beam length)^2 106
7.8 Measurement of residue film thickness percentage at different pyrolyzation temperatures 108
7.9 Raman spectra of the pyrolyzed carbon film at different pyrolysis temperatures 109
7.10 Measured carbon film sheet resistance as a function of pyrolysis temperature 109
7.11 Measured carbon stress as a function of pyrolysis temperature . . . 110
7.12 SEM image and measured cantilever resonant frequency as a function of length 111

A.1 Illustration figure. 114
A.2 Arrival time illustration. 115
A.3 Block diagram for uniform random number generator. 117
A.4 (a) Radioactive decay pulse signal (b)Histogram of time intervals for 10000 samples for a radioactive source of average rate 27000 Hz . 118
A.5 Oscilloscope display of the random number system. 119
A.6 Output of the uniform number generator. 120

B.1 Radioactive DC bias diagram 123
B.2 Circuit model diagram 123
B.3 Circuit model diagram for two RVBs connected in series 124
B.4 Output voltage with oxide thicknesses of 50nm and 120nm 126
B.5 Output voltage of the radioactive bias with different oxide thickness 126
B.6 Output voltage for two devices connected in series 127
B.7 Output voltage for two devices connected in series 128
B.8 The V_{gs} -I_d characteristic of the transistor 128

LIST OF TABLES

1.1 Power densities of different batteries, fuels, and radioisotopes[6] [7] 2
1.2 Comparison of radiation properties of ^{3}H, ^{63}Ni, and ^{147}Pm[12] . . 4

2.1 power requirements of typical periodically sampling low power wireless sensor microsystems 9
2.2 Representation and values of R, L, C components in the equavilent circuit model in Figure 2.20(b) 39

4.1 Representations and values of R, L, C components in circuit model in Figure 4.2 61

7.1 Constants for Physical Interactions between C60 Molecules 97
7.2 Young's modulus and acoustic impedance of typical MEMS materials 98

CHAPTER 1

OVERVIEW OF RADIOISOTOPE POWER GENERATION

With the advancement of solid state and microelectromechanical systems (MEMS) technology, the size of sensing and actuation devices have been greatly reduced. To operate those devices, compact power supplies with long lifetime and high power density are required, to have a microsystem in which the power-supply does not dominate the volume. Traditional electrochemical batteries cannot meet the requirements due to their limited energy density. The implementation of radioisotope powered batteries are investigated utilizing the high energy density of radioisotopes. Different radioactive-decay energy to electrical energy conversion mechanisms are discussed in this chapter.

1.1 Energy Density of Different Fuels

A critical requirement for the success of autonomous remote systems is the realization of miniature power sources with long lifetimes, especially for sensor networks working in harsh, inaccessible environments where battery change would be expensive or impossible. Those applications include environmental monitoring [1, 2] civil infrastructure health monitoring [3], and implantable medical devices such as pacemakers [4] and intracranial implants [5]. To achieve high-energy long-lifetime miniature power sources, we need to use fuels with high energy density.

The energy densities of the different batteries, fuels, and radioisotopes are listed in Table 1.1 [6] [7]. For alkaline and lithium batteries, their power density is too low to be scaled down for long-term operations. Extensive efforts have been made to convert hydrogen or hydrocarbon fuels to electrical energy with micro fuel cells [8] [9] [10] and micro combustion engine [11]. However, those device are complicated to

Table 1.1: Power densities of different batteries, fuels, and radioisotopes[6] [7]

Fuel	Energy density (MJ/kg)
Alkaline battery	0.4-0.59
Lithium-ion battery	0.46-0.54
Methanol	19.7
Gasoline	46.4
Methane	55.6
Hydrogen	146
^{63}Ni	10^4
^{210}Po	10^6

fabricate, and the hydrocarbon and hydrogen fuels cannot provide enough energy for long-lifetime applications without refueling. On the other hand, radioisotopes such as ^{63}Ni and ^{210}Po have energy density several order higher than hydrogen and hydrocarbons. They are therefore good candidates for long-lifetime micro power generation.

1.2 Radioisotopes for Micro Power Generation

When radioisotopes are used to power micro power generators, it is very important to ensure all the radioactive elements are contained within the packages. For radioisotopes emitting high energy particles, thick shields will be needed to keep it safe, which will significantly increase the volume of the device. The potential risk due to leakage is also high. Therefore, to find the suitable radioisotope fuel for micro power generation, safety, power density, and half-life of the fuels need all to be considered.

1.2.1 Safety of Radioisotope Fuels [12]

The safety of radioisotope fuels can be evaluated using the following criteria: (1) penetration range of primary radiation; (2) generation of Bremsstrahlung secondary radiation during the stopping of primary radiation; (3) effusivity of the radioisotope source, if gaseous; (4) chemical toxicity, in case of release and ingestion or inhalation; and (5) security and non-proliferation standpoint.

Radioisotopes employed in terrestrial microsystems should ideally satisfy the following criteria: (1) minimal shielding should be required for stopping both the primary radiation and the resulting Bremsstrahlung; (2) radioisotope sources should not be prone to dispersal through effusion; and (3) they should not be chemically toxic. Given these requirements, radioisotopes emitting low energy ($E_{rad,avg} < 100keV$) β-radiation are particularly suitable for terrestrial microsystems. Low-energy β-radiation emitted with average energies can be shielded easily by thin ($< 100\mu m$) sheets of most metals, and the resulting Bremsstrahlung is very weak, as just $< 0.1\%$ of E_{rad} is converted into photons [13]. In contrast, β-radiation with average energies $E_{rad,avg} > 500keV$ is difficult to shield due to its considerable penetrating power arising from the low mass of electrons, and it generates significant Bremsstrahlung [14]. Additionally, even though α-radiation is easily shielded due to their large mass and ionized state, most α-radioisotopes also emit high penetration range γ radiation from the decay chain, are highly toxic chemically [13]. This makes large activities of α-radioisotopes unsuitable for widespread deployment in terrestrial applications. Furthermore, γ-radiation requires heavy shielding because of its high penetrating power [13], and hence makes γ-radioisotopes unsuitable for most terrestrial applications.

Table 1.2: Comparison of radiation properties of ^3H, ^{63}Ni, and ^{147}Pm[12]

Parameters	^3H	^{63}Ni	^{147}Pm
$E_{rad,avg}(keV)$	5.7	17.3	63.5
Half-life ($years$)	12.4	100.3	2.64
Highest available specific activity (Ci/cc)	500	133	4300

1.2.2 Low Energy β-emitters

As analyzed in the last section, low energy β-emitters would be the best choices for micro power generation. Tritium (^3H), Nickel-63 (^{63}Ni), and Promethium-147 (^{147}Pm) are the three most common lower β-emitters with their properties listed in Table 1.2. Other β-emitters with low energy include Sulfur-35 (^{35}S) with half life of only 87 day [15].

The choice of low energy β radioisotope sources depends on the application requirements. In this research, we are focusing on applications requires compact long lifetime power sources. ^3H has higher specific activity than ^{63}Ni with lower electron energy. However, because it is in either gas or liquid form, it is prone to dispersal by effusing through thin-layers of materials [16], which could cause undesirable long-term degradation of performance, and raise safety concerns about radiological leakage. ^{147}Pm has the highest specific activity, but its half-life is only 2.64 years, which is too short for long lifetime applications. Thin-film ^{63}Ni is well suited for long lifetime safe microsystems because of its $100year$ half-lifetime and its relative radiological and chemical safety. Thin-films of ^{63}Ni can be handled with minimal shielding requirements, because the average energy of the β-electrons emitted from ^{63}Ni is only $17.3keV$, which cannot even penetrate through the dead layer of human skin [13], and the resulting Bremsstrahlung is insignificant. Additionally, ^{63}Ni is not known to effuse out of thin-films even at temperatures as high as 400^oC. Consequently, it is employed in a variety of industrial applications including electron capture devices [17] [12].

1.3 ^{63}Ni Radioactive Decay Energy Conversion

^{63}Ni is a great candidate of fuel source for our targeted applications. However, for most cases, we cannot directly use the radioactive energy to power electrical devices. The energy stored in the emitted electrons from ^{63}Ni source needs to be converted into electrical energy. As shown in Figure 1.1, the radioactive-to-electrical energy conversion mechanisms traditionally including thermoelectric, direct charging, generation of electron-hole pairs or photons, etc. However, for ^{63}Ni, despite its high energy density, the power density is low due to its long half-life. With its low electron energy, a radioisotope thermoelectric generator would not be feasible. While direct-charging could potentially generate a high DC bias voltage, its applications are very limited. Secondary electron-hole pair generation or photon generation can only have a power output around $100nW/mCi$, which might be enough to maintain charges in sleep mode for some applications, not enough for other functionalities. To completely power remote sensing/communication devices, i.e., RF sensors and RFIDs, we need to somehow achieve energy integration, hence power amplification.

1.4 Outline of the thesis

In chapter 2, the mechanism to generate the power amplification is discussed in details both theoretically and experimental with electrostatic discharge based pulse power generation.

In chapter 3, utilizing the pulse power generator, an active wireless sensor node completely powered by radioactive thin-film is demonstrated, which can transmit an RF signal coded with the environmental information gathered by a passive capacitive sensor.

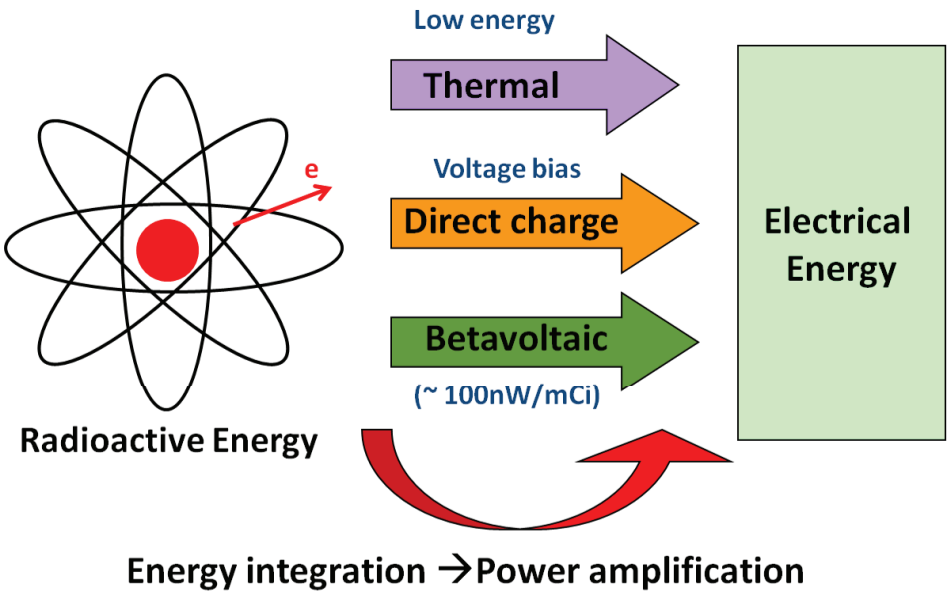

Figure 1.1: Illustration of radioactive-to-electrical energy conversion mechanisms for ^{63}Ni

In chapter 4, integrating a high quality factor SAW resonator with the discharge system, a wireless RFID/RF sensor with well-defined frequency for long distance communication is studied and demonstrated.

In chapter 5, high power density, high efficiency SiC betavoltaics are demonstrated for applications that requires continuous power supply.

In chapter 6, we looked into low power signal phase drive ultrasonically driven MEMS micromotors. In this thesis, we were able to demonstrate direct optical visualization of rotating whispering gallery modes. The motors have potential applications in directional sensing and directional communications.

In chapter 7, carbon materials (Pyrolyzed carbon and C60) are explored for applications in RF MEMS to reduce the actuation voltage and stiction.

In appendix A, ^{63}Ni radioactive decays are used as random events to empower a uniform true random number generator.

In appendix B, ^{63}Ni source is utilized to generate a scalable DC bias voltage across a insulating barrier.

CHAPTER 2

RADIOISOTOPE-POWERED SELF-TRIGGERED ELECTROSTATIC DISCHARGE SYSTEM

Inside a vacuum chamber, a metal cantilever is placed above a ^{63}Ni source. Due to the electrostatic force created by electron accumulation on the beam, the cantilever is pulled down and discharged. Radio-Frequency (RF) signal with hundreds of milliWatts of power is generated upon discharge. In this chapter, the mechanisms of the cantilever pull-down and RF signal generation are explored both theoretically and experimentally.

2.1 Introduction

For harsh and inaccessible environmental sensing and monitoring applications shown in Figure 2.1, the power requirements for a typical low-power wireless sensor node are 1-10 nW for retaining memory state, 0.1-1 mW for periodic sensing and processing, and 1-100 mW power for periodic wireless communication [18]. The power to retain memory state can be provide by betavoltaics as reported in [19] even with the low activity radioactive thin films presented here. Furthermore, MEMS radioisotope-powered piezoelectric power generator [20] can generate output power needed for periodic sensing and processing. In this chapter, we focus on the hundreds of milliWatts of radioactive RF power generation that can be used as a CMOS compatible wireless beacon and communications. With passive sensing components integrated to the discharge system, wireless sensors nodes can be powered entirely with thin films of low activity radioisotope.

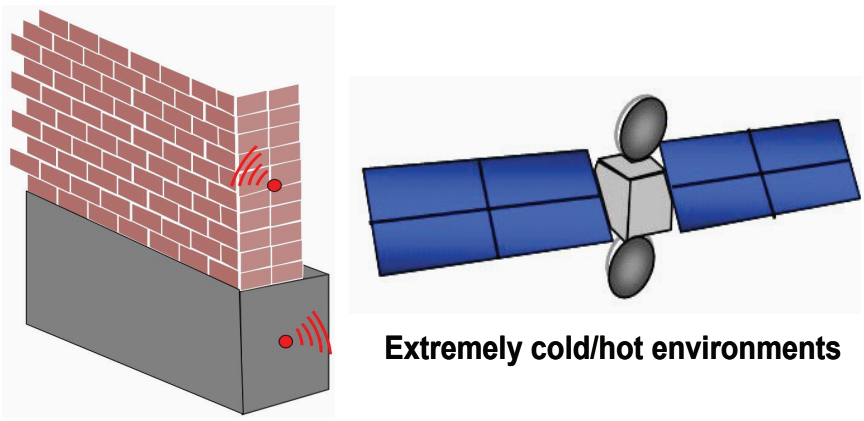

Figure 2.1: Schematic illustrating the sensor nodes operating in harsh and inaccessible environments

Table 2.1: power requirements of typical periodically sampling low power wireless sensor microsystems

Retaining memory state	1-10nW
Sensing/processing	0.1-1mW
Wireless communication	1-100mW

2.2 Radioactive powered discharge system

As mentioned in Chapter 1, to generated hundreds of milliWatts of RF power from nanoWatts of radioactive energy, an energy integration mechanism need to be implemented. A pulsed-power generator is a good candidate for energy integration (power amplification). As shown in Figure 2.2, in a pulsed power generator, an energy storage is charged up slowly with a low power source. Once the switch is activated, all the energy stored is released in a short time period. A large power amplification can thus be obtained. The energy can be stored either electrically, mechanically, or chemically.

For our application, a pulsed power generated is designed as illustrated in Figure 2.3. A metal cantilever is placed above a ^{63}Ni radioactive thin film with 1.5 mCi activity. Positive charges are accumulated on an electrically isolated

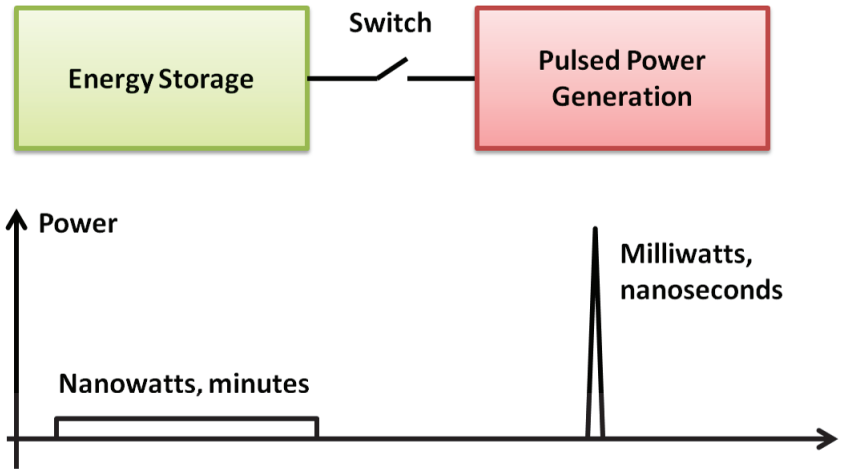

Figure 2.2: Schematic illustrating the working principle of a pulsed-power generator

^{63}Ni thin film due to the continuous emission of β-particles (electrons), which are collected on the metal cantilever. The accumulated charge increases with time, increasing the electrostatic force which eventually pulls the cantilever down towards the radioisotope thin-film. When the gap between the cantilever and radioactive source is small enough, arc discharge occurs through the gap. The energy stored is released, exciting the electrical components in the system, which results in an RF signal output. As the electrostatic force is eliminated, the beam oscillates mechanically and the process repeats itself. When the initial gap between the cantilever and the radioactive source is 500 μm, the pull-down cycle requires 3 minutes while the electrostatic discharge time is very short(<1ns). Therefore, the energy integrated over the reciprocation period is released in a very short time allowing us to greatly amplify the power from the radioactive source.

The entire radioactive power to RF power conversion process in the discharge

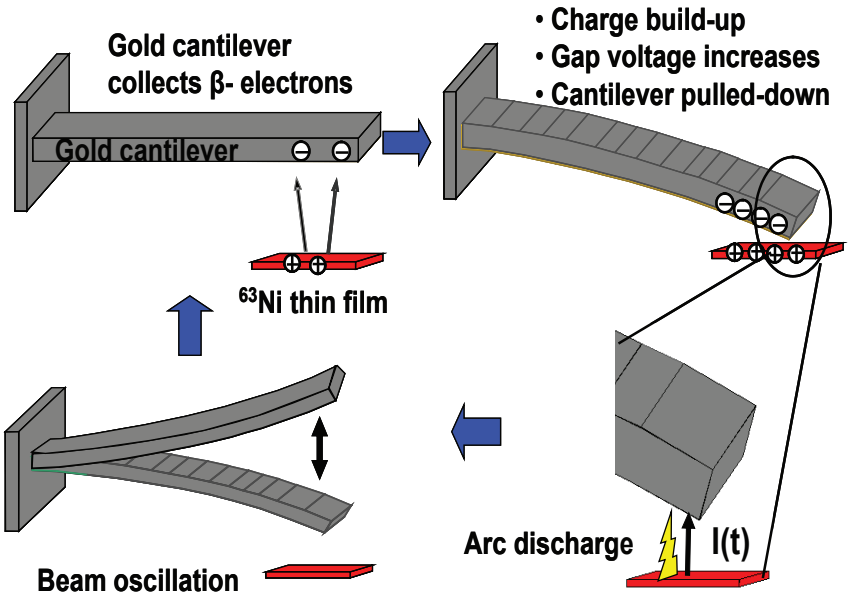

Figure 2.3: Schematic illustrating the radioisotope actuated reciprocation of metal cantilevers

system can be viewed as three sub-processes: cantilever pull-down process, electrostatic energy discharge process, and RF signal generation process. All these three processes will be discussed in details in the following sections for further understanding, modeling, and optimizing the system.

2.3 Study of cantilever pull down process

The cantilever in the discharge system is several millimeters long while the gap between the cantilever and the ^{63}Ni film is in the range of 100μm to 500μm. Therefore, to study the electrostatic force between the cantilever and the source, parallel plate capacitor approximation can be used [21][22][23]. The ^{63}Ni film is modeled as the fixed electrode, and the cantilever is the moving electrode. The system is driven by the ^{63}Ni-emitted electrons, which can be considered a current source. To better understand the relatively complicated charge-controlled cantilever actuation, we first analyze the simpler voltage-controlled system.

2.3.1 Voltage-controlled cantilever actuation

Assuming the system is actuated with a constant voltage, the discharge system can be modeled as in Figure 2.4, where m, k, and b are the mass, spring constant, and damping coefficient of the cantilever respectively. The cantilever and source has a initial gap of g_0 with a voltage of V applied across them. The cantilever moves in the direction of x. The forces acting in the system can be expressed as

$$m\ddot{x} + b\dot{x} + kx = \frac{1}{2}V^2\frac{dC}{dx} \tag{2.1}$$

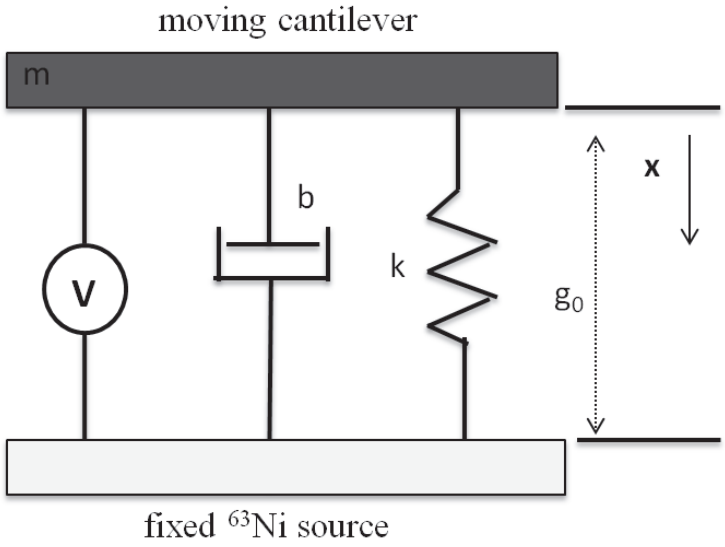

Figure 2.4: Voltage-controlled actuation model of the discharge system

The mechanical forces are on the right side of the equation while the electrostatic force is on the left side. Under equilibrium condition, where $\ddot{x}$=$\dot{x}$=0, Equation 2.1 can be simplified as

$$kx = \frac{1}{2}V^2\frac{dC}{dx} = \frac{1}{2}V^2\frac{\epsilon_0 A}{(g_0 - x)^2} \tag{2.2}$$

As shown in Equation 2.2, the mechanical restoring force increases linearly with the displacement, while the electrostatic force increases nonlinearly with the

displacement. For the cantilever pulling down process to stay stable, i.e., without pull-in, the increase rate of the electrostatic force must be slower than or equal to the increase rate of the mechanical force, in other words

$$\frac{d}{dx}[kx - \frac{1}{2}V^2\frac{\epsilon_0 A}{(g_0 - x)^2}] \geq 0 \tag{2.3}$$

Solving Equation 2.3, together with Equation 2.2, the pull-in gap and voltage are

$$g_{pi} = \frac{g_0}{3} \tag{2.4}$$

$$V_{pi} = \sqrt{\frac{8kg_0^2}{27c_0}} \tag{2.5}$$

where c_0 is the capacitance before applying voltage. As shown in Equation 2.4, the cantilever can only travel 1/3 of the gap before being pulled in.

To understand the relationship between voltage and displacement, Equation 2.3 can be rewritten as

$$\frac{V(x)}{V_{pi}} = \sqrt{\frac{27}{4}}\sqrt{\frac{x}{g_0}}(1 - \frac{x}{g_0}) \tag{2.6}$$

where $V(x)/V_{pi}$ is the voltage normalized to the pull-in voltage, and x/g_0 is the displacement normalized to the initial gap. Therefore, the normalized voltage needed for a normalized displacement is plotted in Figure 2.5. For every actuation voltage, there are two possible deflections, but the one beyond $g_0/3$ is unstable.

2.3.2 Ideal charge-controlled cantilever actuation

Since the discharge system is driven by the ^{63}Ni-emitted electrons, which is a current source rather than a voltage source, we have a charge-controlled system,

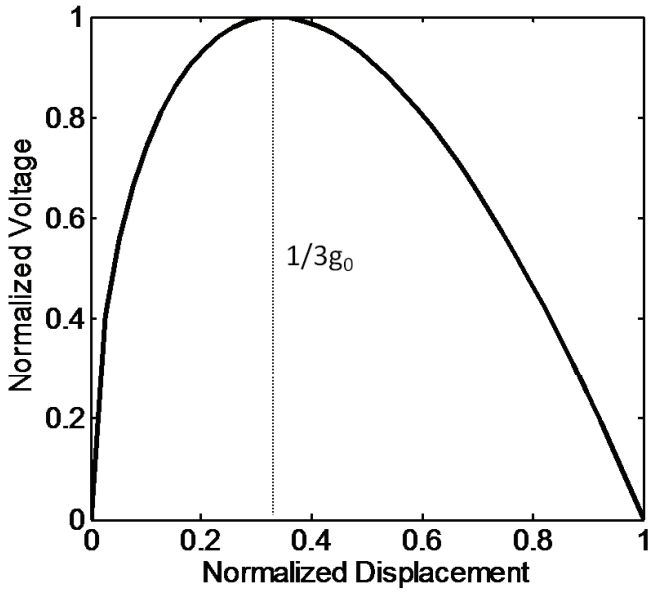

Figure 2.5: Normalized voltage needed for normalized displacement with voltage-controlled pull down

as illustrated in Figure 2.6 where i is radioisotope current and V is the voltage across the gap. For simplicity, in the section, let's assume there is no leakage current and parametric capacitance in the system, which means all the charges emitted are used to charge the parallel plate capacitor alone. The forces in the system can then be written as

$$m\ddot{x} + b\dot{x} + kx = \frac{Q^2}{2c_0 g_0} = \frac{Q^2}{2\epsilon_0 A} \tag{2.7}$$

As shown in Equation 2.7, the electrostatic force on the right side of the equation is independent of the gap. In equilibrium condition, the derivative of electrostatic force minus mechanical force is

$$\frac{d}{dx}(kx - \frac{Q^2}{2\epsilon_0 A}) = 1 \tag{2.8}$$

Therefore, the system is stable at any gap, and there is no pull-in for charge actuated cantilever. The cantilever travels the entire gap to reach the ^{63}Ni source.

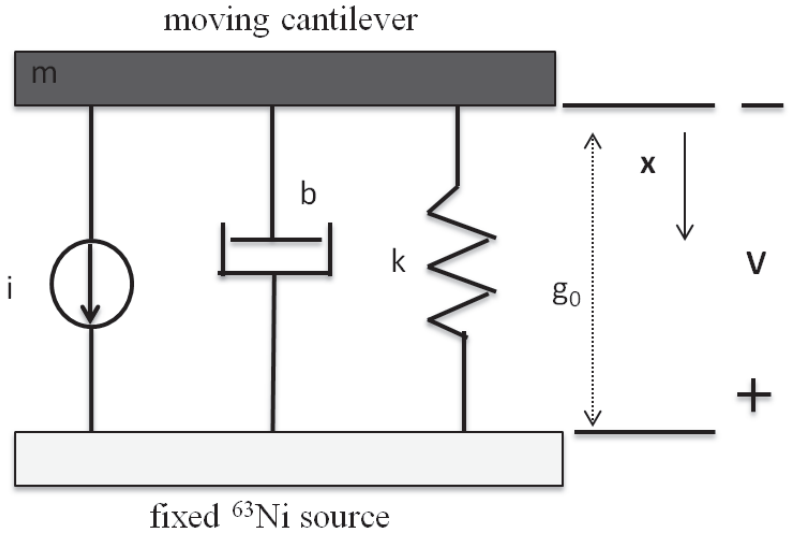

Figure 2.6: Charge-controlled actuation model of the discharge system

During the cantilever pull down process, the position of the beam at any given time can be calculated by substituting Q with it in Equation 2.7, which leads to

$$x = \frac{i^2 t^2}{2\epsilon_0 k A} \tag{2.9}$$

As illustrated in Figure 2.7, the displacement of the cantilever increases as a square of the charging time. The speed of the cantilever's movement increases with charging time. The time required for the cantilever to pull-down, which is the reciprocation cycle time in the discharge system, can be calculated as

$$T = \sqrt{\frac{2\epsilon_0 k A g_0}{i^2}} \tag{2.10}$$

Therefore, with all other conditions stay the same, the pull-down time in an ideal charge-controlled system increases with the square root of the gap . The total charge required to pull a cantilever down, which equals to the product of pull-down time and charging current, can be expressed as in Equation 2.11, which is independent of the current supply.

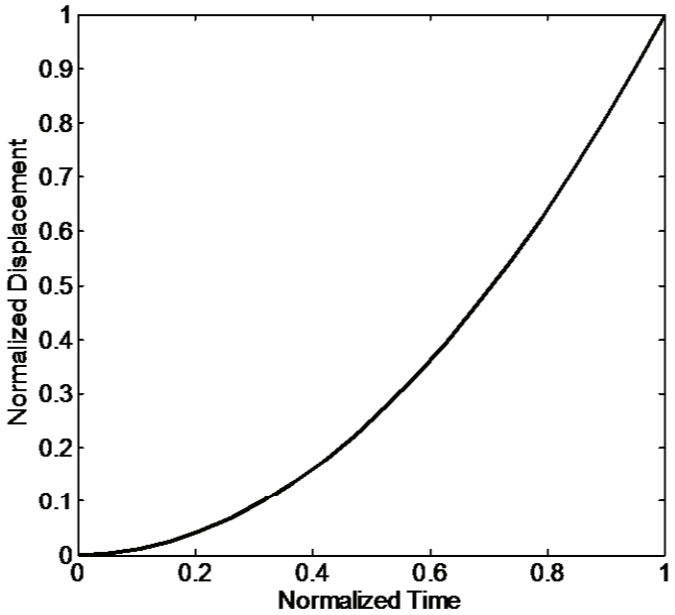

Figure 2.7: Normalized cantilever displacement (with respect to initial gap)versus normalized charge time (with respect to pull-down time)

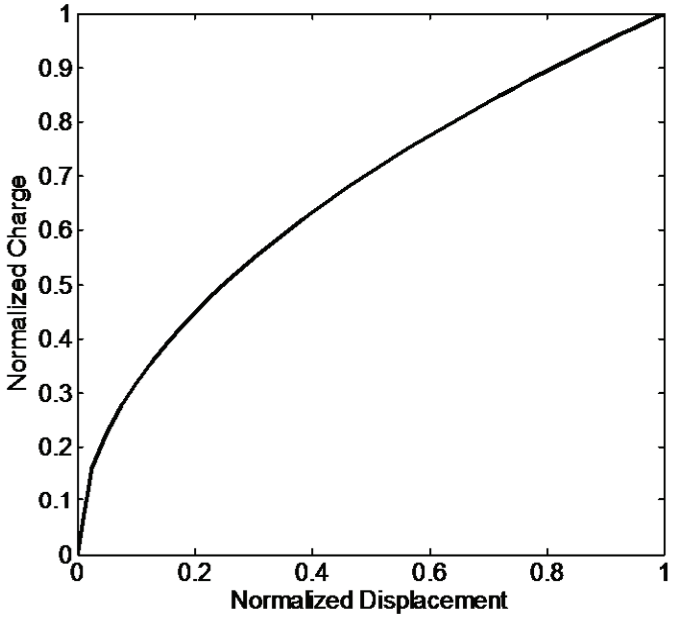

Figure 2.8: Normalized charge across the gap during cantilever pull-down versus its normalized displacement

$$Q = \sqrt{2\epsilon_0 k A g_0} \tag{2.11}$$

The amount of charge needed for a cantilever to reach a certain displacement is plotted in Figure 2.8 using Equation 2.11, with displacement and charge normalized to initial gap and pull-down charge respectively.

With the relationship between charge, capacitance, and displacement derived, the voltage across the gap as a function of the cantilever displacement is

$$V(x) = \frac{Q(x)}{c(x)} = \sqrt{\frac{2k}{\epsilon_0 A}}\sqrt{x}(g_0 - x) \tag{2.12}$$

Equation 2.12 is plotted in Figure 2.9, the voltage first increases with the displacement because the percentage rate of the charge increase is more than that of the capacitance increase. However, as the cantilever pull-down velocity increases with the displacement, the capacitance increase rate catches up and dominates, which results in a decrease of the voltage after an optimal displacement. The maximum voltage is achieved with the displacement of $g_0/3$. Although similar to voltage pull-down shown in Figure 2.5, every voltage has two different possible deflections, they correspond to different input charge levels (Figure 2.8). The maximum voltage can be expressed as

$$V_{max} = \sqrt{\frac{8kg_0^2}{27c_0}} \tag{2.13}$$

The spring constant of a cantilever is

$$k = \frac{Ewt^3}{4l^3} \tag{2.14}$$

where E is the Young's modulus of the cantilever material, w, t, and l are the width, thickness, and length of the cantilever respectively. Substituting Equation 2.14 into Equation 2.13, we get

$$V_{max} = \sqrt{\frac{2Et^3g_0^3}{27\epsilon_0 l_0 l^3}} \tag{2.15}$$

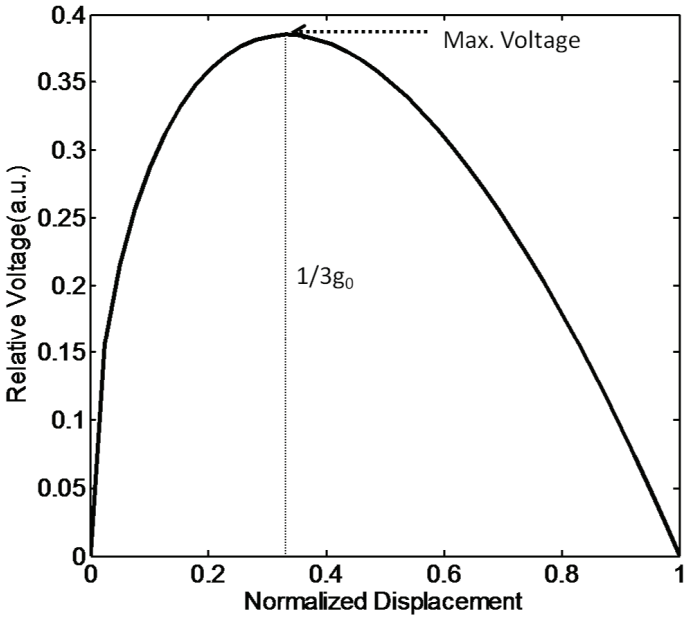

Figure 2.9: Relative voltage across the gap during cantilever pull-down versus its displacement

where l_0 is the overlap length between the cantilever the the bottom electrode. For a gold cantilever with Young's modulus, thickness, and length of $79GPa$, 300μm, and $5cm$ respectively, with overlap length of $7mm$, the maximum voltage is $2kV$ for 500μm gap and $4.5kV$ for $1mm$ gap.

2.3.3 Charge-controlled cantilever actuation with parasitic capacitance

In the previous section, we assume all the charges from the current source accumulate across the cantilever-radioisotope capacitor. However, in practice, there are parasitic capacitance between radioactive source and chamber wall, cantilever with chamber wall, etc. To accurately study the discharge system, in this section, we study the effects of the parasitic capacitance on cantilever charging and pull-down process. As shown in Figure 2.10, the parametric capacitance is modeled

in parallel with the gap capacitance C_p. Equation 2.7 can be modified as:

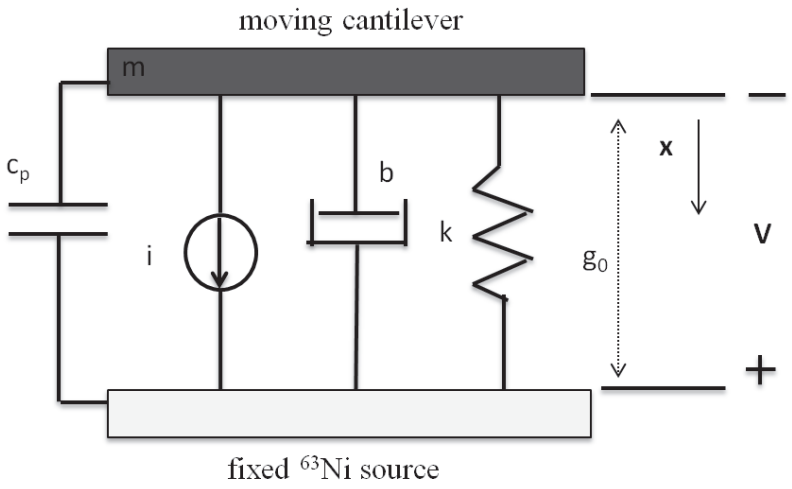

Figure 2.10: Charge-controlled actuation model of the discharge system with parasitic capacitances

$$m\ddot{x} + b\dot{x} + kx = \frac{Q_g^2}{2c_0 g_0} = \frac{Q_g^2}{2\epsilon_0 A} \tag{2.16}$$

The radioisotope-emitted current is charging up both the gap capacitance and the parasitic capacitance. The current can therefore written as

$$i = \frac{dQ_g}{dt} + c_p \frac{dV}{dt} \tag{2.17}$$

where Q_g is the charge across the cantilever radioactive source gap, and Q is the total charge in the system. Integrating Equation 2.17 over time, we can get

$$Q = Q_g + Q_g \frac{c_p}{c_0}(1 - \frac{x}{g_0}) \tag{2.18}$$

Equation 2.18 can be rearranged as

$$Q_g = \frac{Q}{1 + \frac{c_p}{c_0}(1 - \frac{x}{g_0})} \tag{2.19}$$

When the system is in the steady state condition, Equation 2.16 can be simplified as

$$kx = \frac{Q_g^2}{2\epsilon_0 A} \tag{2.20}$$

As mentioned in previous sections, for the system to be stable, the derivative of the mechanical force minus electrostatic force needs to be non-negative, which means

$$\frac{d}{dx}(kx - \frac{Q_g^2}{2\epsilon_0 A}) \geq 0 \tag{2.21}$$

Solving Equation 2.21 by substituting in Equation 2.19 and Equation 2.20, we get

$$x \leq \frac{g_0}{3}(1 + \frac{c_0}{c_p}) \tag{2.22}$$

From Equation 2.22, the pull-in conditions of the charge-controlled system with parasitic capacitance can be summarized as follows:

- If $c_p < c_0/2$, $x_{pi} > g_0$, there is no pull-in
- If $c_p = c_0/2$, $x_{pi} = g_0$, pull-in at 0 gap
- If $c_p >> c_0$, pull-in at $2g_0/3$

Even with parasitic capacitors, the charge-controlled cantilever has a pull-down range of $g_0/3$ to g_0 before being pulled in, which is bigger than the $g_0/3$ pull down range in voltage-controlled system.

In the pull down process, the total charge in the system as a function of the displacement can be derived from Equation 2.19 and Equation 2.20 to be

$$Q(x) = \sqrt{2k\epsilon_0 A g_0}\sqrt{\frac{x}{g_0}}[1 + \frac{c_p}{c_0}(1 - \frac{x}{g_0})] \tag{2.23}$$

With displacement normalized to the gap g_0, and charge normalized to the charge needed to pull down a cantilever as shown in Equation 2.11, the charge is plotted with different parasitic capacitance values.

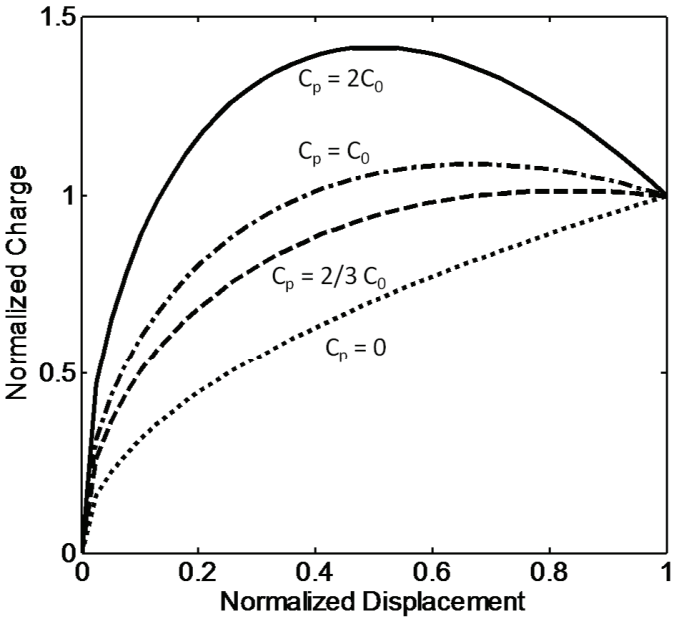

Figure 2.11: Normalized charge across the gap during cantilever pull-down versus its normalized displacement

As shown in Figure 2.11, the charge needed at pull-in point increases with the parasitic capacitance. The voltage across the gap during the pull-down process is equal to the total charge in the system divided by the total capacitance of the system, which is also equal to the charge across the gap over the gap capacitance. Therefore, Equation 2.12 still valid for the system with parametric capacitance.

With constant current input into the system, the charge can be expressed as

$$Q(x) = it(x) \tag{2.24}$$

To understand the effect of the parasitic capacitance on the pull down time, we substitute Equation 2.24 into Equation 2.23 to get

$$t(x) = \sqrt{\frac{2k\epsilon_0 A g_0}{i^2}} \sqrt{\frac{x}{g_0}}[1 + \frac{c_p}{c_0}(1 - \frac{x}{g_0})] \tag{2.25}$$

which can be written as

$$t(x) = T\sqrt{x_n}[1 + \frac{c_p}{c_0}(1 - x_n)] \tag{2.26}$$

where T is the time to pull down a cantilever without parasitic capacitance, as shown in Equation 2.10, and x_n is the displacement normalized to the gap. The normalized time required for the cantilever to pull down to a normalized position with various parasitic capacitances are plotted in Figure 2.12

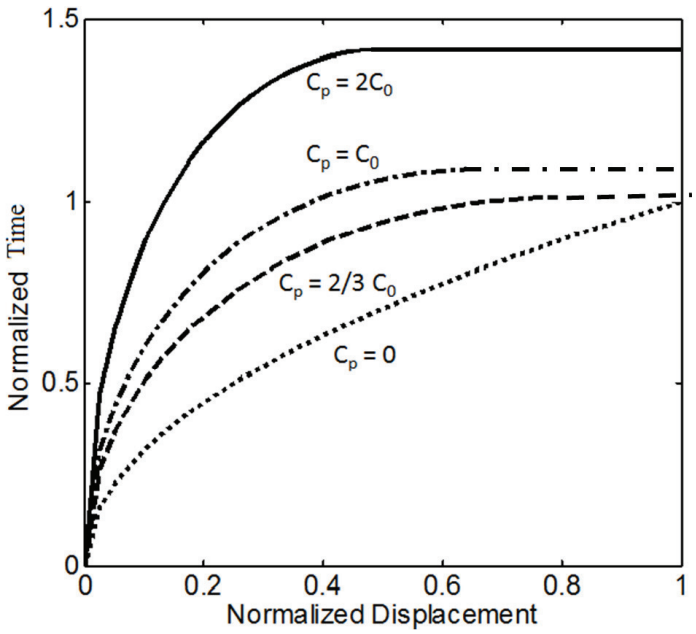

Figure 2.12: Normalized time required for cantilever to be pulled down to a normalized displacement with various parasitic capacitors

As the parasitic capacitance increases, the time needed for the cantilever to reach a certain displacement increases, and the total time required for the cantilever to be pulled down increases.

2.3.4 Charge leakage in the system

In the analysis so far, we have assumed zero leakage in the system. In reality, there are leakages across the gap and across the parasitic capacitors. As the voltage across the gap built up, low energy radioactive electrons are also lost because they cannot make across the gap. All of these will reduce the totally charge accumulation across the gap. Therefore, we need to study the effects of leakage current on the system.

If at any time in the cantilever pull-down process before pull-in, the leakage current is equal to the radioactive input current, the cantilever will stay at that displacement without ever reaching the bottom electrode. However, in this section, we will assume that the total leakage current is always smaller than the radioactive input current, which always results in the a cantilever pull down.

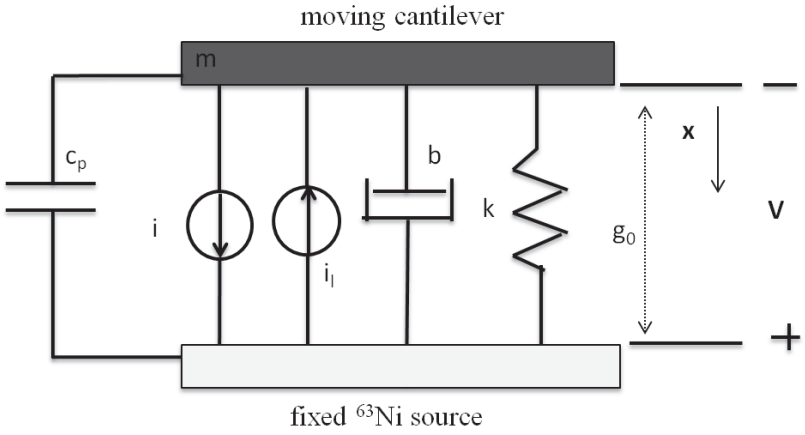

Figure 2.13: Charge-controlled actuation model of the discharge system with parasitic capacitances and leakage current

The system can then be modeled as shown in Figure 2.13. For the system with leakage current, with the overall force acting in the system can still be expressed with Equation 2.16, the current in the system is

$$i - i_l = \frac{dQ_g}{dt} + c_p \frac{dV}{dt} \tag{2.27}$$

where the total leakage current in the system, i_l can be expressed as

$$i_l = i_r + i_{lg} + i_{lp} \tag{2.28}$$

where i_r is the radioisotope current loss, i_{lp} is the parasitic capacitor leakage current, and i_{lg} is the leakage current across the gap. The equivelent resistance across the gap can be written as

$$R_{lg}(x) = R_0(1 - \frac{x}{g_0}) \tag{2.29}$$

with R_0 represent the initial resistance of the gap before pull-down. The resistance decreases as the cantilever is pulled down. The radioactive electrons have average energy of 17keV, and the voltage across the gap is much lower than 17kV. The i_r term in Equation 2.28 can therefore be neglected. The resistance of the parasitic capacitor can be approximated to be a constant value, R_p. Equation 2.28 can be simplified as

$$i_l \approx i_{lp} + i_{lg} = \frac{V(x)}{R_{lp}} + \frac{V(x)}{R_0(1 - \frac{x}{g_0})} \tag{2.30}$$

By substituting Equation 2.12 into Equation 2.30, we get

$$i_l(x) = \sqrt{\frac{2kg_0^2}{\epsilon_0 A R_p}}\sqrt{x}(1 - \frac{x}{g_0}) + \sqrt{\frac{2kg_0^2}{\epsilon_0 A R_0}}\sqrt{x} \tag{2.31}$$

In the discharge system, the parasitic capacitors have much larger gap than the gap between the cantilever and the source, which means $R_p >> R_0$. Equation 2.31 can therefore simplified as

$$i_l(x) = \sqrt{\frac{2kg_0^2}{\epsilon_0 A R_0}}\sqrt{x} \tag{2.32}$$

Equation 2.19 can then be modified as

$$Q_g = \frac{Q - Q_l}{1 + \frac{c_p}{c_0}(1 - \frac{x}{g_0})} \tag{2.33}$$

where Q_l is the total leakage charge. Comparing to the the system without leakage, due to the increase of leakage current with the displacement, in Equation 2.19, the mechanical force on the left side stay the same while the electrostatic force on the right side decreases. Therefore, the cantilever can be pulled down further while staying in steady state condition. Since the total charge needed to pull a cantilever down is fixed, the pull-down time for the cantilever increases due to leakage. Leakage current should be minimized in the system to optimize the system operation efficiency.

2.3.5 Energy conversion in the pull-down process

If thermal energy generation due to dumping and electron bombardments is ignored, during the cantilever pulling down, radioactive energy from the electron is converted into electrostatic energy across capacitors (gap capacitor and parasitic capacitor) and mechanical energy on the cantilever, which include potential energy due to bending and kinetic energy due to its movement.

$$E = E_{eg} + E_{ep} + E_p + E_k \tag{2.34}$$

where E is the total energy, E_{eg} and E_{ep} are the electrostatic energy stored in gap capacitor and parasitic capacitor respectively, and E_p and E_k are the potential energy and kinetic energy stored on the cantilever respectively. The entire pull-down process can be divided into two parts, before and after cantilever pull-in.

Before the cantilever is pulled in, under steady state condition, the cantilever is moving in a low speed. The kinetic energy is much smaller compared to others [22], so it is not included in the following discussion in this section.

With Equation 2.12, the electrostatic energy stored in the gap capacitor and parasitic capacitor can be expressed as

$$E_{eg} = \frac{1}{2}c_g V^2 = kg_0^2 \frac{x}{g_0}(1 - \frac{x}{g_0}) \tag{2.35}$$

$$E_{ep} = \frac{1}{2}c_p V^2 = \frac{c_p}{c_0} kg_0^2 \frac{x}{g_0}(1 - \frac{x}{g_0})^2 \tag{2.36}$$

and the potential energy stored in the cantilever is

$$E_p = \frac{1}{2}kx^2 = \frac{1}{2}kg_0^2(\frac{x}{g_0})^2 \tag{2.37}$$

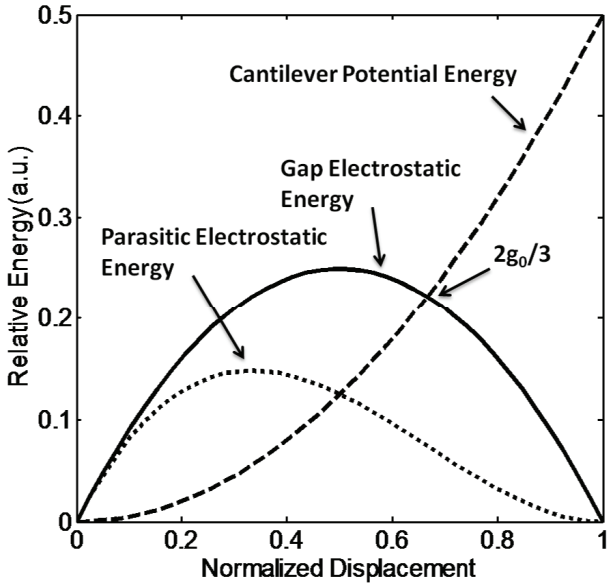

Figure 2.14: The electrostatic energy stored in gap capacitor and parasitic capacitor, and the potential energy stored in the cantilever with respect to the normal displacement

With the displacement normalized to g_0, and the energy normalized to kg_0^2, the energy distribution with respect to displacement is plotted with $c_p/c_0 = 1$ in Figure 2.14. The electrostatic energy stored in gap capacitor and parasitic capacitor have maximum value at $g_0/2$ and $g_0/3$ respectively.

If the cantilever is pulled down without pull-in, after the energy stored in the capacitors reach the maximum value, the input energy and the capacitor-stored electrostatic energy start converting into cantilever potential and kinetic energy. Since the cantilever moves relatively slow without pull-in, the majority of the energy is converted into potential energy stored in the cantilever.

If cantilever pull-in happens, during the pull-in process, the energy input from the radioactive source is minimum due to the short pull-in time. Therefore, all the cantilever potential and kinetic energy gain are from the decrease of the electrostatic energy.

2.4 Vacuum electrostatic discharge conditions for radioisotope-powered system

In the last section, we studied the cantilever pull down process, and in this section, we focus on what happens once the cantilever is pulled down. We will study the conditions for electrostatic discharge while the cantilever is pulled towards the radioisotope source.

With positive charges accumulated on the ^{63}Ni source and electrons collected on the cantilever, the electric field across the cantilever and the radioactive source can be derived from Equation 2.12.

$$E(x) = \frac{V(x)}{g_0 - x} = \sqrt{\frac{2k}{\epsilon_0 A}}\sqrt{x} \tag{2.38}$$

For a gold cantilever with Young's modulus, thickness, and length of $79GPa$, 300μm, and $5cm$ respectively, with overlap length of $7mm$ and gap of 500μm, the electric field across the gap with respect to the pull-down displacement is plotted in Figure 2.15

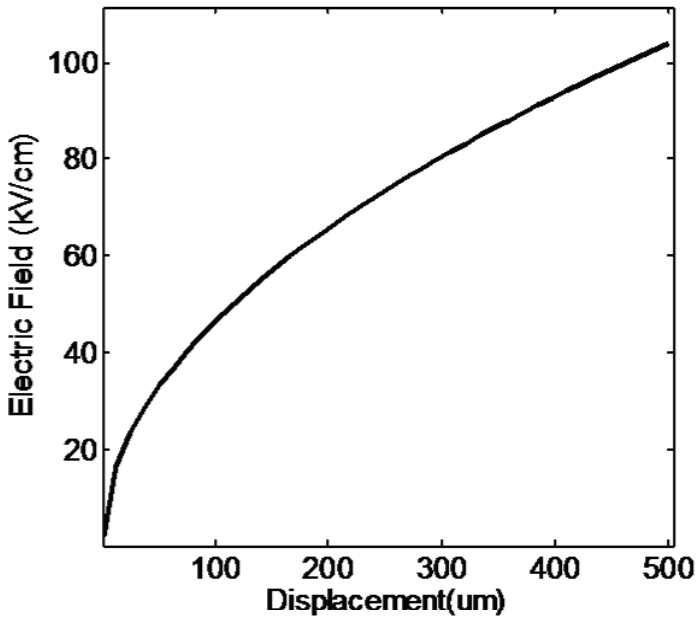

Figure 2.15: Electric field versus cantilever pull-down displacement with 500μm initial gap

As shown in Figure 2.15, the electric field across the gap increases with displacement, reaching over $100kV/cm$. In the pull-down process, when the electric field is above the breakdown field of the system, with or without pull-in, electrostatic discharge will take place across the remaining gap.

2.4.1 Introduction to electrostatic discharge

Electrostatic discharge have utilized to generate large current pulses or electrical signals for decades. One of the most common electrostatic discharge systems is the spark gap discharge system, typically consisting of high voltage sources and spark gaps housed either in gases or in vacuum. The spark gap is charged up

to a high voltage with the voltage source, and triggered with either a separate electrode [24] or laser [25]. Due to the requirement of high voltage source and complex triggering systems, the system is power-hungry, bulky, and difficult to be integrated with small electronic devices. The radioisotope-powered discharge system overcomes the problems with compact energy source and self-triggering mechanism through cantilever pull-down. The discharge mechanism is similar to the generation of "electrostatic shock" we get when touching a metal surface on a dry winter day. As the two electrodes, hand and metal surface in this case, are moving close together, electrical spark discharge happens due to large electric field.

In air, the electrostatic discharge is induced by the ionization of the gas atoms and molecules in the gap by the electron bombardment [26]. When the ionization rate, which depends on the electric field, reaches a certain level, a plasma will be generated around the anode. As the plasma moves from the anode to the cathode, a plasma channel is created across the gap. An electrostatic discharge thus happens. Therefore, the discharge process can be divided into two different phases: the surface electron generation and acceleration process and the avalanche process.

In the surface process, electrons are generated on the cathode, injected into the gap, and accelerated due to the voltage across the gap. The duration of the process is extremely small (about 40 ps), and there is no ionization in this process because the electron energy is below the ionization energy [27]. Once the electrons acquired enough energy, the ionization/avalanche process begins, which has a longer rise time (hundreds of picoseconds) than the surface process. The duration and significance of the two processes are shown in Figure 2.16 [27]. The plasma propagates across the gap towards anode, and discharge occurs only after the electron avalanche has established an ionized channel from cathode to anode.

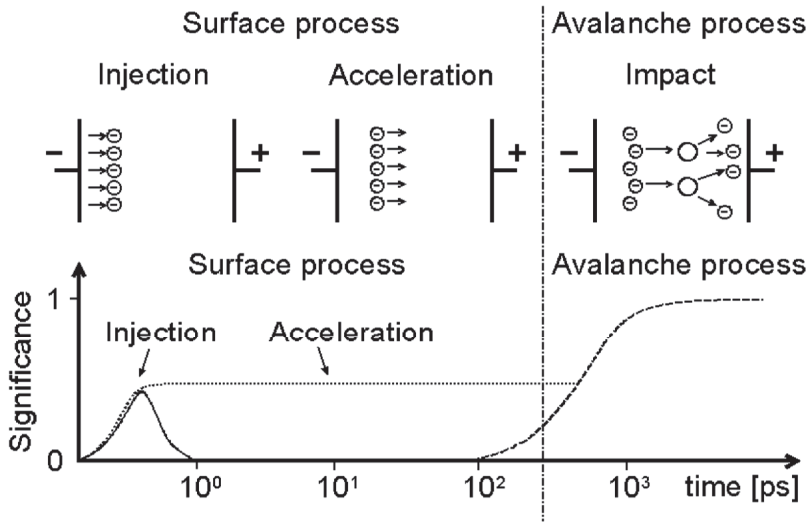

Figure 2.16: Schematic illustrating the significance of the surface and avalanche process [27]

The dynamics of the switch during breakdown process determines its resistance, inductance, and the rise time of the current [28].

In this section, to study the condition for electrostatic discharge to take place, we focus on the discharge current during the surface electron generation and acceleration process.

2.5 Study of current and radiated electromagnetic field from radioisotope-powered electrostatic discharge system

In the last section, we studied the conditions for electrostatic discharge to take place. We will focus on the results of the discharge in the section, namely the generation of discharge current and electromagnetic field.

The electrostatic discharge is actually a serious threat for electronics or integrated circuits, and it has been studied extensively [29, 30, 31, 32, 33, 34]. The International Electrotechnical Committee (IEC) prescribed the standard 61000-4-2 in order to define a procedure to be followed immunity the tests on electrical or electronic equipment against electrostatic discharges. According to IEC 61000-4-2 [35], an ESD generator must be designed produce a human body model (HBM) pulse as shown in Figure 2.17 to simulate the discharge event between human and electronic devices in air. The pulse consist of two parts: a first peak called the "initial peak" with maximum current and fast rise time, caused by the discharge through the hand, a low inductance path, and a second peak, which is caused by the discharge of the body, which generates a much longer pulse. The fast initial spike generates large values of $\partial i/\partial t$, where i represents the discharge current. Electromagnetic wave is generated due to abrupt current change [36] [37].

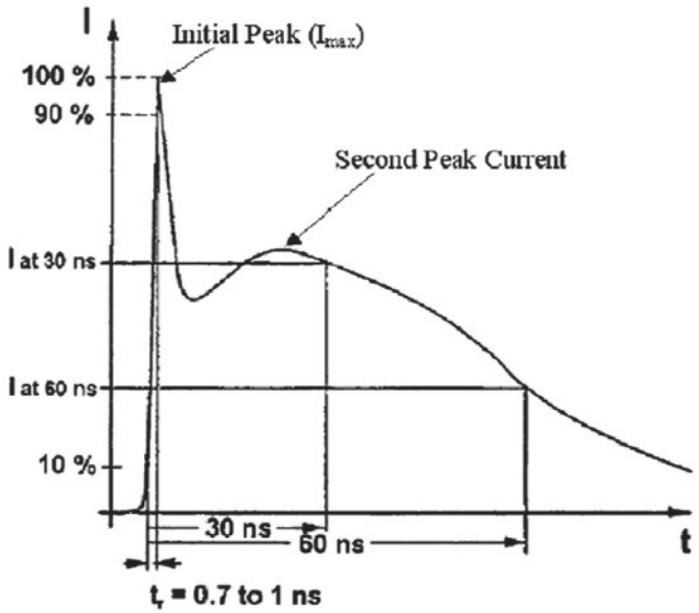

Figure 2.17: Typical waveform of the output current of the ESD generator

Therefore, electrostatic discharge is accompanied by two phenomena: the injection of discharge currents and the radiation of electromagnetic pulses [38]

[36]. Since Both phenomena could lead to RF signal output from the radioisotope-powered discharge system. They will be studied in details for better understanding and optimizing of the system

2.5.1 Electrostatic discharge Current

As mentioned in the last section, the discharge process consists of two different phases: the surface electron generation and acceleration process and the avalanche process. In this section, we focus on the discharge current during the avalanche phrase, which contribute the most of the output current. The discharge current can be derived from the equivalent arc resistance, reported by Rompe and Weizel [29]. Assuming the channel conductivity proportional to the dissipated ohmic energy, the arc resistance can be calculated as

$$R(t) = \frac{d}{\sqrt{2a \int_0^t i(\xi)^2 \, \mathrm{d}\xi}} \tag{2.39}$$

where R is the arc resistance, d is the arc length, a is empirical constant, and i is the current. Assuming the discharge current is a single shot impulse current, the total charge across the gap just prior to discharge is [39]

$$q = I_{max}\tau \tag{2.40}$$

where I_{max} is the peak discharge current and τ is the nominal duration period. The discharge current can be written as

$$i(t) = I_{max}F(t/\tau) \tag{2.41}$$

Where $F(.)$ is a dimensionless function representing the electrostatic discharge current waveform with

$$\int_0^\infty F(x)dx = 1 \tag{2.42}$$

Combing Equation 2.39 and Equation 2.41, we can get [39]

$$I_{max} = \frac{C_0 V_s a (V_s/l)^2}{3\sqrt{3}} \tag{2.43}$$

$$F(x) = \frac{3\sqrt{3}}{2} e^{3\sqrt{3}(x-x_0)} [1 + e^{3\sqrt{3}(x-x_0)}]^{-1.5} \tag{2.44}$$

$$\frac{\partial F(x)}{\partial x} = \frac{27}{4} e^{3\sqrt{3}(x-x_0)} [1 + e^{3\sqrt{3}(x-x_0)}]^{-2.5} [2 - e^{3\sqrt{3}(x-x_0)}] \tag{2.45}$$

where C_0 is gap capacitance before discharge, V_s is the spark voltage, and x_0 is an integral constant. The nominal discharge period can be derived from Equation 2.43 to be

$$\tau = \frac{3\sqrt{3}}{a(V_s/l)^2} \tag{2.46}$$

As shown in Equation 2.43, 2.44, and 2.46, with a being a constant, the electrostatic discharge current is determined by the spark voltage, the spark length, and the capacitance. The maximum current is proportional to the discharge voltage, gap capacitance, and the square of the gap breakdown field, while the nominal period is solely determined the breakdown field.

The analyses above are for fixed gap electrostatic discharges, where the arc length is well defined. However, for a discharge gap with one moving electrode (Figure 2.18), arc length is controlled by discharge voltage, and electrode speed, and the capacitance. While fixed gap arc discharge has been well studied and simulated [40] [39], for the discharge with moving electrodes, only experimental results have been reported in the literature [29] [41].

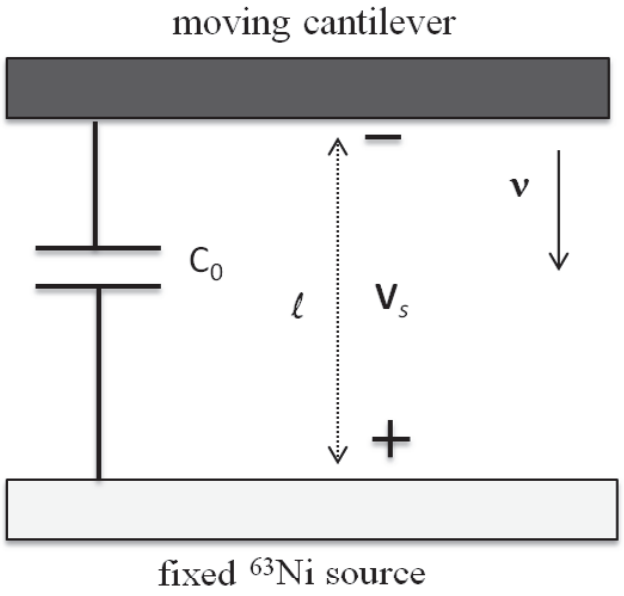

Figure 2.18: Schematic illustrating the moving cantilever in the discharge system

For the moving electrode analyses, first, the discharge voltage is assumed to be constant, while we exam the effects of the approach speed on the maximum magnitude and nominal period (rise time) of the discharge current. The discharge current peak values increase with electrode approach speed, while the current rise times decrease with the approach speed [29]. The change of peak current and rise time with approach speed can be understood by examining the corresponding arc lengths. It was reported that the arc lengths decrease with the electrode approach speed, especially for voltage over $1kV$ [41] [42]. The decrease of arc lengths with other parameters staying constant will lead to increase of current peak magnitude and decrease of rise times, as shown in Equation 2.43 and 2.46.

With approach speed staying constant, the maximum magnitude of the discharge current increases with charge voltage until it reaches a maximum value after which the current decreases. The rise time of the discharge current initially stays flat with the voltage until it reaches a threshold value, after which it increases sharply until it reaches a maximum value. The rise time will then decrease again

with the increasing voltage. The variation of the current and rise time could also be caused by the changing of arc length.

For high frequency signal generation, large current output with short rising time is desired. Therefore, cantilever with larger approach speed upon discharge will be preferred in the radioisotope-powered discharge system, which can be achieved by either increasing the gap size or increase the ratio between parasitic and gap capacitances.

2.5.2 Electromagnetic radiation from electrostatic discharge

Upon electrostatic discharge, electromagnetic field is also generated with the discharge current. While the discharge current is constrained within the circuitry physically connected to the discharge system, the electromagnetic wave generated across the gap can be transmitted and received wirelessly over a long distance without requirement of antenna, which makes miniature RF pulse generator possible. However, we need to first understand the electromagnetic wave generated for the discharge.

Assuming the cross section area of the plasma channel during discharge is small, the electromagnetic field generated can be approximated with a current dipole with length l. The electric and magnetic field can then be express as [36]

$$\begin{aligned}\overline{E}(\overline{r},t) \approx \overline{a}_\rho l \frac{\rho z}{R^2}\frac{\eta_0}{2\pi}\left\{\frac{3i(\mu)}{R^2}+\frac{1}{cR}\frac{\partial i(\mu)}{\partial \mu}\right\} \\ +\overline{a}_z l \frac{\eta_0}{2\pi}\left\{\left[\frac{3z^2}{R^2}-1\right]\frac{i(\mu)}{R^2}+\left[\frac{z^2}{R^2}-1\right]\frac{1}{cR}\frac{\partial i(\mu)}{\partial \mu}\right\}\end{aligned} \tag{2.47}$$

$$\overline{H}(\overline{r},t) \approx \overline{a}_\phi l \frac{\rho}{R}\frac{1}{2\pi}\left\{\frac{i(\mu)}{R^2}+\frac{1}{cR}\frac{\partial i(\mu)}{\partial \mu}\right\} \tag{2.48}$$

where R is the distance from the discharge point to the observation point

(ρ, ϕ, z), η_0 is the free-space wave impedance, c is the propagation speed, and $i(\mu)$ is the time-dependent ESD current waveform evaluated at time μ, where $\mu = t - R/c$.

From Equation 2.47 and Equation 2.48, we can see there are two basic regions: a near-field zone dominated by $i(\mu)$ and a far-field zone dominated by $\partial i(\mu)/\partial\mu$. For long distance RF signal communication, near-field zone can be ignored, and the equations can be rewritten as

$$\overline{E}(\overline{r}, t) \approx \overline{a}_\rho l \frac{\rho z}{R^2} \frac{\eta_0}{2\pi} \frac{1}{cR} \frac{\partial i(\mu)}{\partial \mu} + \overline{a}_z l \frac{\eta_0}{2\pi} \left\{ \frac{z^2}{R^2} - 1 \right\} \frac{1}{cR} \frac{\partial i(\mu)}{\partial \mu} \tag{2.49}$$

$$\overline{H}(\overline{r}, t) \approx \overline{a}_\phi l \frac{\rho}{R} \frac{1}{2\pi} \frac{1}{cR} \frac{\partial i(\mu)}{\partial \mu} \tag{2.50}$$

Equation 2.49 and Equation 2.50 shows that the electromagnetic signal detected will be determined by the time derivative of the discharge current. The magnitude of the electric and magnetic field with respect to the distance is determined by the magnitude of R, and the ratio among ρ, ϕ, and z. In the same direction, the field magnitude is inverse proportional to the distance, but within the same distance, the magnitude various with direction.

For radiation detected with a loop antenna, the induced voltage is due to the magnetic field generated by the discharge. The magnitude of the magnetic field at a far-field zone is

$$H(t) \approx \frac{\rho}{R} \frac{l}{2\pi} \frac{1}{cR} \frac{\partial i(t - R/c)}{\partial t} \tag{2.51}$$

To calculate the magnetic field, we need to understand the magnitude and waveform of the time derivative of the discharge current. While the waveform is shown in 2.44, the maximum slope of the discharge current can be calculated from Equation 2.43 and 2.44 to be

$$\frac{di}{dt}|_{max} = \frac{2\sqrt{21}-3}{75\sqrt{6}-\sqrt{21}} C_0 V_s a^2 (V_s/l)^4 \tag{2.52}$$

As shown in Equation 2.43, the magnitude of the magnetic field is proportional to the forth order of the breakdown field strength. The nominal period of the magnetic wave stays the same as the discharge current.

2.6 System implementation and simulation

As shown in Figure 2.19, a gold cantilever (5cm×0.8cm×300μm) and ^{63}Ni source discharging system is housed inside a small glass vacuum chamber that is evacuated and sealed. Gold is used in the experiments due to its lack of native oxide, thus better contact between the cantilever and the radioisotope source. Since the metal cantilever operate inside vacuum, other metals such as copper can also be used. Connected to a vacuum pump, the chamber is pumped down to 10^{-3}mTorr. Both the gold cantilever and the ^{63}Ni source are held in place with quarter-inch thick Teflon plates, which forms a capacitor C_b at the beam holder, and a capacitor C_s at the radioactive source holder (Figure 2.20(a)). C_g (t) is the air-gap capacitance at any given time t. An RF receiver (air-core coils with 21 turns and 1.5cm inner diameter) is connected to a high bandwidth oscilloscope (LeCroy WaveMast 8500) placed outside the chamber to detect and record the RF signal (Figure 2.20(b)).

To understand the discharge system for future designs and optimizations, an LC circuit model is developed for the system with the measured values of the components list in Table 2.2. When an arc discharge occurs across the air gap, a sub-nanosecond high power current pulse is released which generates oscillations in the RLC circuit at hundreds of megahertz for hundreds of nanoseconds. After the discharge, the cantilever is effectively at rest because of mechanical inertia. Then the gap between the cantilever and the source is very small, which means

the value of C_g is very large at that moment compared to other capacitors in the circuit.

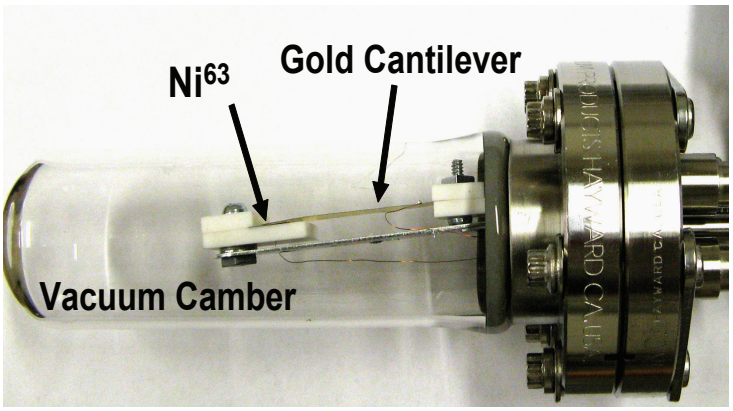

Figure 2.19: Photograph of the self-powered wireless discharge system

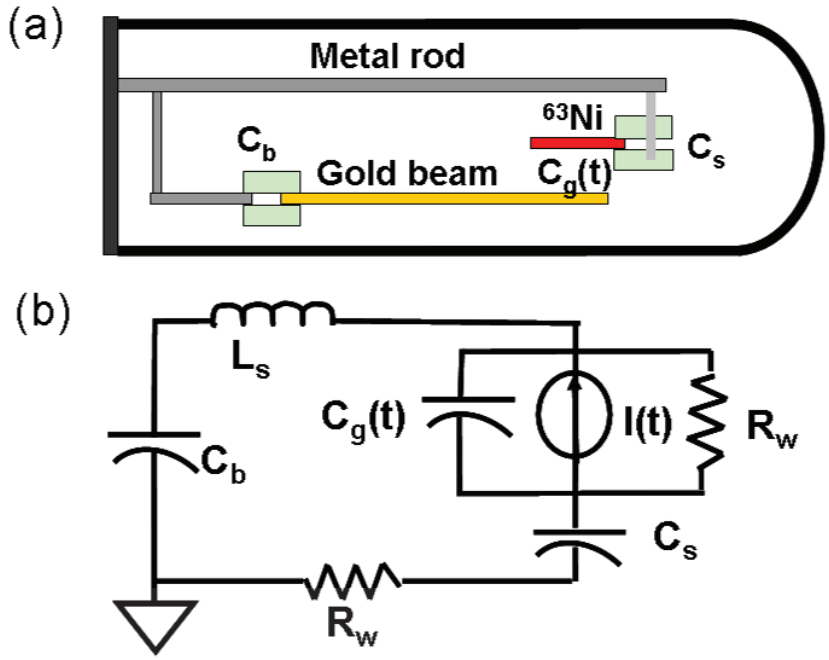

Figure 2.20: (a)schematic, and (b) equivalent LC circuit of the self-powered wireless discharge system

Table 2.2: Representation and values of R, L, C components in the equavilent circuit model in Figure 2.20(b)

Component	Representation	Value
C_s	Source holder capacitance	8.3pF
C_b	Beam holder capacitance	8.3pF
R_w	Resistance of metal beams and rod	0.1 ohm
L_s	Equivalent inductance of the system	2.4nH
C_g (t)	Air gap capacitance	-
I(t)	Air gap current	-
R(t)	Equivalent resistance across the air gap	-

2.7 Testing of the radioactive powered discharge system

For the discharge system implemented in the last section, upon discharge, an RF signal with frequency of 1.52GHz, which lasts for around 10ns, is remotely detected across a 50 Ohm oscilloscope load with maximum peak-peak output voltage of 2V (Figure 2.21). Therefore, a maximum wireless power output of 800mW is obtained, which can be used to enable wireless RF communications.

To verify the circuit model proposed in Figure 2.20(b), simulation in SPICE with the capacitance across the discharge air gap, C_g estimated to be 100pF with contact area of $100\mu m^2$. Capacitance C_g is much larger than C_s, and it acts as a short compared to other impedances in the circuit. R(t) is relatively large and is ignored in this simulation, as it is shorted out by C_g at the time scales involved. The values of other capacitors and inductors used in the simulation are listed in Table 2.2. The cantilever reciprocation period is 3 minutes with 0.64cm of the cantilever area exposed to the radiation. Therefore, with 9pA (1.5mCi) electron current, the totally charge across the air gap at the time of arc discharge is 1nC. Assuming the discharge lasts 1ns, the average discharge current will be 1A. A pulse current of 1A with rising and falling time of 0.1 ns (time estimated from experimental values) and duration time of 1ns are chosen to excite the LC

circuit in the simulation (resonance frequency of the circuit is independent of pulse magnitude and duration). The simulated resonance frequency of the LC circuit is plotted in Figure 2.22, together with the frequency of remotely measured RF signal from device shown in Figure 2.21. The simulation result agrees with the experimental result, both of which are 1.52 GHz.

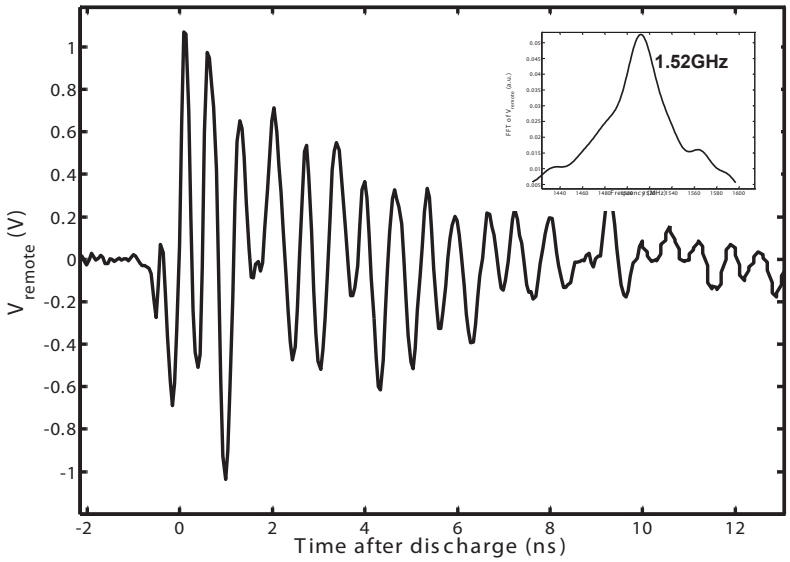

Figure 2.21: Magnitude and frequency of the remotely detected RF signal of the arc discharge system

2.8 Efficiency study of the radioactive powered discharge system

To meet the power requirements of wireless RF sensors/RFIDs, in the previous sections, we have demonstrated a discharge-based energy integration system that can output hundreds of milliWatts of RF power. We have also studied the operation principle of the system, and successfully developed a equivalent circuit model to predict the output frequency of the system. In this section, we focus on increasing the radioactive to electrical energy conversion efficiency. To improve the conversion

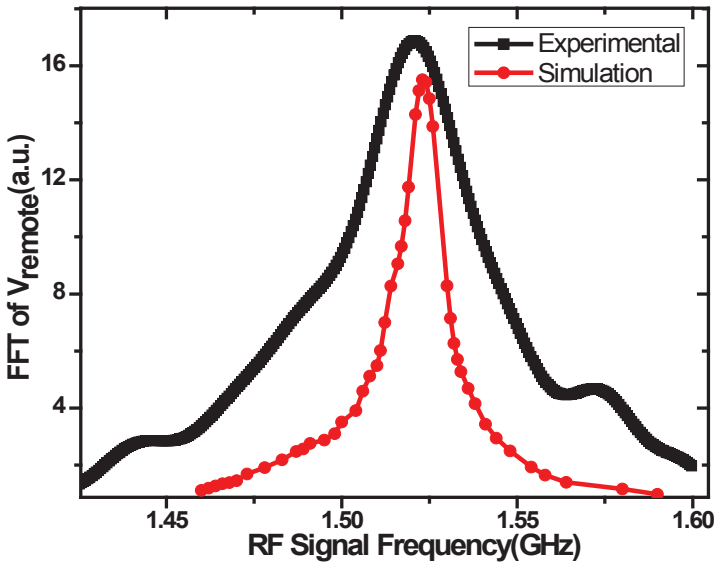

Figure 2.22: Resonance response of the arc discharge system from SPICE simulation and experimental measurement

efficiency of the system, we analyze the energy transformation process in the cantilever discharge cycle.

In the cantilever reciprocation charging cycle, when the radioisotope emitted-electrons cross the vacuum-gap to reach the collector, the radioisotope kinetic energy is converted to electrostatic energy and thermal energy, while electrostatic energy is then converted to electrical energy and mechanical energy. The thermal energy is due to electron kinetic energy dissipated in the cantilever; the mechanical energy is due to deformation of the cantilever; while the electrical energy is stored in various capacitors in the system.

The discharge system is studied for overall radioactive to electrical energy conversion with varying gaps between the cantilever and source. As shown in Figure 2.23, the total collected radioactive energy increases linearly with the gap, but the output electrical energy shows a quadratic increase with gap before decreasing after 600μm figure 2.24 . Therefore, there is an optimal gap for maximum radioactive to electrical energy conversion efficiency (600μm for the

prototype device). The decrease in efficiency for gaps greater than the optimal gap could be due to increase of leakage of emitted electrons at large emission angle, and decrease of lower field emission current due to higher voltage across the gap.

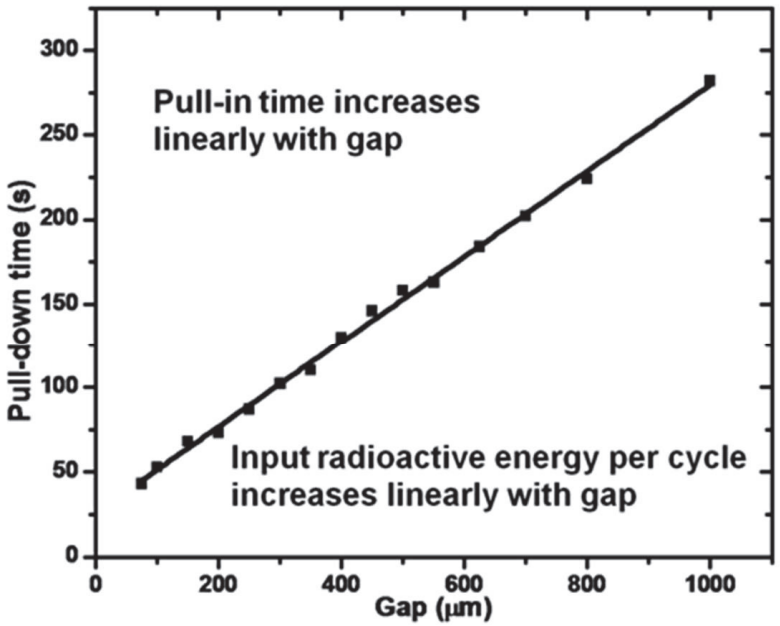

Figure 2.23: Measured pull-in time of the discharge system at different gap sizes

2.9 Micro-fabricated discharge system

We have so far discussed the demonstration of the prototype macro-size discharge systems. To power wireless RFID/RF sensors, we need to have micro-size discharge systems (Figure 2.25). To achieve that, single crystal silicon cantilevers with various lengths were micromachined using a two-step deep reactive ion etch (DRIE) process with a SOI wafer (Figure 2.26), and assembled alongside a 1.5 millicurie ^{63}Ni source plate that could housed inside a 1cm $\times$ 1cm vacuum package. The RF signal is remotely detected using an antenna and measured with an oscilloscope. With beam length of 5mm, the remotely detected signal is plotted in Figure 2.27,

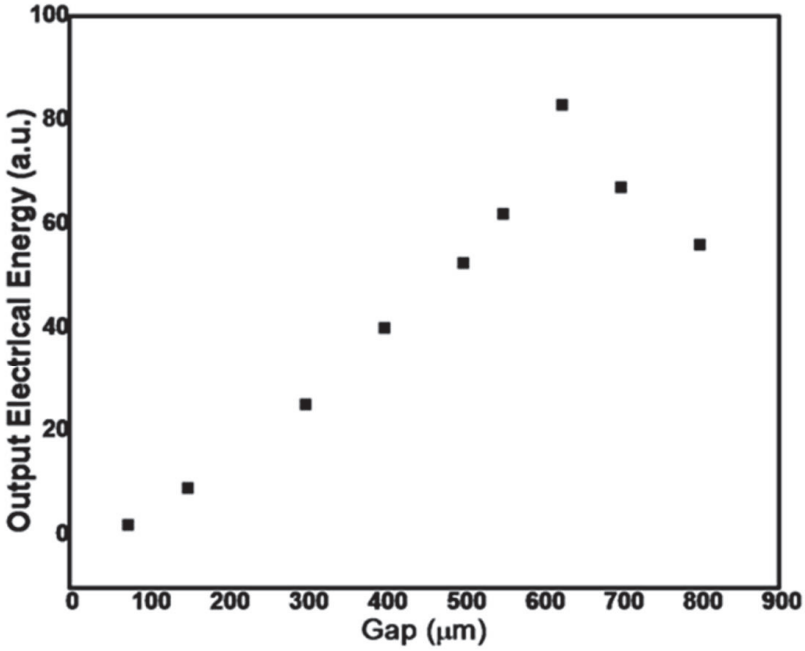

Figure 2.24: Measured discharge system output energy at different gap sizes at 320MHz

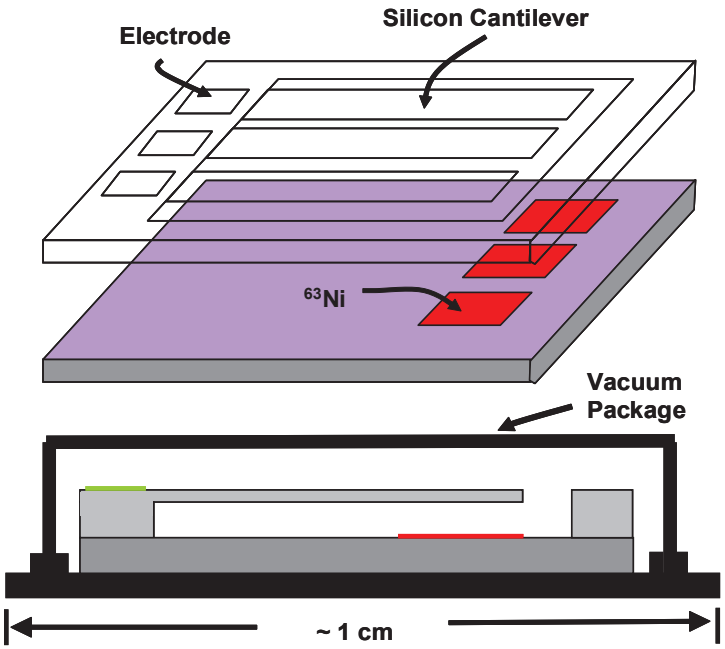

Figure 2.25: Schematic illustrating the integration and packaging of the micro-RF transmitter

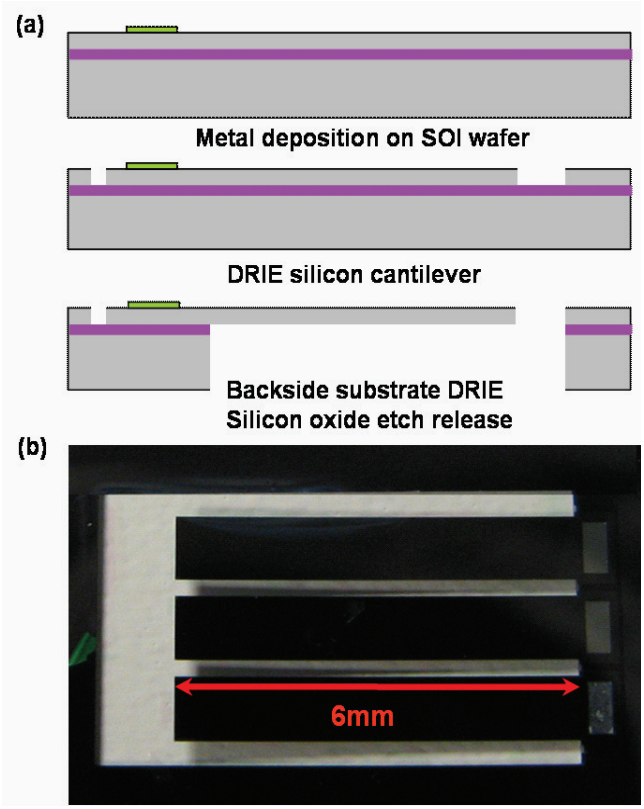

Figure 2.26: (a) Fabrication process and (b) photo of the microfabricated RF transmitter

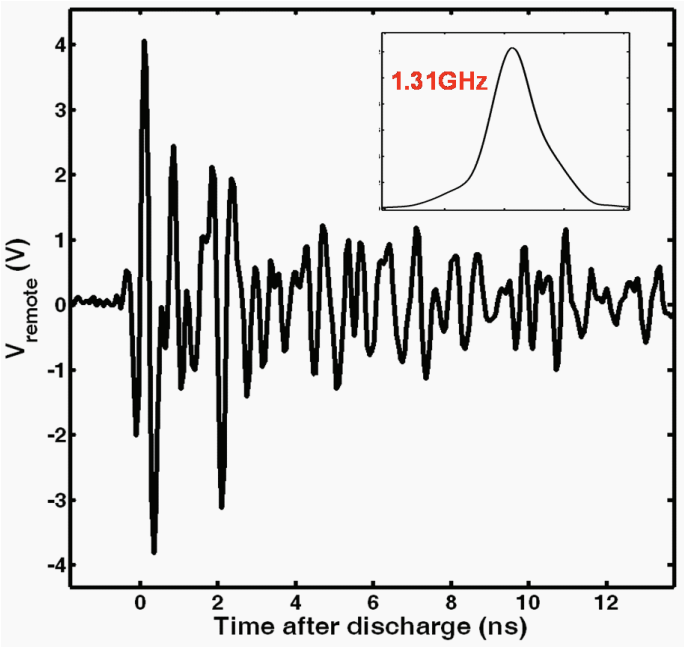

Figure 2.27: Waveform and frequency of the RF signal from a transmitter with 5mm long cantilever

where a RF signal with frequency of 1.31GHz is generated. With microfabrication, the discharge system can be assembled with much finer accuracy, thus enables better control of the equivalent inductance and capacitance of the discharge system. The frequency of the output RF signal can therefore be controlled better than macro-scale devices.

2.10 Vacuum study of the radioactive powered discharge system

The discharge system could potentially power wireless RF devices for decades. However, the life time of device is only as long as its vacuum packaging retains vacuum sufficient for the cantilever reciprocation. While it is important to have high quality vacuum packaging that would last for decades, it is equally important

to make sure the device can function under a wide range of vacuum conditions, and tolerate as high a vacuum level as possible. In this section, we studied the performance of the RF power generator at a wide range of vacuum conditions to establish the foundation for vacuum packaging to achieve long lifetime RF transmitters.

2.10.1 Experiment Setup

To conduct the experiment, as illustrated in Figure 2.28, a gold cantilever ($5cm \times 6mm \times 300\mu$m) is placed 250μm above a $63^N i$ radioactive thin film ($1cm \times 1cm$) with a 1.5mCi activity in a vacuum chamber. To characterize the discharge system under varying vacuum, a 47pF load capacitor and an antenna was connected to the cantilever output. The transmitted signal is detected wirelessly with another antenna and recorded with a real time oscilloscope. The chamber is first pumped down to 8.7×10^{-7}mBar, and then the pressure is slowly increased with a leak valve while taking measurements. The vacuum pressure levels rises at a rate of 10^{-5}mBar/hour to $10 - 2$mBar/hour controlled by the leak valve.

2.10.2 Experiment Results

The RF signal detected wirelessly at 8.7×10^{-7}mBar is shown in Figure 2.29, with 10μs duration and a carrier frequency of 306.5MHz. The reciprocation period of the system is 104 seconds. A signal component with much higher frequency is also detected at the beginning, which is the pulsed electromagnetic radiation signal corresponding to the original current pulse. The frequency of the electromagnetic signal, which is at around 1.5GHz, is determined by the electrostatic discharge time. The maximum RF signal frequency due to discharge current is therefore also 1.5GHz. As the vacuum level slowly increases inside the discharge chamber, the

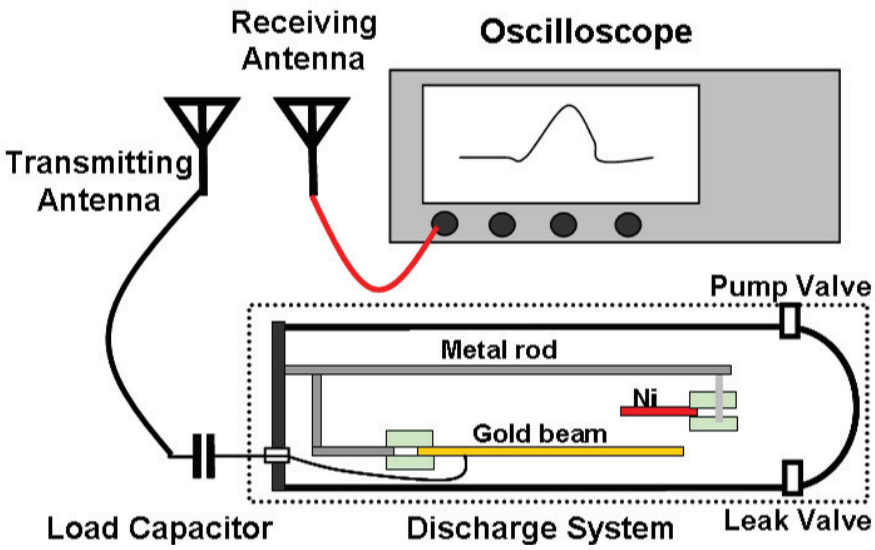

Figure 2.28: Schematic illustrating the testing setup for the discharge system with 47pF load capacitor and antenna connected to cantilever output with vacuum controlled by leak valve

discharge time and output wireless RF signal is recorded.

As shown in Figure 2.30, the discharge time stays almost constant at 104 seconds from 8.7×10^{-7}mBar to 2.2×10^{-3}mBar. The frequency of the output RF signal also remains constant at 306.5MHz. At pressure level of 2.2×10^{-3}mBar, the system abruptly stops reciprocating.

To understand the independence of discharge signal with vacuum level, the entire discharge process can be divided into cantilever pull-down process and electrostatic discharge process. With vacuum level higher than 10^{-3}mBar, there are not enough gas molecules in the gap, and the leakage across the gap is minimal. The reciprocation time, which is determined the cantilever stiffness, gap size, and radioisotope current, stay the same. In the electrostatic discharge process, at high vacuum, due to the lack of gas molecules across the gap, the discharge is dominated

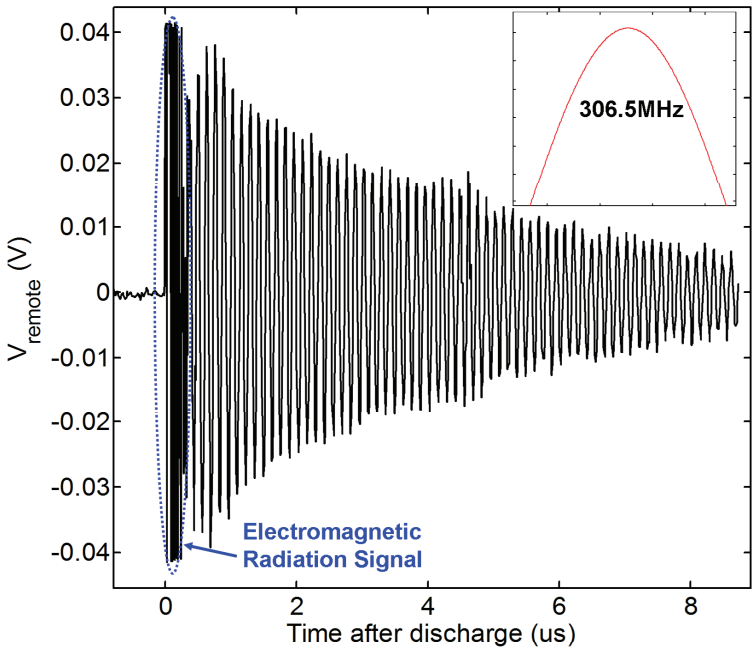

Figure 2.29: Experimental RF signal output of the discharge system with short electromagnetic radiation signal and pulse current induced LC signal at 306.5MHz

by cathode surface field emission [43], which is also independent of the pressure. However, as the pressure increases to above $2 \times 10{-}3$mBar, the gas avalanche discharge starts [44], which increases the leakage current across the gap (Figure 2.31). Therefore, system stops working because there is not sufficient voltage built-up across the gap to pull the cantilever down.

2.10.3 Radiation Current Measurement

To experimentally verify the vacuum discharge theory mentioned in the last section, a high impedance current meter is connected across the gap to measure the radiation current at different vacuum (Figure 2.32). With 1.5mCi radioactivity, the current emitted from the source is around 9pA. If there is no gas introduced charges with pressure below 2×10^{-3}mBar, the current should stay constant.

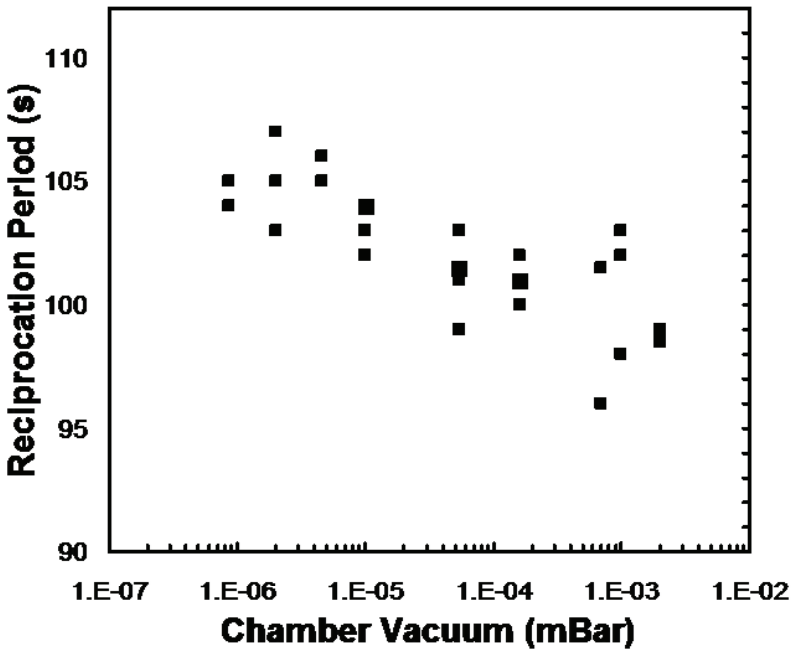

Figure 2.30: Reciprocation period of the system at different vacuum levels. Multiple data points are recorded at each vacuum level

The measurement results (Figure 2.33) agree with the prediction in Figure 2.31. The radiation current stays relatively constant below 2×10^{-3}mBar. Above that pressure, a leakage current increase is detected.

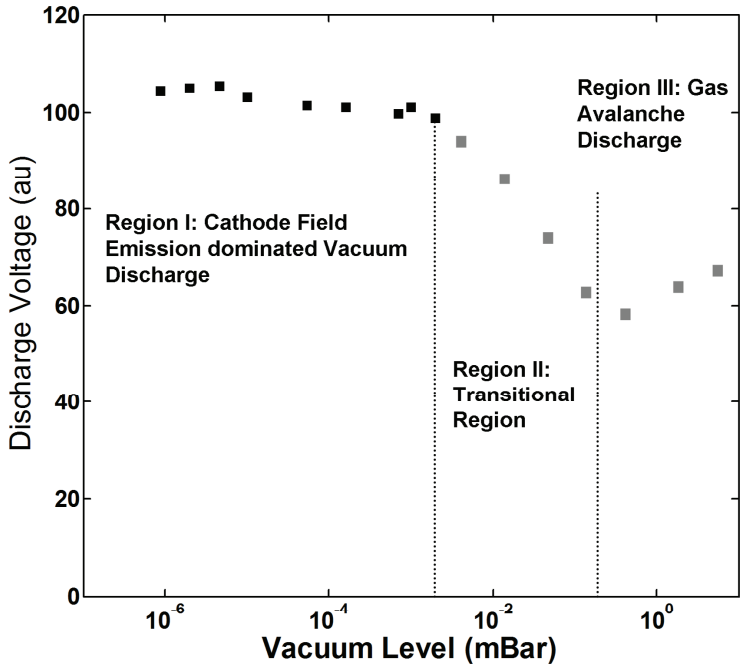

Figure 2.31: Schematic illustrating the discharge mechanisms of the vacuum breakdown at different vacuum levels [43]

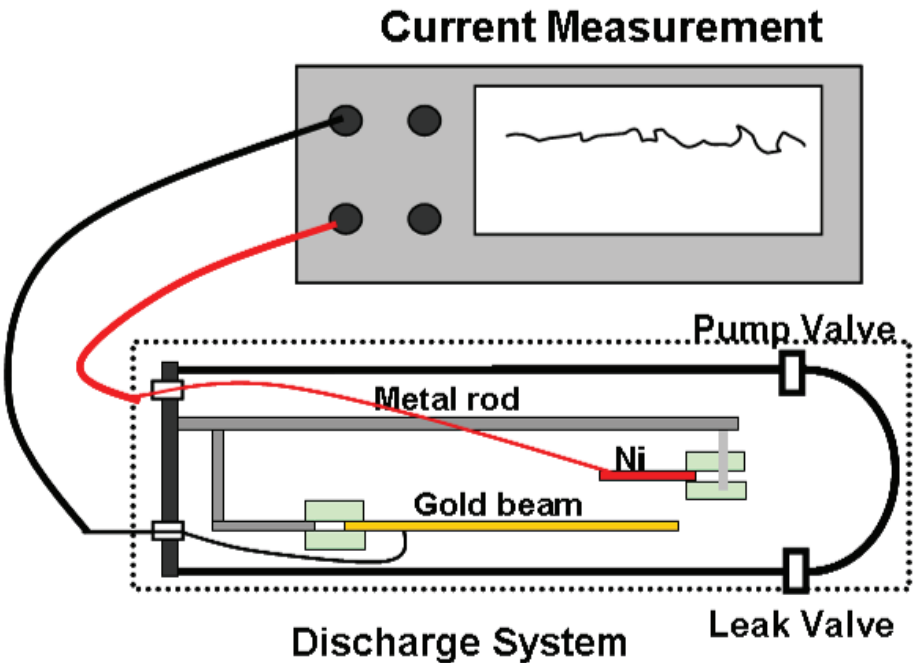

Figure 2.32: Schematic illustrating the testing setup for the radiation current measurement with a high impedance current meter(Keithley 2400)

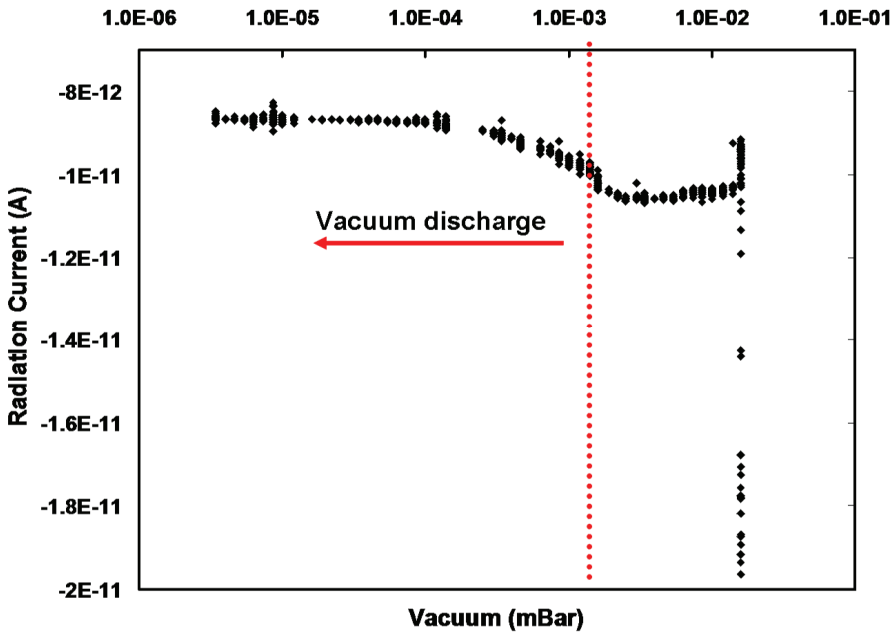

Figure 2.33: Experimental measurement of radiation current at under different vacuum condition with a 1.5mCi source

CHAPTER 3

RADIOISOTOPE-POWERED RFID AND SENSORS

We demonstrate a radioactive thin-film powered wireless sensor node which can transmit an RF signal coded with the environmental information gathered by a passive capacitive sensor. Sensor nodes operate for several decades and transmit data over RF links at powers of 100-1000 milliWatts. In our active sensor node, radioisotope energy emitted in electrons from ^{63}Ni thin films is used to electrostatically charge a cantilever over several minutes, and the stored electrical energy is released over a nano-second time scale, achieving a collected-to-released power amplification of 10^9 (10 mins/10ns). Even when the radioisotope emitted power is nanowatts from a benign amount of ^{63}Ni, over 500mW of transmitted RF power has been remotely detected. Since the half life of ^{63}Ni is 100 years, this RF transmitter can work autonomously for several decades. In our prototype wireless sensor node, a humidity sensitive polymer capacitance is used to demonstrate sensor node functionality. A transmitted frequency shift of 4.27 MHz over 150 MHz is achieved when the humidity changes from 22% to 97%.

3.1 Introduction

In Chapter 2, we have demonstrated a discharge-based energy integration system that can output hundreds of milliWatts of RF power, which can be used as a wireless RFID. We have also developed a equivalent circuit model to predict the output frequency of the system. The RF signal frequency of the system is determined by the values of the equivalent capacitance and inductance in the system. Therefore, we have to redesign the discharge system for the RFID to output different frequencies, which is costly with equivalent LC values very difficult to control precisely. To overcome that, in this chapter, we are going to

study the effects of externally connected inductances and capacitance on the RF signal output. If the frequency of the RF signal can be controlled with external LC components, various RFID/RF sensors can be implemented with the same discharge system.

3.2 Radioisotope powered discharge system with external capacitances

To study the impacts of the external capacitive components on the RF signal. As shown in Figure 3.1(a), external capacitor is connected to the arc discharge system. In the equivalent circuit (Figure 3.1(b)), the circuit inside the dotted box is the arc discharge system, while C_{SC} is the external capacitance. L_w, and R_e, the inductance and resistance introduced by wire connections to the external capacitor, are measured to be 61nH and 0.8 Ohm respectively using LCR meter (HP 4275A). A 20pF capacitor is connected to the discharge system while the RF signal is remotely detected upon cantilever discharge. The output RF signal is record with a oscilloscope and analyzed. As shown in Figure 3.2 , the 1.52GHz signal still exist for the first 10ns with an additional 214MHz component existing in the RF signal. The RF signal lasts for more than 300 ns with a maximum of 500mW detected 20 cm away from the chamber via the RF receiver. The SPICE simulation result of the new LC circuit (Figure 3.1(b)) with 20pF external capacitor agrees with the experimental measurement (Figure 3.3).

External capacitors with different values are then used to examine their impact on the frequency of the RF signal. The output RF signals are remotely detected with receiver and analyzed. The frequency of the RF signal is plotted versus the external capacitance in Figure 9. The frequency decreases with increasing external

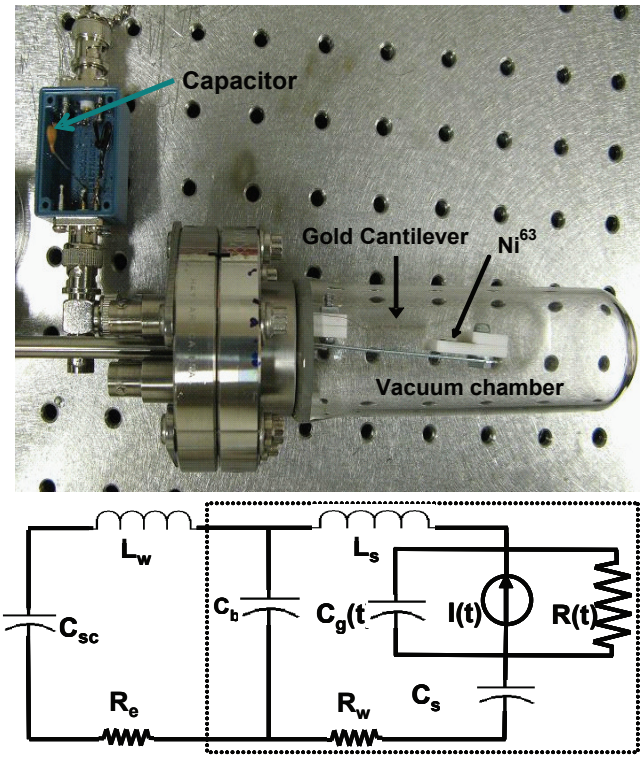

Figure 3.1: (a) Photograph, (b) equivalent LC circuit of the self-powered wireless discharge system with external capacitance

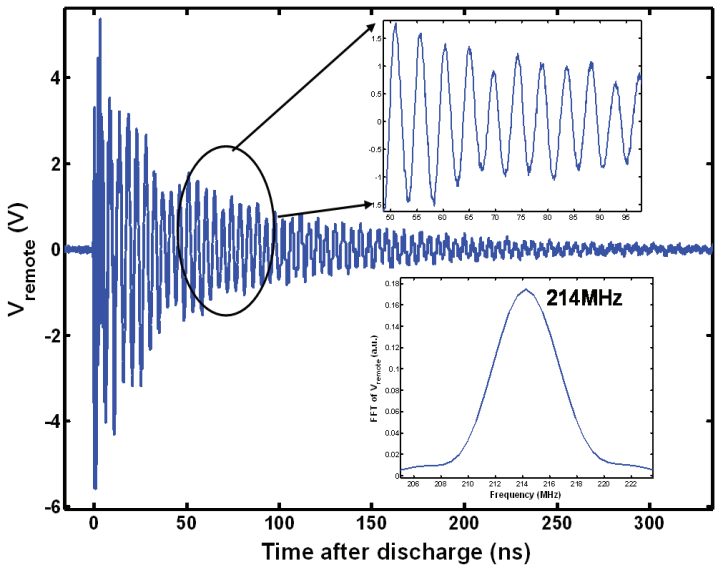

Figure 3.2: Magnitude and frequency of the remotely detected RF signal with 20pF external capacitance wireless RF sensor node

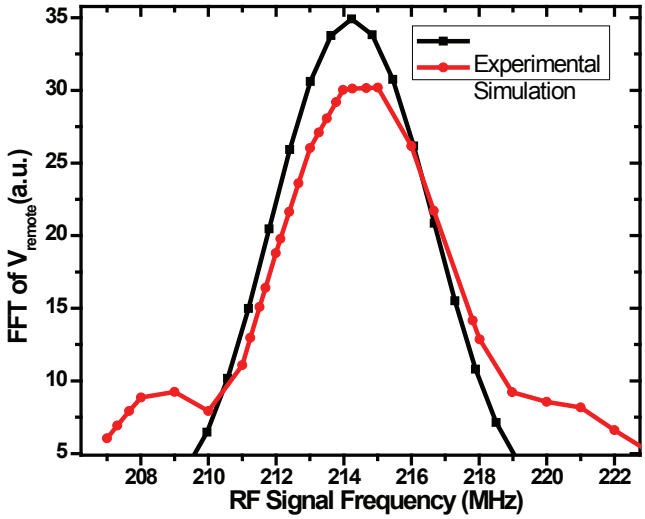

Figure 3.3: Resonance response of system with 20pF external capacitor from SPICE simulation and experimental measurement

capacitance. When the capacitance increases from 12pF to 75pF, a frequency shift of 63 MHz is achieved (239MHz to 176MHz). The result of the SPICE simulation of LC circuit model matches the measurement results. Therefore, with the circuit model, the value of the external capacitor can be extracted from the frequency of the remotely detected RF signal. The relative power of detected RF signals with different external capacitor values is also plotted in Figure 3.4. With cantilever reciprocation period almost stays the same, the transmitted RF signal power is consistent for all external capacitance values. However, the RF receiver has different gains at different frequencies, which causes the variation in detected RF signal power.

3.3 Radioactive powered wireless sensors

To implement a completely self-powered wireless sensor node, a capacitive polymer humidity sensor (Figure 3.5) is connected to the discharge system. The capacitance of the sensor at different humidity levels are first characterized (Figure 3.5). The

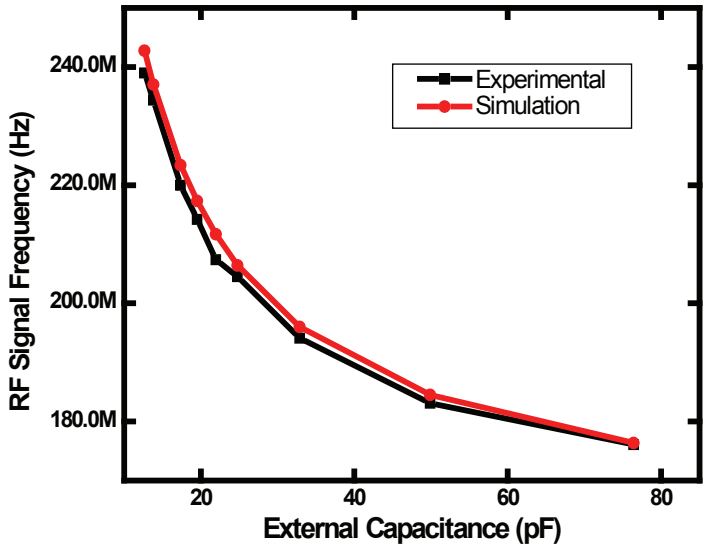

Figure 3.4: Experimental and simulated RF signal frequency with different external capacitance

different levels of relative humidity are generated by exposing the humidity sensor to different saturated salt solutions (with known relative humidity values) in a closed chamber. The capacitance of the sensor increases with the relative humidity. The RF signal is remotely measured at different humidity levels. The frequency of the signal is analyzed and plotted in Figure 11. A frequency shift of 4.27 MHz is achieved when the humidity changes from 22% to 97% (Figure 3.6). The experiment results match SPICE simulation outputs when the capacitance values of the humidity sensor are used in the LC circuit model in Figure 3.1(b).

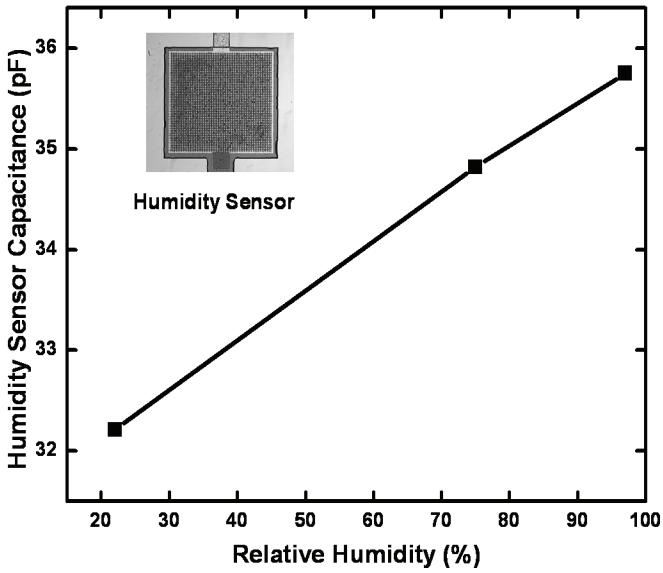

Figure 3.5: Measured humidity sensor capacitance at different relative humidity levels

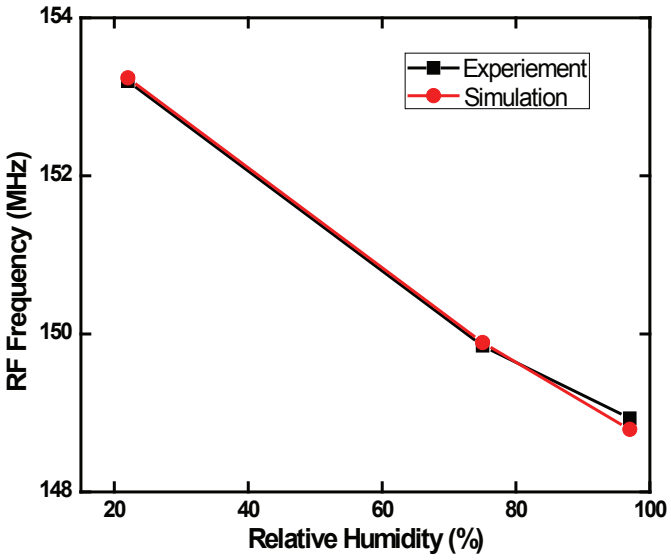

Figure 3.6: Measured remotely detected RF signal frequency at different relative humidity levels

CHAPTER 4

SAW-BASED RADIOISOTOPE-POWERED RF TRANSPONDER

In this chapter, we demonstrate radioisotope-powered pulse transponders that has a SAW (surface acoustic wave) device as the transmission frequency selector. Because the frequency is determined by a SAW device, narrowband detection with an identical SAW device enables the possibility for a long distance RF-link. The SAW transponders can be buried deep into structural constructs such as steel and concrete, where changing batteries or harvesting vibration or EM energy is not a reliable option.

4.1 Introduction

In Chapter 2 and Chapter 3, ^{63}Ni radioisotope actuated reciprocating metal and silicon cantilevers housed inside large vacuum chambers have been shown to generate RF pulses upon radioisotope discharge. However, the frequencies of the RF pulses in those previous efforts were determined by the equivalent LC circuit of the system. This makes it a challenge to generate RF signals at a specific frequency as needed, which are hard to model and design to output a specific frequency as needed for various turned RF-link applications. Furthermore, the RF pulse power determined by equivalent LC circuit is typically low (50), which also makes long distance narrow-band communication difficult. To have precise frequency control, a SAW resonator is connected to the discharge system as a frequency selector. In the SAW device, the frequency is determined by the gap between the fingers at the input port and the acoustic boundary conditions for the SAW pulse. Since the gap can be controlled precisely with microfabrication, the resonant frequency of the SAW device, hence the frequency of the output RF signal, can be designed to meet a given application requirements. The SAW devices also typically have

quality factors that are couple orders of magnitude higher than the LC discrete resonators. Since SAW devices are pervasive in communication and sensor systems, this result might lead to a widespread acceptance of integrated radioisotope power source in the transponder and RFID applications.

4.2 Principle of operation

To increase the signal power while having better frequency control, a SAW resonator is integrated with a discharge system (Figure 4.1). The SAW resonator is connected such that the high impedance port of the SAW device is in parallel with the charge collection cantilever. The emitted charge is shared across the SAW port and the nonlinear capacitor, resulting in direct strain in the SAW device. When the cantilever discharges, a SAW pulse is generated as a result of strain release and induced displacement currents due to sudden charge release. Similar to the LC circuit RF signal, the SAW resonator energy collected over 3-5 minutes is released in nanoseconds, which excites the SAW wave on the time scale of microseconds. This results in a collected-to-released power amplification of 10^8. Hence, even a very small of radioisotope can be used to generate high power pulses. The propagating SAW wave generates charges on the output IDTs, which can be coupled to an antenna. Sensing films can be integrated between the input and output ports of the SAW resonator. With response to the surrounding environment, the mass of the sensing film will change, which creates mass-loading effects on the SAW device. A radioisotope-powered SAW sensor can be achieved by monitoring the change of the output RF SAW signal.

The self-powered SAW transponder can be modeled as an RLC circuit with a SAW resonator connected in parallel (Figure 4.2), with the components listed in Table 4.1. The circuit in the right box represents the discharge system, while the

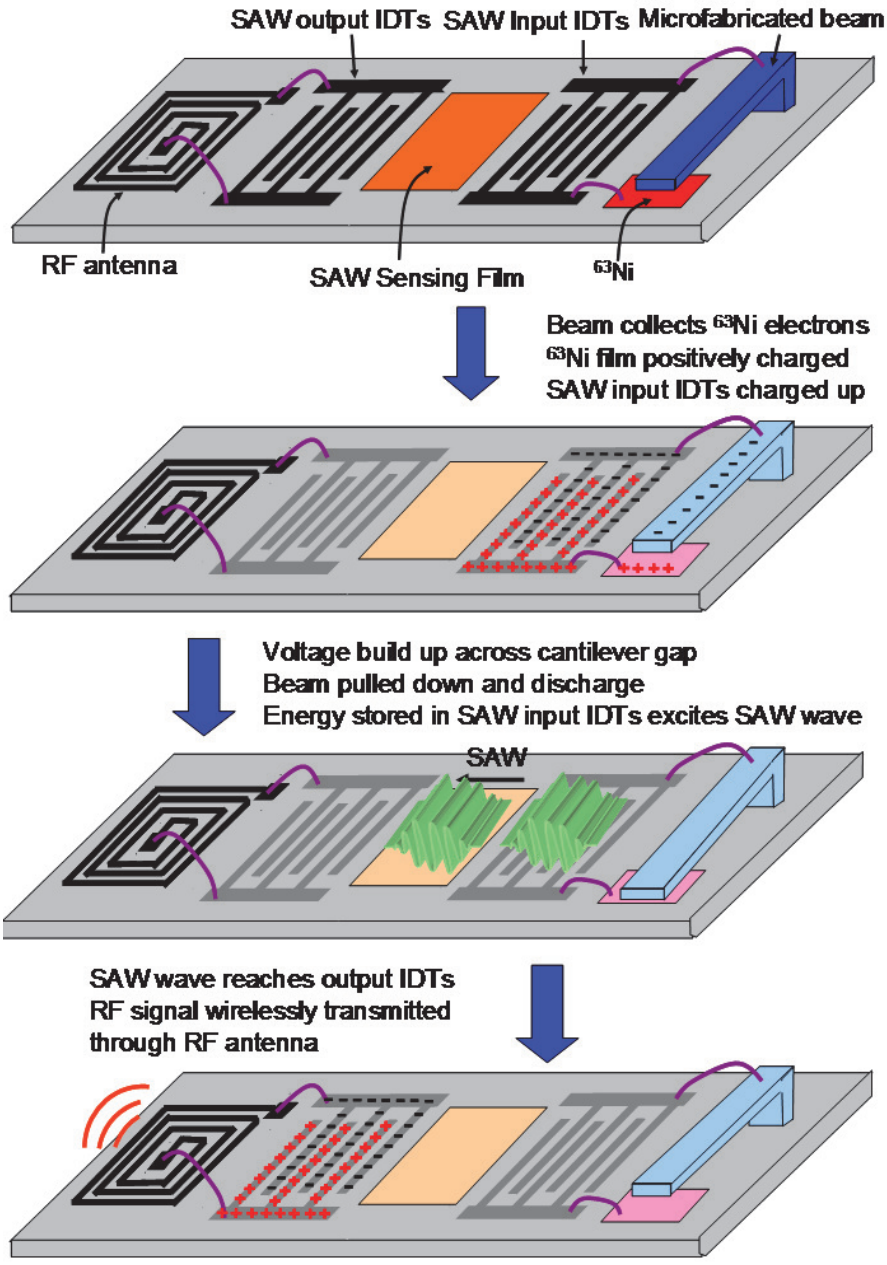

Figure 4.1: Schematic illustrating operation principle of the SAW-based radioisotope-powered RF transponder

equivalent circuit of the SAW resonator is in the left box. In the charging cycle, the electrical energy is stored both in the discharge-system capacitor and the SAW resonator's input ground-coupling capacitor, while mechanical energy is stored in the cantilever and the piezoelectric substrate of the SAW resonator. When an arc

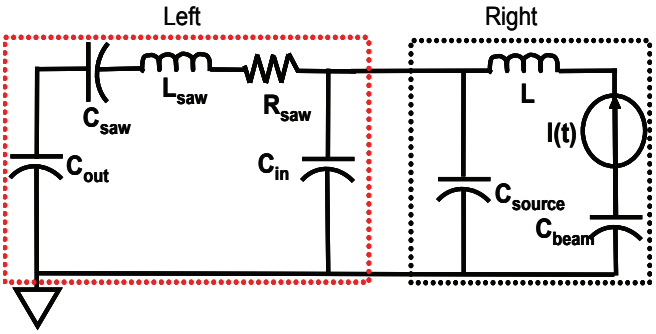

Figure 4.2: The equivalent circuit model of the SAW transponder

Table 4.1: Representations and values of R, L, C components in circuit model in Figure 4.2

Component	Representation
C_s	Source holder capacitance
C_b	Beam holder capacitance
I(t)	Air gap current
R_saw	SAW equivalent resistance
L	Discharge system inductance
C_in (t)	Input SAW IDT capacitance
C_out (t)	Output SAW IDT capacitance
L_saw (t)	ISAW equivalent inductance
C_saw (t)	Output SAW IDT capacitance

discharge occurs across the air gap, a sub-nanosecond high power current pulse is released which excites oscillations in the RLC circuit of the discharge system, at hundreds of megahertz for hundreds of nanoseconds, while at the same time the energy stored in the SAW capacitor and substrate excites the SAW resonator at its resonator frequency. Both signals are measured at the output of the SAW device with the SAW signal having a delay equal to the time needed for the signal to travel from the input to the output IDTs. The RF signal from the discharge system reaches the SAW output, through capacitive coupling without the ultrasonic delay.

4.3 Macro-size implementation and experimentally results

As shown in Figure 4.3, in a micro-size prototype transponder, a gold cantilever (5cm×0.8cm×300μm) and a ^{63}Ni source discharging system is housed inside a small glass vacuum chamber that is evacuated and sealed. It is connected to a vacuum pump, and the chamber is pumped down to 10^{-2} mTorr. Both the gold cantilever and the ^{63}Ni source are held in place with 6 mm thick Teflon plates. A 315MHz SAW resonator (RPM RP1239) is connected to the gold cantilever at its input, with the output connected to a high bandwidth oscilloscope (LeCroy WaveMast 8500) with 50-ohm input impedance. The initial gap between the cantilever and the radioisotope source is fixed at 500μm, which gives a charge time of 3 minutes.

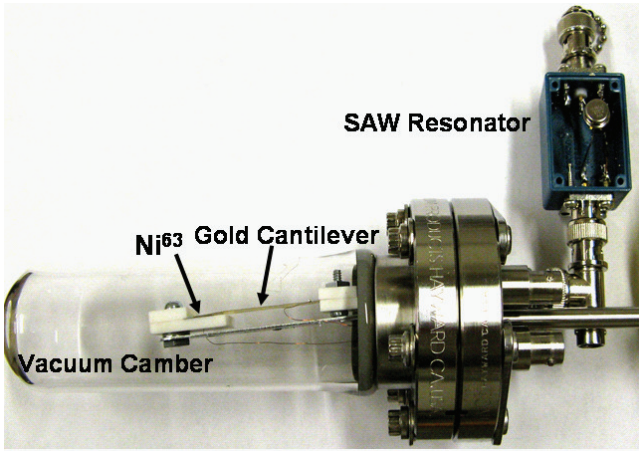

Figure 4.3: Photograph of the prototype radioisotope-powered SAW transponder

The RF signal from the transponder recorded on the scope is shown in Figure 4.4. The signal contains two parts, the RF signal generated from the LC circuit of the discharge system, which lasts about 100ns with a maximum peak-peak voltage of 5V, and the RF signal from SAW resonator, which lasts $\tilde{1}0$ μs with 0.2Vpp. The total energy in the SAW pulse is calculated to be 2nJ, while the total energy in the RF pulse is 5nJ (calculated by integrating the power over RF signal duration.)

The FFT of the transduced signal shown in Figure 4.4 is plotted in Figure 4.5.

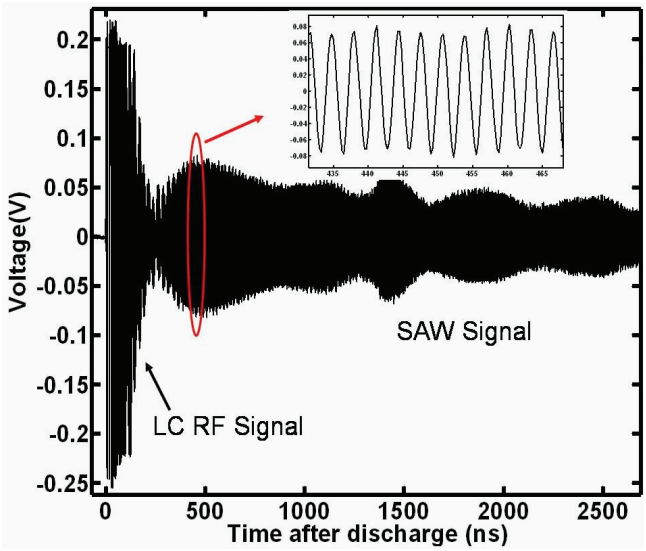

Figure 4.4: Measured RF signal waveform with 315MHz SAW resonator connected

The signal component from the 315MHz SAW device is shown with a quality factor (Q) of 1540, while the discharge LC system has a frequency of 274 MHz with a Q of 60. The SAW resonator signal has a 200ns delay, measured by comparing the signals bandpass-filtered at 315MHz and 274 MHz respectively (Figure 4.6) The system is also tested with a 434 MHz SAW resonator. The 434 MHz SAW signal with a quality factor of 1560 and a 277 MHz (Q = 70) discharge RF frequency are detected.

4.4 Micro-size implementation and experimentally results

Single crystal cantilevers, 30μm thick, with lengths of 4mm to 8mm were micromachined using a two-step deep reactive ion etch (DRIE) process on a SOI wafer, and assembled alongside a 1.5 millicurie ^{63}Ni source plate that is housed inside a 1-cm$\times$1-cm$\times$0.5-cm vacuum package (Figure 4.7). The SAW resonators are fabricated with aluminum (500nm thick) lift-off process on 128^o Y-cut lithium niobate wafers. SAW resonator devices of various frequencies are fabricated with

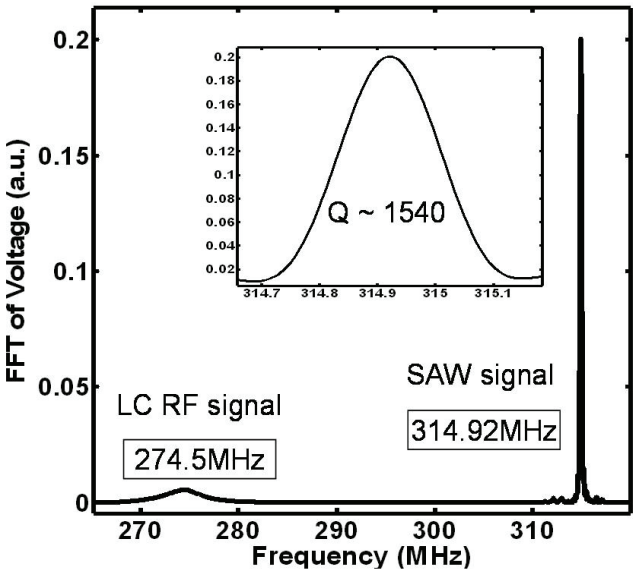

Figure 4.5: Frequency of the RF signal with 315MHz Saw resonator connected

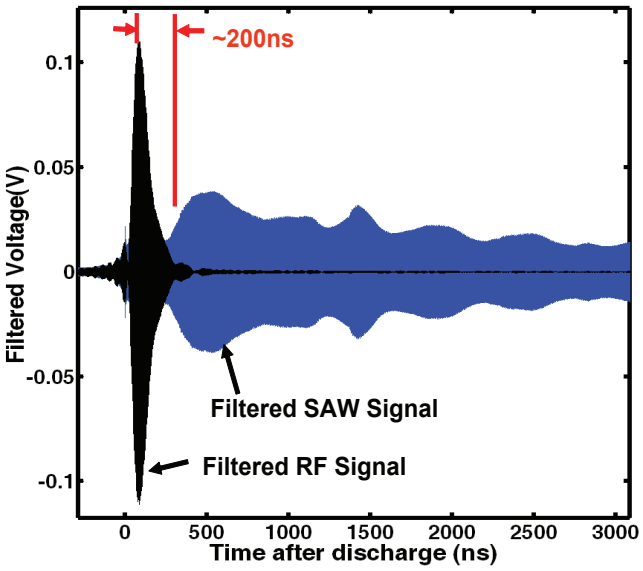

Figure 4.6: Bandpass-filtered signals illustrating the SAW resonator signal delay

35 pairs of interdigitated transducers at both input and output ports. The vacuum package is pumped down to 10^{-5} Torr and sealed by melting a solder layer on the edge of the package.

With a 100MHz SAW resonator connected to the ^{63}Ni discharge system, the SAW RF output signal is measured on a 50 ohm oscilloscope load, while the RF

output from the discharge system is measured wirelessly with an antenna (Figure 4.8). With a beam length of 5mm, the RF signal from the discharge system has a frequency of 1.31GHz with a low quality factor of 40. The SAW RF signal with a maximum output power of 5mW and duration of 10μs is achieved. With a quality factor of over 400, the RFID signal can be detected from hundreds of feet away with the same SAW tuned receiver. The RF signal at the cantilever is also measured for the same discharge event, and a signal delay of 750ns is detected for the SAW signal (Fig. 5),which is due to the 3mm gap between its input and output IDTs.

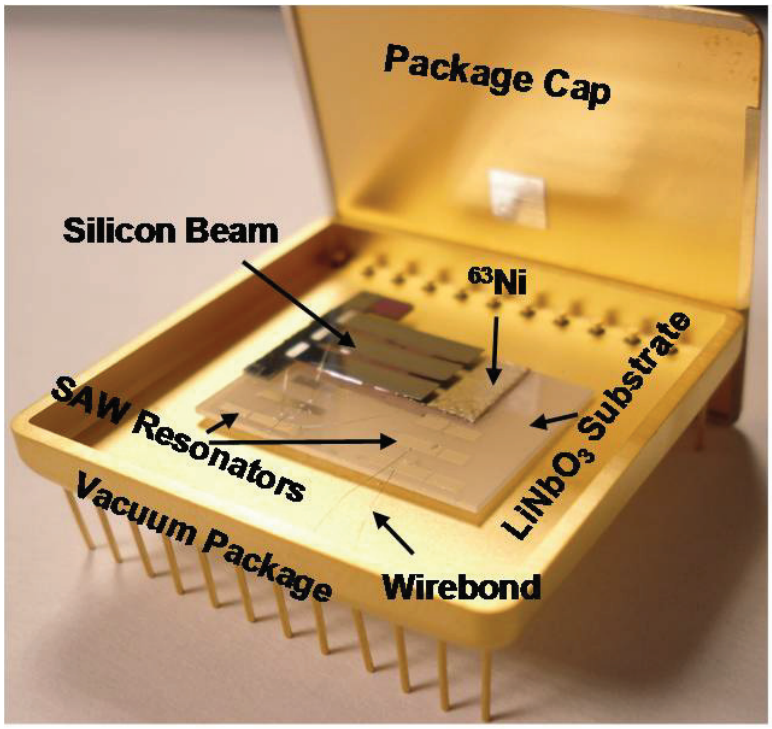

Figure 4.7: Photograph of the microfabricated integrated RFID device inside a 1 inch^2 vacuum package

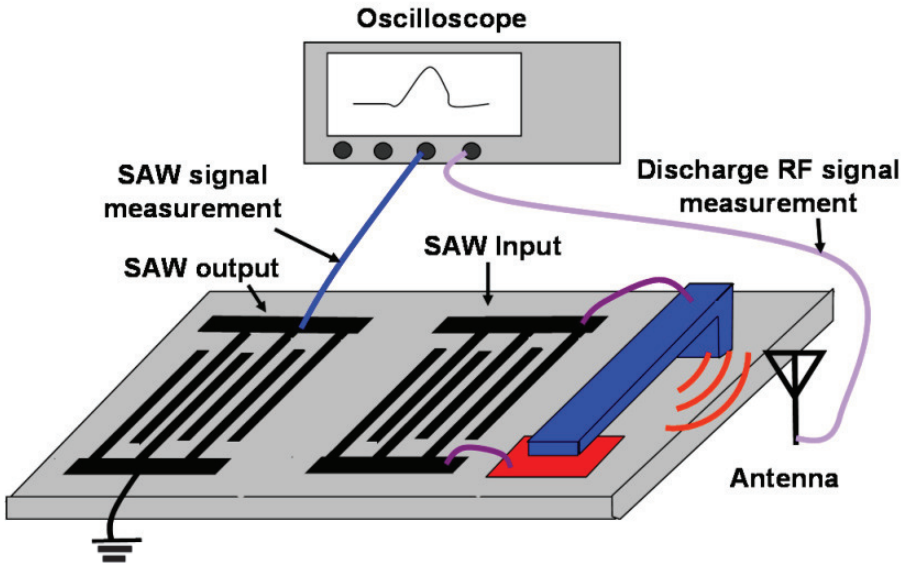

Figure 4.8: Schematic illustrating the measurement set for the RF signals from SAW and discharge system

4.5 Radioisotope-powered SAW sensor study

The SAW transducer frequency can be modulated by integrated or attached mass-sensors or a RFID code. One can integrate sensing films or coded floating IDT fingers between the excitation and receiving IDT pairs. Hence, in principle a self-powered sensor node and RFID are possible with our RFID. As a proof of principle, aluminum fingers are deposited between the input port and one of the output ports to create the mass-loading effects, while the signal is measured at a second output port is used as reference (Figure 4.10) After the cantilever discharges, SAW signal generated at the input port propagate towards both output ports, and due the mass-loading effects, a frequency shift of 14 kHz at 100MHz center frequency is produced at the output with loading fingers (Figure 4.11), generating beat notes at the output. For future research, SAW sensors will be fabricated and integrated

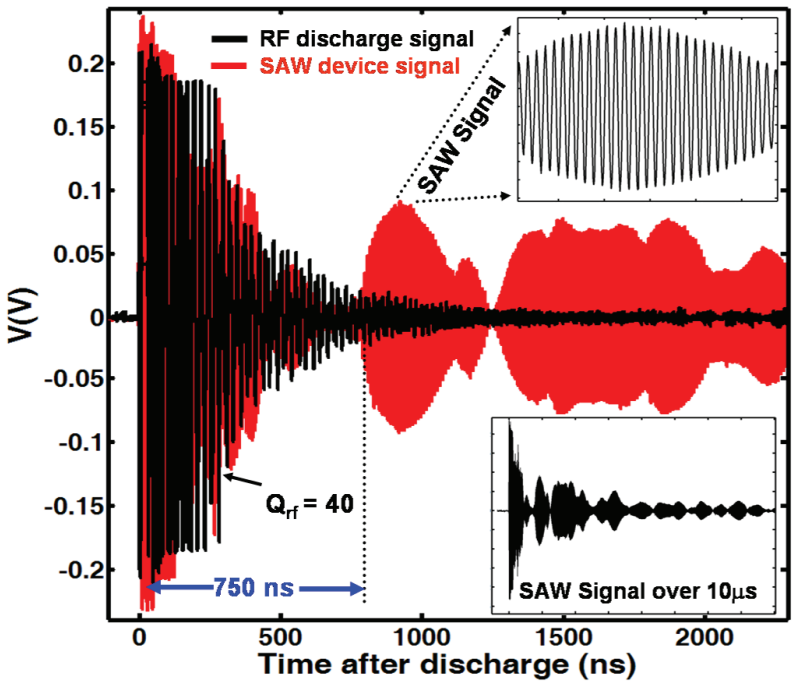

Figure 4.9: RF discharge signal measured at the discharge cantilever compared to the signal from the SAW devices show a 750ns SAW delay

into the system to realize a complete miniature self-powered wireless sensor node.

4.6 Efficiency study of the integrated SAW RF transponder

Increasing the voltage and energy output from the SAW resonator can improve the distance over which a RF-link can be established. We want to maximize the radioactive-to-SAW energy conversion efficiency, which can expressed as energy in the detected SAW wave divided by the collected radioactive energy

$$\eta = \frac{E_{SAW}}{E_{rad}} = \frac{E_{SAW}}{E_{electrical}} \frac{E_{electrical}}{E_{rad}} = \frac{\frac{1}{2} Q \frac{V^2}{R} \frac{1}{f}}{T_{rec} E_e A} \tag{4.1}$$

where E_{SAW} and E_{rad} are the SAW output energy and radioisotope input energy

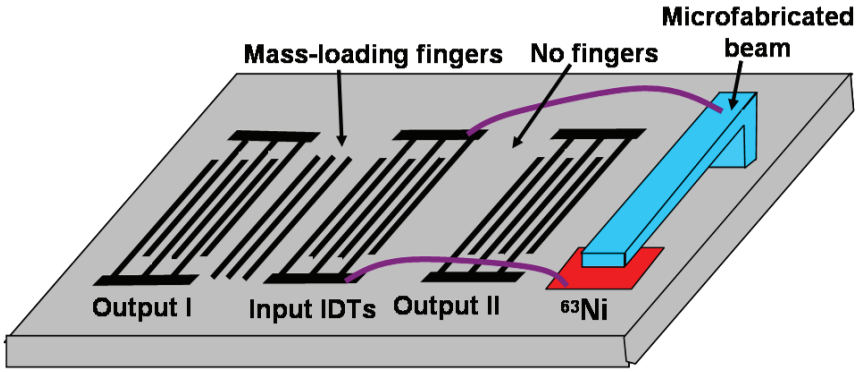

Figure 4.10: Schematic illustrating the SAW resonator with mass-loading between input port and one of the output ports

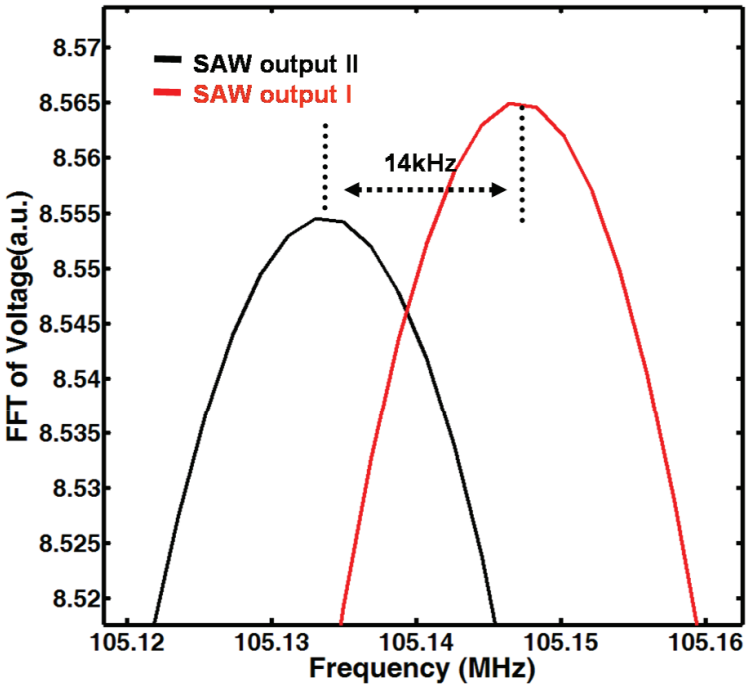

Figure 4.11: Measured RF signal frequencies at both output ports of the SAW resonator whose resonant frequency is about 100MHz

respectively. Q and V and the quality factor and voltage of the output SAW signal respectively, R is the load resistance (50 ohm) , T_{rec} (180s) is the reciprocation period of the discharge system, and E_e and A are the average electron energy (17 keV) and activity of the radioactive source (1.5 mCi/cm^2). The prototype device reported here has a conversion efficiency of 0.06%.

As shown in Equation 4.1, the overall conversion process can be divided into radioactive energy to electrical energy conversion and electrical to SAW energy conversion. The radioactive to electrical energy conversion has been studied in Section 2.8,where there is an optimal gap for best conversion efficiency. In this section, we are focusing on the electrical energy to SAW energy conversion. With SAW device connected to the system, the electrical energy is stored across the air gap, across the input port of the SAW resonator, and across other capacitances in the system. Since only the electromechanical energy stored across the input port of the SAW device contributes to the output RF signal, SAW input capacitance should be increased while other capacitances need to be minimized.

CHAPTER 5

ULTRAHIGH EFFICIENCY AND POWER DENSITY MICROMACHINED THIN SILICON-CARBIDE BETAVOLTAICS

We report on the first demonstration of an 11.2% ultra-high efficiency 50um-thick thinned-down silicon carbide betavoltaics under ^{63}Ni irradiation. The efficiency can be further increased to 23.6%, while the device thickness can be decreased to below 30um. Comparing to the best SiC betavoltaics reported so far [45][46], our devices have an efficiency improvement of 3-4X, with a fuel fill factor improvement of 8-10X, which will lead to an overall power density improvement of 30-40X. Comparing to the best available planar silicon betavoltaics [47], our devices have a power density improvement of 100X (6X in efficiency, and 16X improvement in fuel fill factor.)

5.1 Introduction

With very high energy densities of 1-10 MJ/cc [48] (compared to 1-20 kJ/cc for conventional electrochemical and hydrocarbon fuels [49]), and long half-life of 1-100 years, radioisotope fueled batteries are ideal for applications requiring compact, long lifetime power supplies, such as remote sensing and implantable devices. Furthermore, low energy emitters (^{63}Ni, ^{147}Pm, etc.) have little or no safety concerns, and Promethium-147 powered betavoltaics has been implanted inside humans for powering cardiac pacemakers [47].

To achieve compact size batteries, the power density of the device should design to be as high as possible. The power output density of a betavoltaic battery can be expressed as following

$$P_{out} = P_{fuel} FFF \eta_{fuel} \eta_{\beta} \tag{5.1}$$

where P_{fuel} is the fuel power density, FFF is the fuel fill factor (volume percentage of the radioisotope fuel), η_{fuel} is radioisotope thin-film emission efficiency, and η_β is betavoltaic conversion efficiency, P_{fuel} and η_{fuel} are determined by the radioisotope material. While higher energy isotopes such as ^{137}Cs and ^{90}Sr have higher fuel power density, due to their high energy, significant shielding is needed, which decreases the overall power density of the battery. ^{63}Ni emits β-particles with an average kinetic energy of 17.3keV, and a penetration depth of less than 10μm in most solids. As a result, devices powered by ^{63}Ni thin-films can be deployed safely with millimeter or microscale shields. In this paper, we are focus on improving FFF and η_β to maximize the power density of a betavoltaic battery.

Different techniques of improving the FFF of a betavoltaic battery by patterning and etching of its active device layers have been previous reported [50][19]. However, in both those cases, the leakage currents were significantly increased due to the damage to the semiconductor materials in the etching process, hence very low conversion efficiencies were reported. In our design, only non-active substrate is etched away, so FFF can be improved without sacrificing the conversion efficiency.

The thicknesses of the SiC and silicon wafers ranges from 300μm to 500μm, while the top 20μm is the active functioning region for a betavoltaic battery (Figure 5.1.) Therefore, regular planar betavoltaics have over 90% of their volume wasted, while a FFF improvement of 8X can be achieved by thinning down the non-active substrate to 30μm. Furthermore, in a planar device, all the electrons irradiated away from substrate are wasted, which is 50% of all electrons. By stacking thinned-down devices together, all the electrons will be utilized, which decrease the radioactivity needed for a battery. Besides a higher FFF values, less radioactivity also provide a safer device.

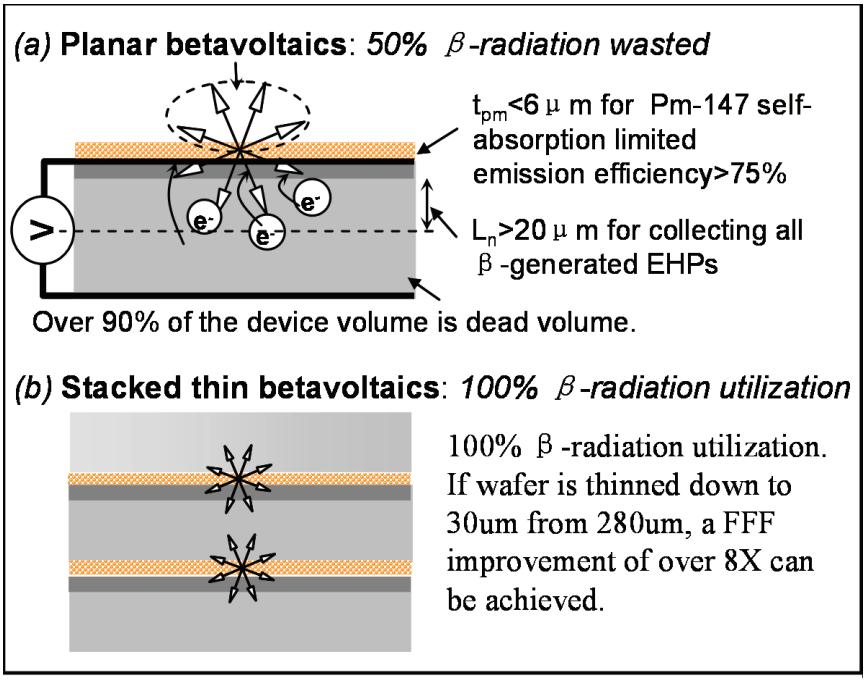

Figure 5.1: Schematics illustrating the design and advantages of the thin SiC betavoltaic design

5.2 Fabrication of SiC betavoltaics

The process flow of the thin SiC betavoltaics is illustrated in Figure 5.2. The SiC wafer substrate has too many defects to be the active device layer, so a 19μm thick of n-doped SiC epitaxial layer followed by a 0.25μm thick of p-doped SiC epitaxial layer are grown on top of the substrate as active device layers. For prototype devices, 1cm^2 dies are thinned down to 50μm from 280μm thick after device isolation etching on the wafer. The devices are metalized with Ti/Al on the p-doped epi-layer and Ni on the n-doped substrate, with RTA followed to ensure good ohmic contact.

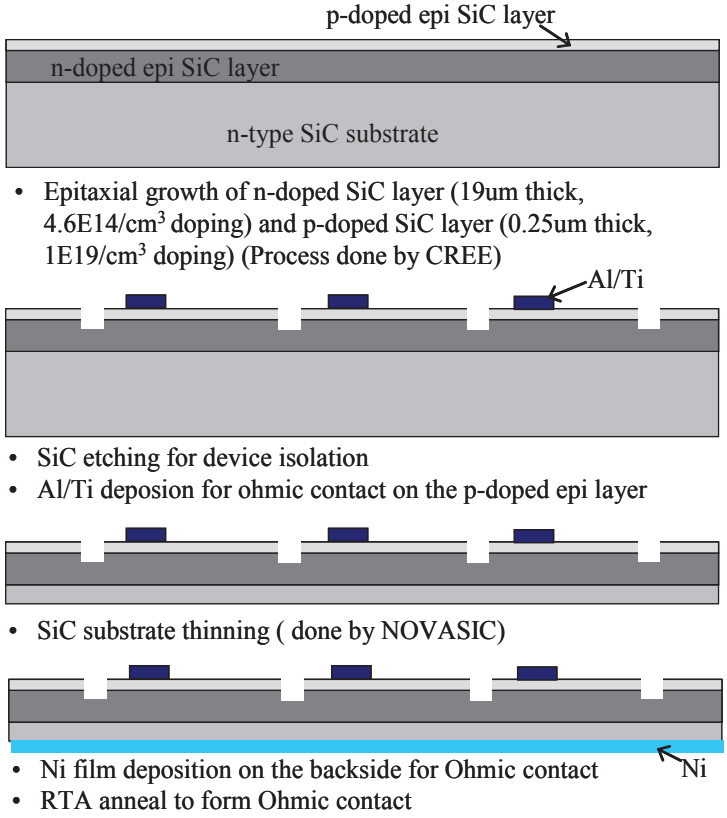

Figure 5.2: Fabrication Process of the thin SiC betavoltaics

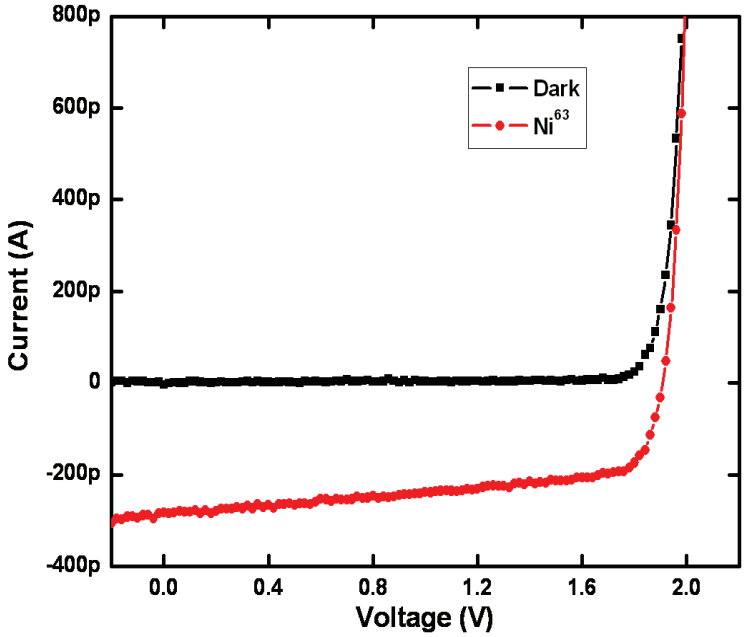

Figure 5.3: Measured IV characteristic of regular-thickness SiC betavoltaic under ^{63}Ni electron irradiation

5.3 Experiment results of thinned-down betavoltaics

Energy conversion characteristics of regular-thickness SiC betavoltaics were first measured under electron irradiation from ^{63}Ni source, which has a radioactivity of 1.5mCi/cm^2. The IV curves of a device with 1mm by 1mm area are plotted in Figure 5.3. Under electron irradiation from ^{63}Ni, the device has a short-circuit current of 300pA with open-circuit current voltage of 1.9V. An ultra-high conversion efficiency of 22.3% was achieved (341nW of output power vs. 1.53nW of input power at 1.76V,) which is almost 4 time of the best results previously reported in [45].

The betavoltaic devices are further characterized in a scanning electron microscope by irradiating them with 20pA-2nA electron beams (corresponding to 3milliCurie- 300milliCurie of radioactivity) accelerated at voltages up to 30kV (SEM limit). The conversion efficiency of device is low at low electron energies

(Figure 5.4.) This is due to the energy loss for electrons to go through the heavily P-doped SiC carbide layer, where the electron-hole pairs generated by the incending elections are quickly recombined. As the electron energy increases, the percentage of the energy wasted in the P-doped SiC decreases. Therefore, the conversion efficiency increases until it reaches the maximum efficiency for the betavoltaic device, which is 23.6%. Further increase of the electron energy could lead to decreasing of the overall conversion efficiency, if the electron penetration depth in the SiC is larger than the diffusion length of the EHS in the low n-doped epitaxial layer. The electron-hole pair (EHP) multiplication factor (number of EHPs per input electron) is also plotted in Figure 5.4. A near straight line at high energies indicates the device could work at even higher input electron energy ($\geq$30keV) with the same efficiency. Therefore, ^{147}Pm, which has a higher average electron energy (62keV) and higher power density (2.05W/cc, comparing to $\tilde{1}$3.4mW/cc for ^{63}Ni) can be used as radioisotope source to further increase the power density of the betavoltaic battery.

To demonstrate of concept of thin-down betavoltaics, a 1cm $\times$ 1cm $\times$ 280μm-thick SiC betavolatic die is thinned down to 50μm thick from the backside of the substrate (as shown in Figure 5.2,) which gives a over 4X improvement on the FFF of the devices. The thickness of the devices can be further thinned down to 30μm, which could provide a FFF improvement of 8X. The thinned-down SiC betavoltaic is tested under ^{63}Ni irradiation, but only 11.2% conversion efficiency is achieved (figure 5.5). That is due to the lack of protection for the p-doped epitaxial layer in the wafer thinning process. The damage to epitaxial layers causes higher leakage current, which lowers the open-circuit voltage and the conversion efficiency. With a carrier wafer to protect the epitaxial layers in wafer-thinning process, a conversion efficiency of 22.3% is expected for the thinned-down SiC betavoltaics with ^{63}Ni

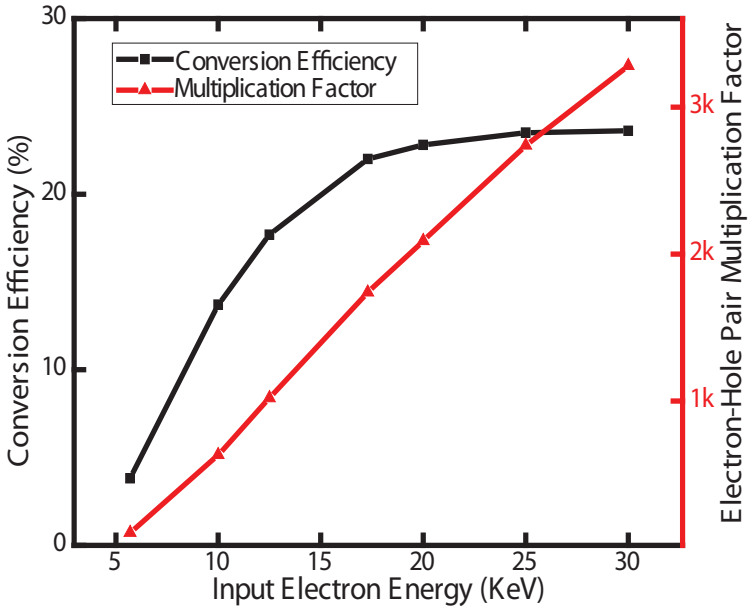

Figure 5.4: Measured conversion efficiency and EHPs multiplication factor at different input electron energy for the regular-thickness device

irradiation. Even with the prototype device, a powered density increase of 170% is achieved.

5.4 Conclusion

In this chapter, we report a high efficiency SiC betavoltaics of 23.6% under ^{63}Ni irradiation, which is about 4 times of the best results reported in the literature. To further increase the power density, the SiC betavoltaics die is thinned down to 50μm, which gives a FFF improvement of over 4 times. The thinned-down device has a conversion efficiency of 11.2%, due to the damage to the device layers in the wafer thinning process. However, it still gives a power density improvement of 10 times over the best SiC betavoltaics reported so far. With device layers protected in the wafer thinning process, the efficiency can be increased to 23.6%, while the device thickness can be decreased to below 30μm. Therefore, an overall power

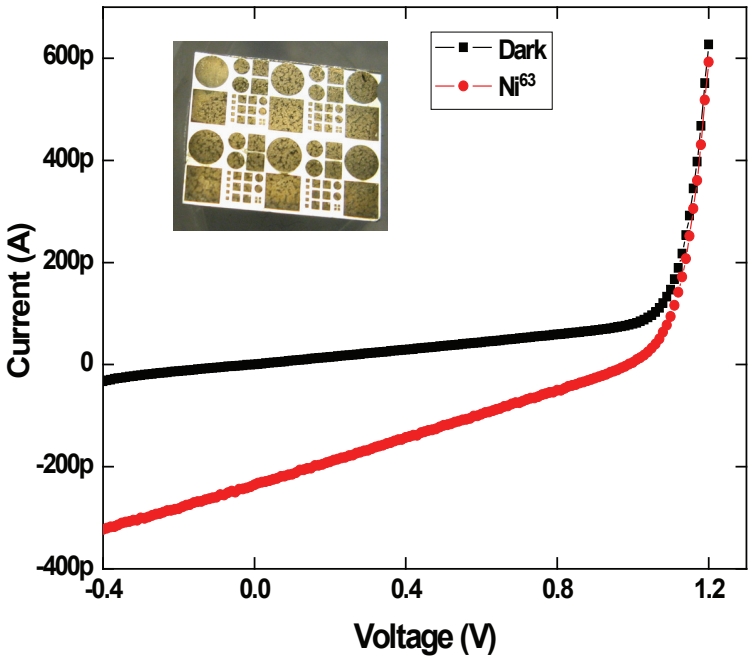

Figure 5.5: Photograph and measured IV characteristic of 50μ m-thick SiC betavoltaic under ^{63}Ni electron irradiation

density improvement of 30-40X can be achieved.

CHAPTER 6

MICROFABRICATED ULTRASONIC MOTOR

In this chapter, we studied the nonlinear subharmonic traveling resonant modes which generate the rotational motion on the surface-macromahcined ultrasonic micromotors. Actuated by a die-attached PZT plate, when the resonant frequency of the one of the stator's vibration mode is close to PZT plate's thickness mode resonance (4.2MHz), rotating wave is generated on the stator. Driven at 3.78MHz, the rotating wave on the stator with 820μm diameter is optically detected and spatially characterized with an optical microscope. Together with laser interferometer measurements, two subharmonic modes are obtained, (1, 13) traveling mode at 1.78MHz and (0, 20) standing mode at 2MHz. The experimental results are further verified with finite element simulation. The traveling wave is acoustically coupled to the rotor without sliding to generate motor rotation. To study motor rotation control, signal bursts with various number of cycles are applied to the motor, and rotation rate of 2 degree per thousand cycles with angular control of as little as 0.1 degree is achieved.

We also studied the actuation, vibration and rotation properties of acoustically-driven surface-macromahcined ultrasonic micromotors with different stator dimensions to achieve optimized performances. The voltage threshold for rotation and maximum rotation speed of the motor varies with the size of the stator. While larger stator (820μm) has lower rotation threshold (3.5V), its maximum rotation speed (180 rpm) is significantly lower than smaller stator (740μm), whose maximum rotation speed is over 320 rpm with rotation threshold of 8.5V.

6.1 Introduction to the ultrasonic motor

Bulk-PZT driven micromachined ultrasonic motors have been previous reported by our group [51] [52]. While the existence of subharmonic traveling waves have been proposed to generate the motor rotation, they have not been visualized experimentally. In this paper, subharmonic traveling and standing waves are experimentally verified and characterized, in order to perform modeling, design, and optimization of the surface micromachined ultrasonic motor.

The ultrasonically-driven surface-micromachined micromotor can be integrated with an optical reflector plates, sensors, and optical sources such as a VCSEL (Vertical Cavity Surface Emitting Laser) (Figure 6.1). Ultrasonic motors can be used to realize compact rotating platform carrying stages for micro-optics, directional sensing etc. With potential applications in directional sensing and communications, surface-microfabricated rotating stage is easily integrated with optics microsystems such as lab-on-a-chip applications. In the motor presented here, with multi-layer polysilicon fabrication process and less than 5V operation, the rotating stage has low cost, low power consumption, and high integrate-ability with other MEMS devices.

6.2 Fabrication of the ultrasonic micromotor

The ultrasonic motor is fabricated using the SUMMiT V polycrystalline silicon surface micromachining process. The thickness and diameter of the rotor are 2.5μm, 980μm respectively.The diameter of the anchor is 280μm, and the thickness of the stator is 2.25μm, while diameter of 820μm. After the system is released, a rectangular PZT-4 plate (3.2mm $\times$ 3.2mm $\times$ 0.5mm) is bonded to the back of the die with cyanoacrylate adhesive (Figure 6.2). The adhesive layer thickness

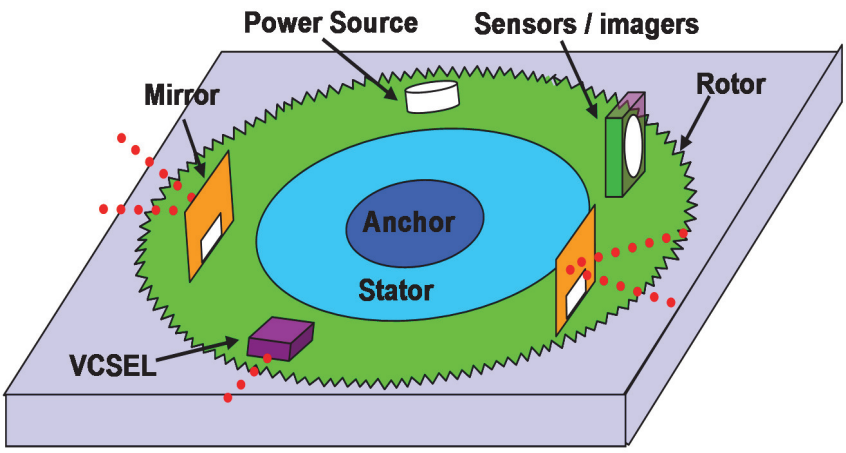

Figure 6.1: Schematic illustrating the ultrasonic micromotor with optical and sensing components integrated on the rotor for directional sensing and communication

is designed to be as thin as possible while ensuring a strong bonding between the silicon die and PZT plate to reduce the coupling loss. The size of the PZT plate is much larger comparing to the size of the silicon die (1.2mm $\times$ 1.2mm $\times$ 0.5mm) to provide easy handling and space for soldering. However, with PCB board integration and wirebonding, the size of the PZT can be significantly reduced to further increase the driving efficiency and ultrasonic motor density.

6.3 Experimental setup

The PZT plate is excited with a single frequency signal with frequency at 3.78 MHz up to 10 volts. For optical experiments, the motor is placed under the microscope with a tilted angle in the z-plane. The out-of-plane vibration can therefore be effectively captured and analyzed. The vibration amplitude of the stator and motor are measured with laser interferometer (Polytec-PI). For vibration waveform and frequency measurements, the signals are recorded with an oscilloscope and the FFT of the signals are then analyzed. To measure the vibration mode of the stator at a certain excitation frequency, a 2D scan is performed across the stator while

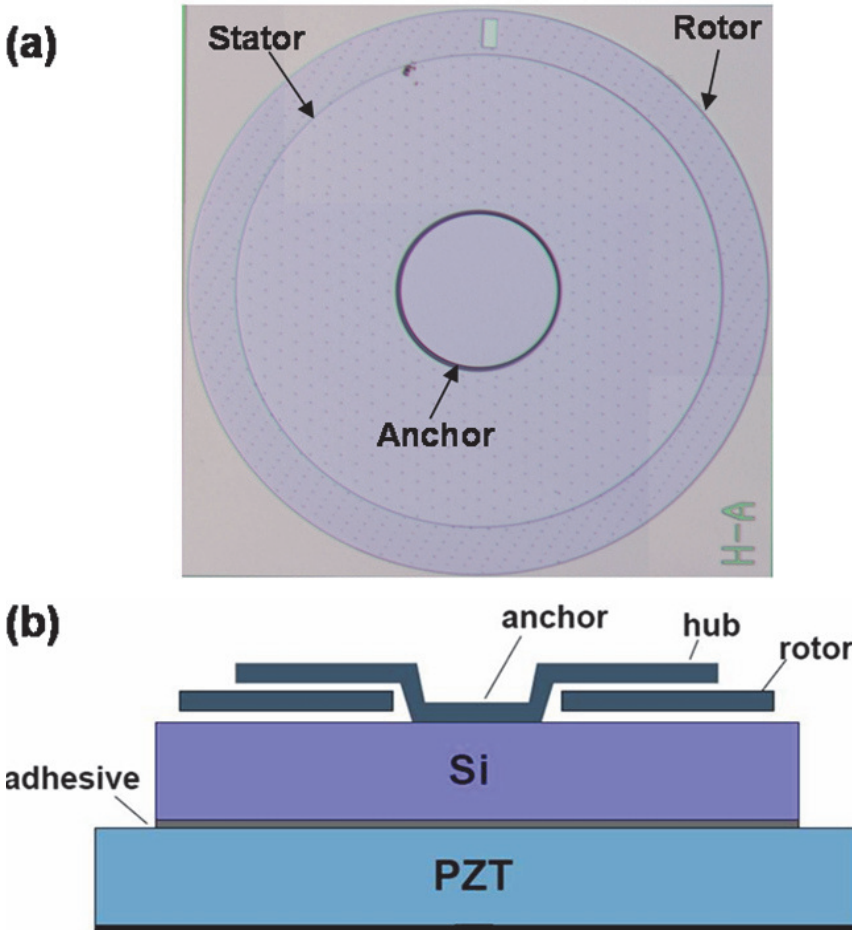

Figure 6.2: (a) Photo of the micromotor (b) Cross section view of the motor measurement setup

the laser interferometer signal is locked to the excitation signal with a locking amplified. The vibration amplitude and phase information are then recorded at each scanning points to map out the mode shape. As shown in Figure 6.2, a rectangular slit is design on the rotor for rotation speed measurements. When the rotor is rotating, the vibration amplitude of the rotor is significantly larger than that of the substrate. Therefore, when the slit on the rotor goes through the laser beam, a dip on the vibration amplitude is observed. The rotation speed can then be determined by measuring the time between two adjacent readings.

6.4 Linear vibration of the stator

When a sinusoidal signal is applied to the PZT plate, the vibration of the plate is transferred to the silicon substrate through the adhesion layer. The vibration of the silicon substrate is then further transferred to the stator through the anchor(Figure 6.3). If the sinusoidal signal frequency is equal to one of the natural frequencies of the stator, large vibration amplitude is observed due to the high quality factor of the polysilicon stator even if it is operating in air. For the PZT-4 plate used in the experiment, its thickness mode resonate frequency is at 4.2MHz. While the silicon die causes some attenuation at the thickness mode (Figure 6.4), which indicates strong coupling between the PZT and silicon die, and energy is transferred to the silicon die. Therefore, one of the resonant frequencies of the stators needs to be designed around the thickness resonance of the PZT plate to provide maximum vibration amplitude with minimum amount of power consumed. The (i, j) mode resonant frequency of a free-clamped annular plate can be expressed as [53]

$$f_{ij} = \frac{\lambda_{ij}^2}{2a^2\pi}\sqrt{\frac{Eh^3}{12\gamma(1-\upsilon^2)}} \tag{6.1}$$

where a is the stator radius; b is the anchor radius, h is the stator thickness; E is

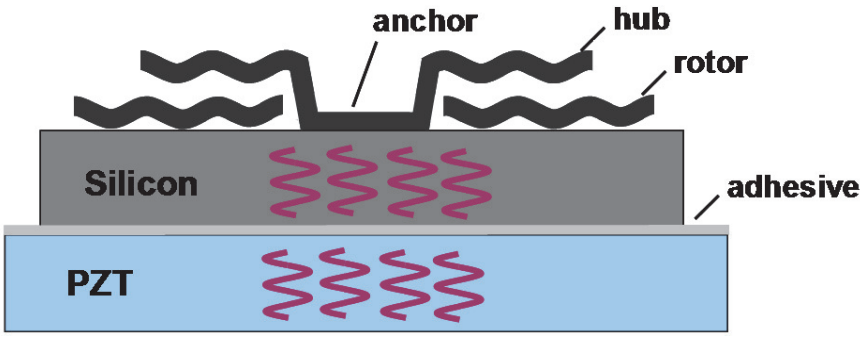

Figure 6.3: Schematic illustrating the energy transfer in the ultrasonic motor actuation process

the Young's modulus; υ is the Poisson's ratio; γ is the mass per unit area; and λ_{ij} is the dimensionless frequency parameter, which is determined by the mode number and the ratio between the radius of stator and anchor. As shown in Equation 6.1, the resonant frequency of stator is determined by the radius of the stator and its equivalent Young's modulus. For motor with 820μm stator, excited at 3.78MHz, The vibration mode shape of the stator is measured to be (5, 1) mode with ANSYS simulation confirming the measured results (Figure 6.5).

6.5 Nonlinear vibration of the stator

6.5.1 Optical Interferometer Measurement

For the motor with 820 μm diameter stator, as the excitation voltage increases to 1.5V, subharmonics frequencies are excited on the edge of the stator, with frequency of 1.78 MHz and 2 MHz (Figure 6.6). The stator vibration amplitude at which nonlinear vibration occurs is 50nm. Although the signal at 3.78MHz actuation frequency can still be detected, the majority of the energy has been transferred to the subharmonic frequencies. The subharmonic nonlinear frequencies could come from period-doubling bifurcations of the system with

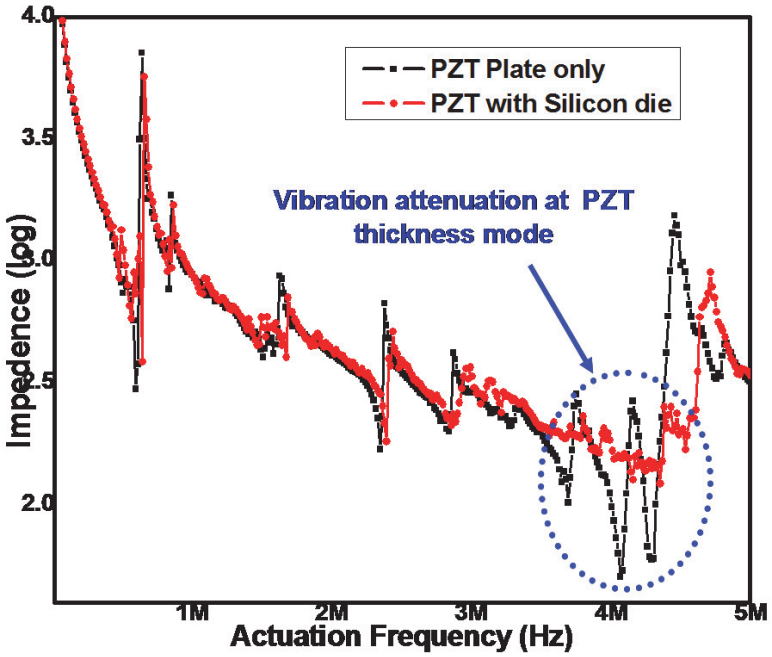

Figure 6.4: Measured impedance of the PZT plate with and without silicon die attached on the bottom, demonstrating the thickness mode at around 4 MHz

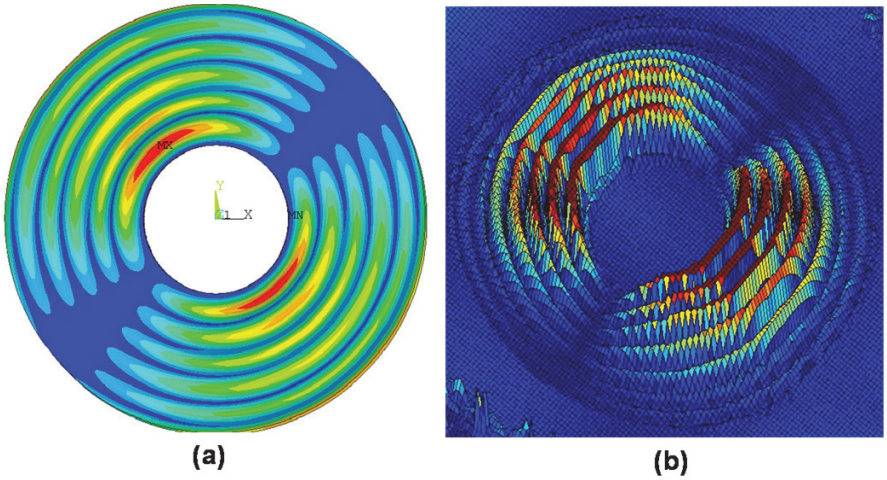

Figure 6.5: (a) Simulated and (b) measured vibrated mode of a micromotor with 820μm stator actuated at 3.78MHz

frequency splitting caused by the etch hole and other imperfections on the stator. The orthogonal mode of the stator at (5, 1) mode will have slightly different frequencies. With one-to-one internal resonance, both modes can be excited and phase-locked, generating a traveling wave on the stator [54][53]. 2D scan is performed with the detected signal locked to the actuation frequency and the two subharmonic frequencies to obtain the mode shapes of the vibration at those three frequencies. As shown in Figure 6.7(a), on the edge of the stator, the (5, 1) linear vibration mode is distorted on the outer edge at 3.78MHz with nonlinear vibration. For subharmonic frequencies, at 1.78MHz, no standing waveform is detected, which indicates the subharmonic mode could be a traveling mode. At 2 MHz, standing mode (0, 20) is detected (Figure 6.7(c)), which agrees with the finite element simulation results of the stator (Figure 6.7(d)).

6.5.2 Direct Optical Measurement

While 2D scan from laser interferometer can be used to make quantitative measurements on the mode shape of the standing waves, to verify and obtain traveling wave modal shapes, transient measurement is needed. With optical microscope, the stator vibration is studied at various actuation conditions, wide side illumination. At 3.78MHz actuation frequency, as the voltage increases from 0V to 10V, the linearly driven (5, 1) mode is first observed (Figure 6.8(a)). As nonlinear vibration starts, (1, 13) subharhonic traveling wave appears on the stator (Figure 6.8(c)). The traveling wave couples to the rotor without sliding for rotation speed up to 500 rpm. Finite element simulation confirmed the existence of (1, 13) at 1.78 MHz on the stator (Figure 6.8(d)).

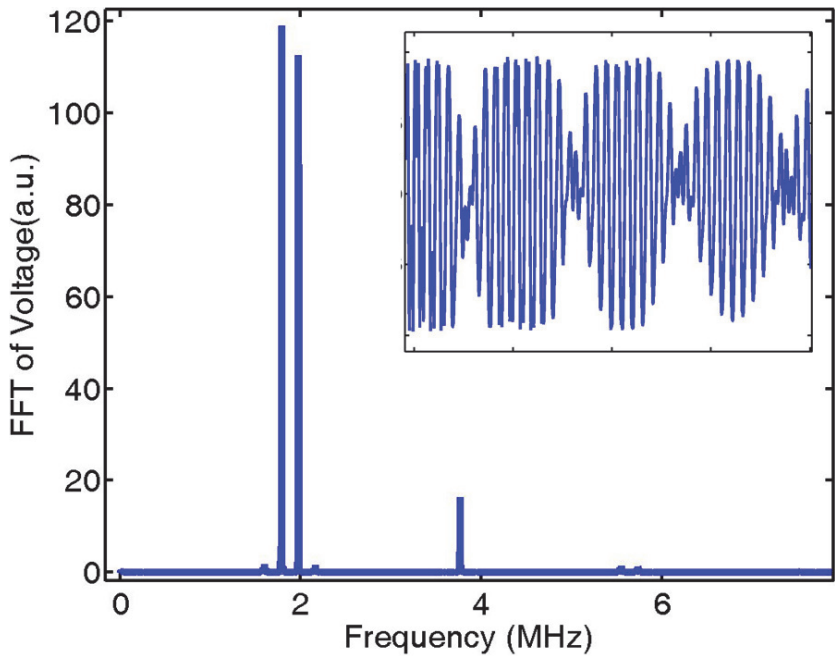

Figure 6.6: Waveform and frequency of the subharmonic signal for the stator with 820μm diameter while PZT is actuated at 3.78MHz

6.6 Experimental measurements of the micro ultrasonic motor

To study the rotation characteristics of the motor, the rotation speed is measured by monitoring the interferometer signal pulses generated every time the slit on the rotor moves through the laser. Although the nonlinear vibration starts at 1.5V, due to static friction between the rotor and the substrate it rests on and the coupling loss between the stator and rotor, the motor starts rotating at 5.5V actuation voltage, when the rotational force on the rotor overcomes the static frication force. The rotation speed increases with excitation voltage at first due to the increase of rotational force on the rotor is greater than the increase of kinetic friction force. However, the rotation speed levels off when the increase of friction force begins to dominate. The maximum rotation speed is 510 rpm with 10V actuation (Figure 6.9.)

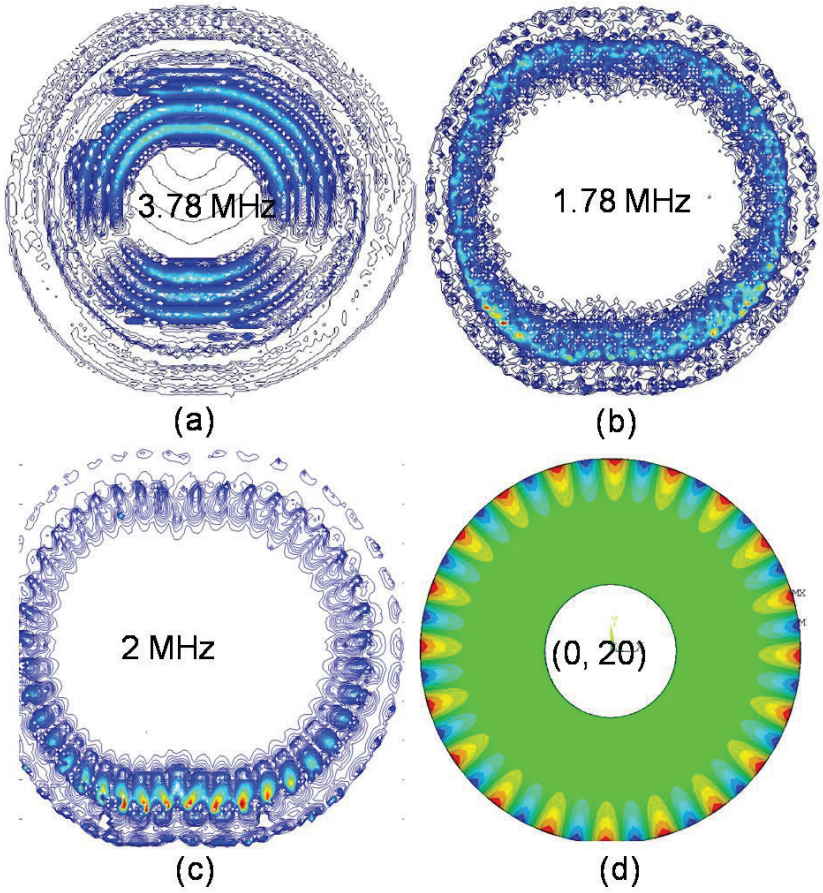

Figure 6.7: (a) Mode shape at 3.78MHz actuation frequency when nonlinear vibration exists (b) Mode shape at 1.78 MHz subharmonic frequency, (c) Mode shape at 2 MHz subharmonic frequency (d) Simulated mode stator mode shape at 2.0 MHz

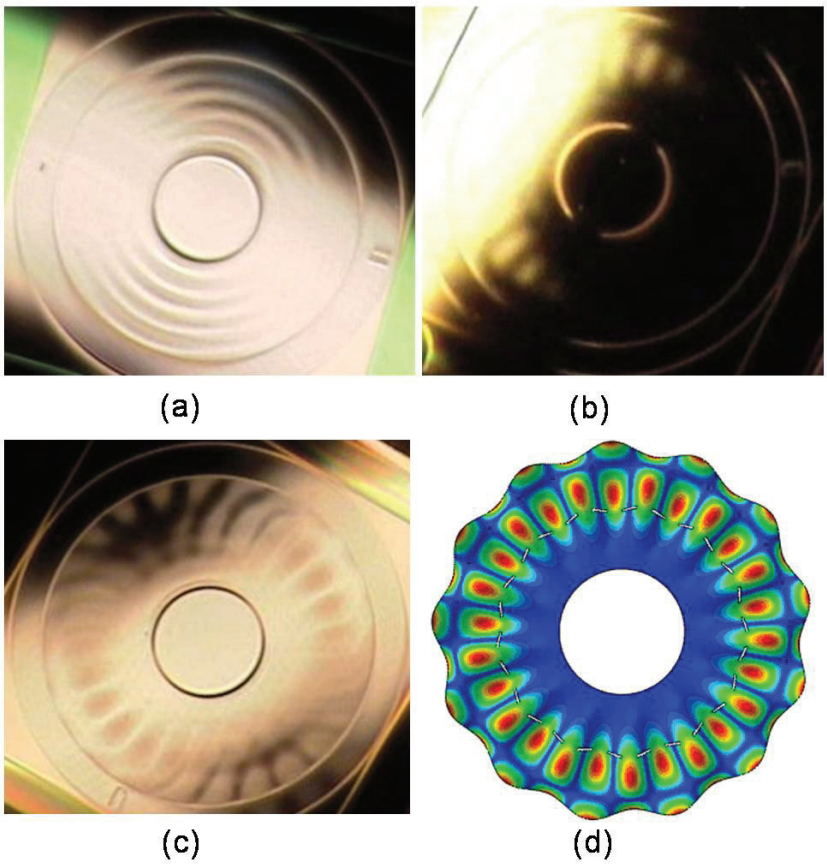

Figure 6.8: Optical image of (a) (5,1) linear vibration mode shape, (b) (c) (1,13) nonlinear traveling wave mode shape. (d) Finite element simulation of mode shape at 1.78 MHz

For directional sensing and communication applications, accurate rotation control is critical for alignment of components on and off the rotation platform. To investigate that, 9V signal bursts with various number of cycles are used to drive the motor with the rotation angle due to each burst measured using a protractor. A rotation angle of 2 degree per thousand cycles with accuracy of 0.1 degree is achieved (Figure 6.10), and the accuracy could be further increased with more accurate angle measurement equipments.

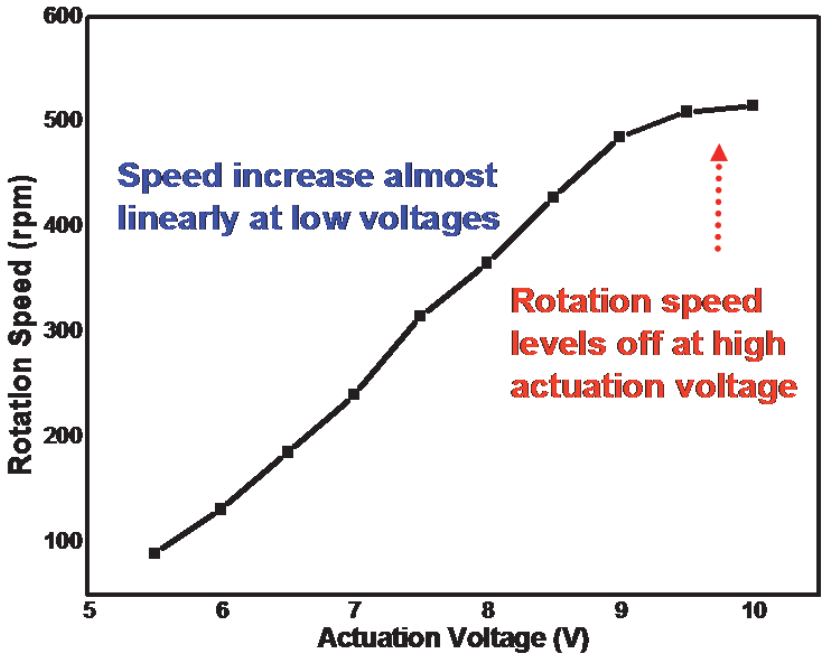

Figure 6.9: Rotation speed of the prototype motor at different actuation voltages. Motor actuated at 3.78 MHz

6.7 Motor optimization study with various hub diameters

The performances of the micromotors with different sized stator are studied to optimize the motor design. The thickness and diameter of the rotor, the diameter of the anchor, and the thickness of the stator are kept the same, while the diameter of the stator varies from 740μm to 820μm. As shown in Equation 6.1, the resonant

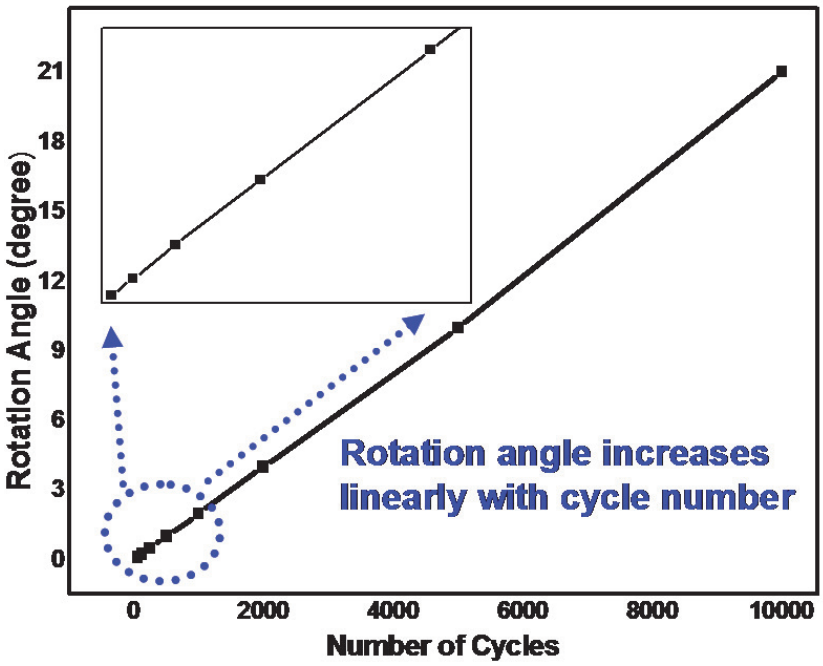

Figure 6.10: Rotation angle of the motor actuated by 3.78MHz sinusoidal signal bursts with various number of sinusoidal cycles. Rotation accuracy of 0.1 degree is achieved

frequency of stator is determined by the radius of the stator and its equivalent Young's modulus. The resonant frequency of the (5, 1) mode for different size stators are different, as plotted in Figure 6.11. The resonant frequency increases from 3.78MHz for 820μm stator to 4.03MHz for 780μm stator, and 4.43MHz for 740μm stator. The size of the stator is designed that their resonant frequency will be close to the thickness mode resonance of the PZT plate. The performance of the motor will decrease if the resonance is too far away from 4.2MHz.

The subharmonic frequencies for stators with different sizes are shown in Figure 6.12. There is a constant frequency gap of 220kHz between the two subharmonic frequencies for all motors. Interferometer modal scan at the subharmonic frequencies does not show any resonant mode shape. If resonant modes do exist at subharmonic frequencies, the frequency gap between the two subharmonic frequencies is expected to increase as the diameter of the stator

decreases. Therefore, the subharmonic nonlinear frequencies could come from period-doubling bifurcations of the system with frequency splitting caused by the etch hole on the stator.

As stated in the last section, the rotation speed increases with excitation voltage at first due to the increase of rotational force on the rotor is greater than the increase of kinetic friction force. However, after the excitation voltage passes a certain point when the increase of friction force dominates, the rotation speed starts to decrease with excitation voltage Figure 6.13. Motor with 820μm stator has a low threshold voltage of 3.5V, but its rotation speed start to decrease after 5.5V with maximum speed of 180rpm. For motor with 780μm stator, the maximum speed is 290 rpm at 9V. Although the 740μm stator motor has a high threshold voltage of 8.5, its maximum rotation speed is over 320 rpm because small stator generates small friction force on rotor even at high excitation voltages. As the rotor size increases, the increase in viscous damping between rotor and hub is likely reason for lower amplitude at larger diameters, and the onset of nonlinear acoustic streaming forces.

6.8 Rotor with integrated mirrors

As show in Figure 6.14, a micromotor with reflectors integrated on its rotor is fabricated and tested. The thickness and diameter of the stator and rotor are 2.25μm, 585μm and 2.5μm, 980μm respectively with the reflector dimension of 150μm long, 75μm wide, and 2μm thick. The device is released and excited with the same setup as mentioned in the previous sections. The stator of the rotating stage is designed to be small to accommodate the reflectors. However, the significant reduction of the stator size causes its (5, 1) mode resonant frequency to be at least double the frequency of 820 μm stator, estimated from Equation 6.1. Therefore,

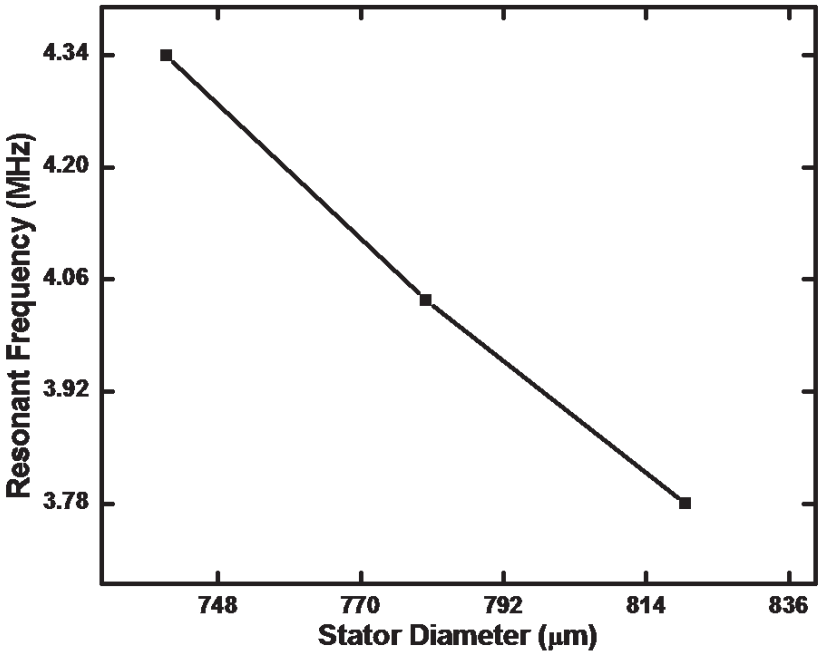

Figure 6.11: (5, 1) mode resonant frequencies for motors with different stator sizes

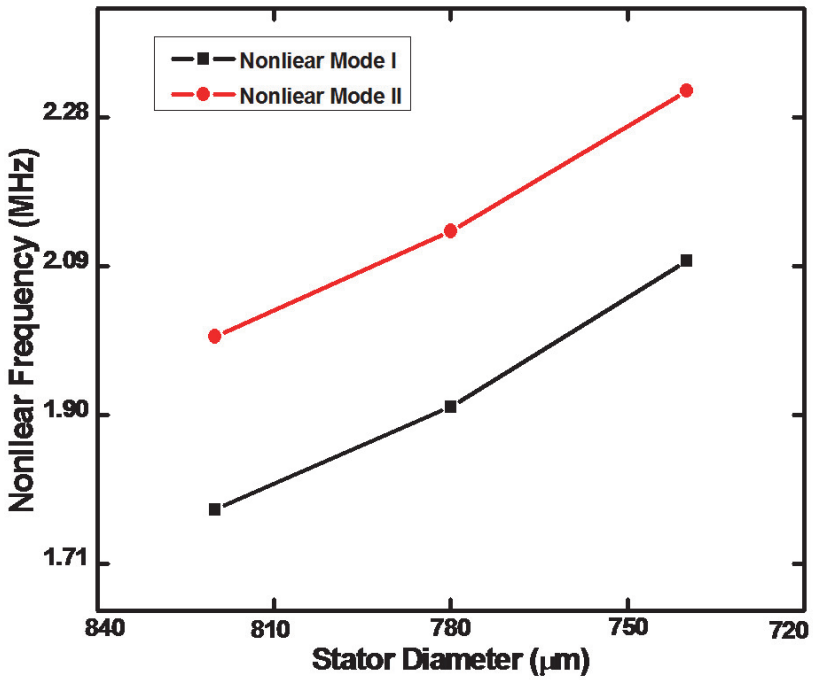

Figure 6.12: Subharmonic frequencies of the motors with different stator diameters

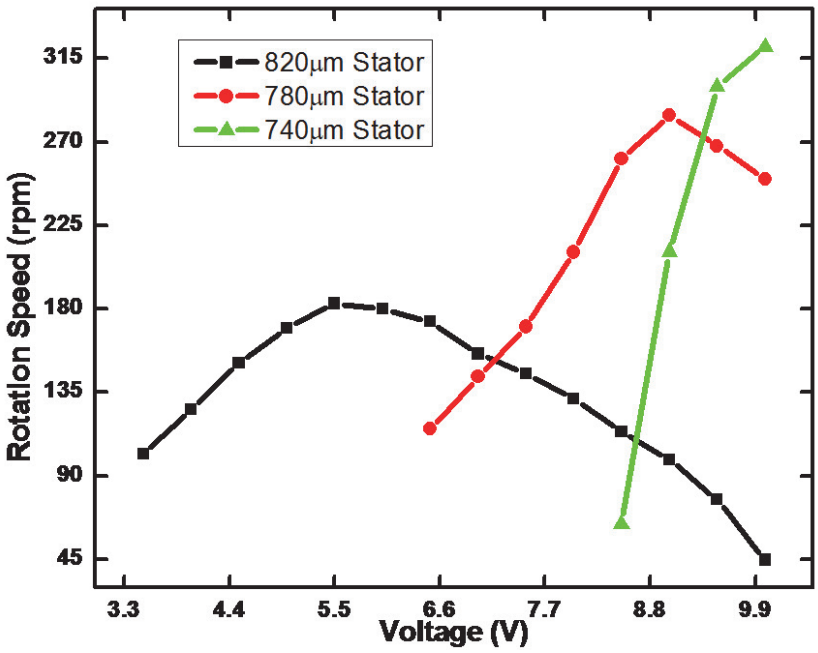

Figure 6.13: Measured rotation speed vs. excitation voltage for motors with varies stator sizes

the (5,1) mode resonant frequency of the stator is far away from the thickness mode frequency of the PZT plate, which makes the coupling between the stator and the rotor too weak to generate any motion on the rotor.

Actuated at 600kHz with a voltage of 10V, rotation of the rotor is observed. The rotation speed is 80rpm, which is much less efficient than actuated around the PZT thickness mode. The mode shape of the stator at 600KHz is shown in Figure 6.15. At 600kHz, the stator has the maximum vibration amplitude, which generates motor rotation. For future rotation stage design, the resonant frequency of the stator will be set around 4.2MHz to achieve optimal performance.

6.9 Conclusion

In this chapter, with optical and laser interferometer measurements, the nonlinear subharmonic vibrations of the stator is measured to gain better understanding

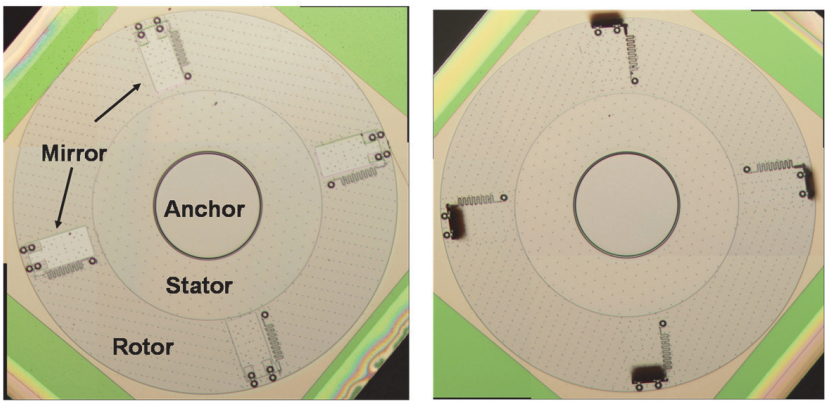

Figure 6.14: Optical image of a micro-ultrasonic motor integrated with reflective mirrors on the rotor, (a) mirrors down, (b) mirrors up and locked in place

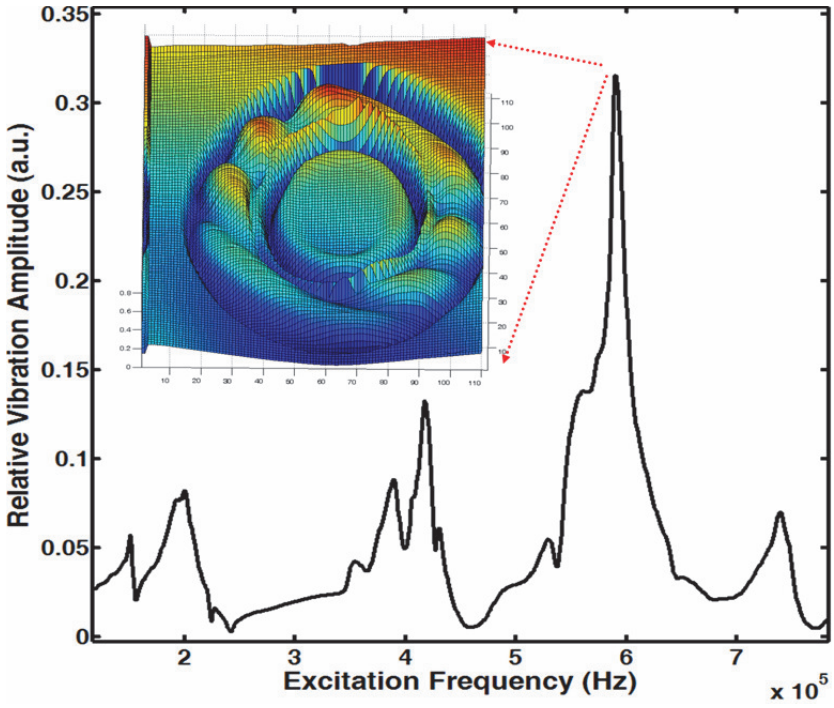

Figure 6.15: The vibration amplitude of the 585μm stator driven at different frequencies, and the modal shape of the stator driven around 600kHz while the motor is rotating

of the motor's operation principle. With 3.78MHz actuation frequency, the subharmonic mode at 1.78MHz is (1, 13) traveling mode obtained from optical transient measurement, while the subhormonic mode at 2.0MHz is (0, 20) standing mode measured with laser interferometer 2D scan. The performances of the micromotors with different sized stator are studied to optimize the motor design. The rotational threshold and maximum rotation speed of the motor varies with the size of the stator. While large stator (820μm) has lower rotation threshold (3.5V,) its maximum rotation speed (180rpm) is significantly lower than smaller stator (740μm), whose maximum rotation speed is over 320 rpm with rotation threshold of 8.5V. In future modeling and measurement of damping forces will help in identifying the motor design space.With its operation principle experimentally studied and demonstrated, the motor operation can be optimized and integrated to implement closed-loop control of motor position by optical feedback, or other integrated capacitive electrodes around the rotor. To realize compact rotating platform carrying stages for micro-optics and other sensing applications. Micro-sensors, micro-mirrors and other micro components need to be integrated with the rotor (Figure 6.1). Future study will be focus on the integration of the rotating stage based on the ultrasonic micrometer.

CHAPTER 7

CARBON MATERIALS STUDY FOR MEMS APPLICATIONS

7.1 Thin-Films of C60

We report on the first-ever pristine C60 (Fullerene) surface micromachined structures fabricated using an all-dry etch process. These structures are used to measure the C60 thin film MEMS electromechanical properties. These properties indicate that C60 is promising for realizing useful boundary conditions for MEMS resonators, and stiction properties for MEMS and NEMS switch applications. The clamped-clamped and clamped-free beams are fabricated with XeF^2 silicon-etch process, with negligible damage to the fullerene films ensuring that predictable C60 material properties can be realized in MEMS. Under substrate-attached-PZT excitation, the resonance responses of the cantilevers and beams are measured with a laser interferometer. The elastic properties of the C60 film are thus obtained from the measured resonance frequencies.

7.1.1 Introduction

C60 molecules are held together by van der Waals forces, as opposed to covalent and metallic bonds found in most other MEMS thin-film-materials. Van der Waals force is relatively weak compared to normal chemical bonds, which leads to lower elastic Young's modulus for C60 solid. The perfect spherical shape of C60 molecules further reduces the inter-molecular forces. The van der Waals like force can be expressed more accurately by the Girifalco potential [55] in the form of

$$\Phi(r) = -\alpha[\frac{1}{s(s-1)^3} + \frac{1}{s(s+1)^3} - \frac{2}{s^4}] + \beta[\frac{1}{s(s-1)^9} + \frac{1}{s(s+1)^9} - \frac{2}{s^{10}}] \quad (7.1)$$

Table 7.1: Constants for Physical Interactions between C60 Molecules

A=32.00×10^{-60}erg.cm^6	β=35.95×10^{-18}erg
B=55.77×10^{-105}erg.cm^{12}	R_0=1.006nm
X_0=0.3895nm	2a=0.71nm
α=32.00×10^{-60}erg	R_m=1.005nm

where

$$S = \frac{r}{2a} \tag{7.2}$$

$$\alpha = \frac{N^2 A}{12(2a)^6} \tag{7.3}$$

$$\beta = \frac{N^2 B}{90(2a)^{12}} \tag{7.4}$$

N is the number of atoms on each sphere, i.e. N=60. Also, constants for physical interactions between C60 molecules are listed in Table 7.1 [55]. With this inter-molecular potential, the layering of the different C60 molecules onto an anisotropic material such as silicon has been modeled by geometric arguments.

As the number of C60 layers increases, the interatomic distances become that of regular C60 solid. The bond energies are in the 0.3eV range between C60 molecules and 0.08eV between silicon and C60 molecules. Therefore the C60-silicon bond energy is a rather small around 4kBT, predicting a weak bond. This property leads to very low interaction energy, and might result in very low stiction forces between silicon and fullerene films. The weak molecular bond also results in high acoustic and ultrasonic internal loss due to C60-C60 slip motion. This high damping can be used to realize high-loss boundary-conditions for electromechanical resonant structures, without any out-gassing associated with polymeric films. C60 films also have very low density and Young's modulus for low acoustic-impedance

Table 7.2: Young's modulus and acoustic impedance of typical MEMS materials

Material	Youngs Modulus (GPa)	Acoustic Impedance (MRayl)
C^60(Here)	9.47	3.58
Polysilicon	169	19.85
Aluminum	70	13.75
Gold	78	38.80
SiO_2	70	12.41
Si_3N_4	290	31.58
Tungsten	411	88.95

(Table 7.2. This property can be useful to provide high-impedance mismatch between resonators, without out gassing associated with polymeric materials with similar acoustic impedances. The C60 electrical insulating property, combined with its high internal loss and low-impedance, would enable coupled resonator arrays, where mechanical coupling needs to be spatially modulated by large ratios, without using free-space between resonators. Additionally, C60 has ultra low surface energy and friction [56], which can be utilized for stiction prevention, and precursors for on-chip carbon nanotube fabrication [57].

Since C60 first captured the imagination of the science and technology community [58], its bulk single-crystal properties have been extensively studied [59] [60]. However, no micron-size free standing structure has been reported. Macro-size C60 membranes were fabricated [61], but CF_4 silicon etching used was identified as disruptive to C60 structure. With XeF_2 silicon etching used in our process, no damage to C60 film was observed. Moreover, we present the resonant properties of isolated C60 surface-micromachined MEMS.

7.1.2 Device Fabrication

In our experiments, 99.5% pure C60 powder from SES Research is evaporated onto patterned silicon wafer in a thermal evaporator. C60 cantilevers are fabricated with

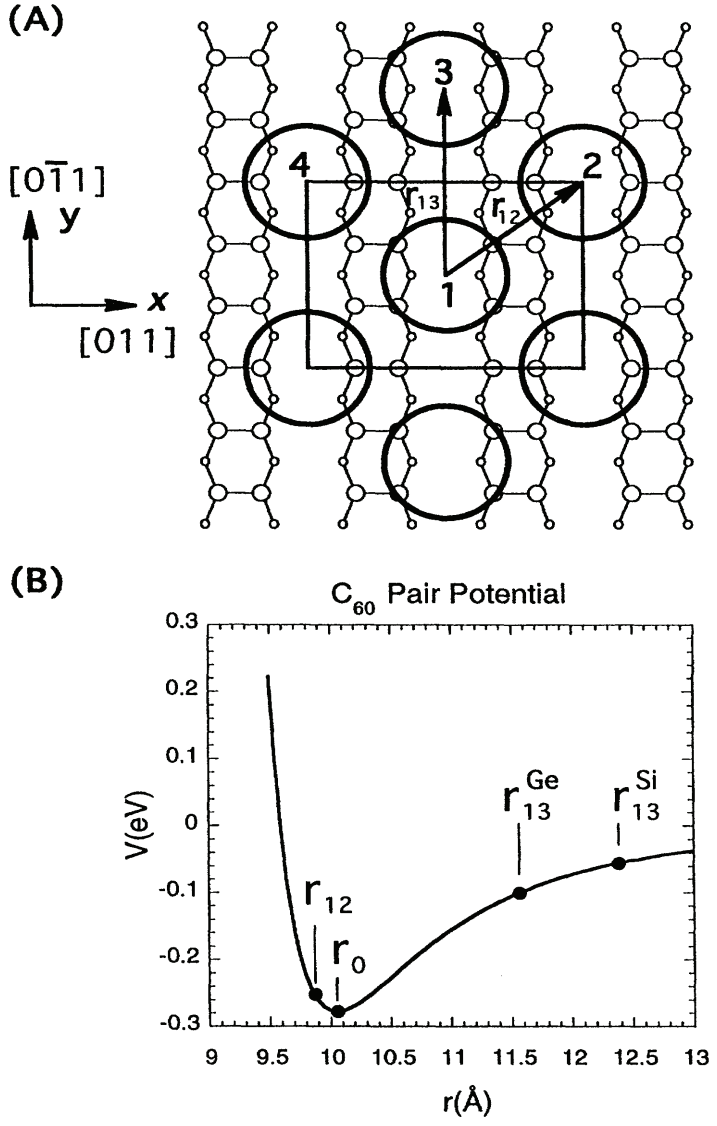

Figure 7.1: This figure shows the ordering of C60 molecules onto silicon and germanium [62]

a one-mask process (Figure 7.2). To ensure a stable anchor after the undercut release process, cantilever anchors are design to be much larger than the beam width. Silicon wafer is first patterned and then etched using DRIE process (3μm deep) to form mesas in the shape of the desired C60 microstructures. A 400 nm-thick C60 film is deposited via sublimation at 350^{o}C onto the silicon wafer at a rate of 20nm/minute (or 20ML/min). The built-in stress of the C60 film is measured to be 14MPa tensile, (measured with FleXus), which is low compared to other residual stresses, and might be due to the initial lattice mismatch between C60 and silicon as predicted by Figure 7.1(b). To release the C60 cantilevers, different wet and dry etching processes are investigated. C60 films are found to be either soluble or washed away in solvents and acids such as acetone, methanol, and HF. Furthermore, dry RIE processes with chemicals such as CF_4 and SF_6 are found to attack C60 films. Because of the high selectivity of XeF_2 to silicon, we tried XeF_2 dry etching of the silicon C60 combination. Raman spectrum (measured with Nanonics MV1000) of the C60 film are measured before and and after the XeF_2 etch to see effect on film properties. Both $A_g(1)$ mode and $A_g(2)$ modes are detected at 496 cm-1 and 1469 cm-1 respectively, which indicates the existence of pristine C60 [63]. Focusing on the $A_g(2)$ mode, Raman spectra of the C60 cantilevers are measured both before and after the XeF_2 etch (3 minutes,) and it shows no change in the carbon peak (Figure 7.3. Therefore, there is no structure damage caused by the XeF_2 release process. The SEM images of the C60 cantilevers are taken with electron energy of 1-keV (Figure 7.1(b).) When the electron energy exceeds 1.4-keV, the cantilevers are charged and are easily shattered into pieces. This might be occurring due to local heating induced thermal expansion, or charging related strain induced in the structures.

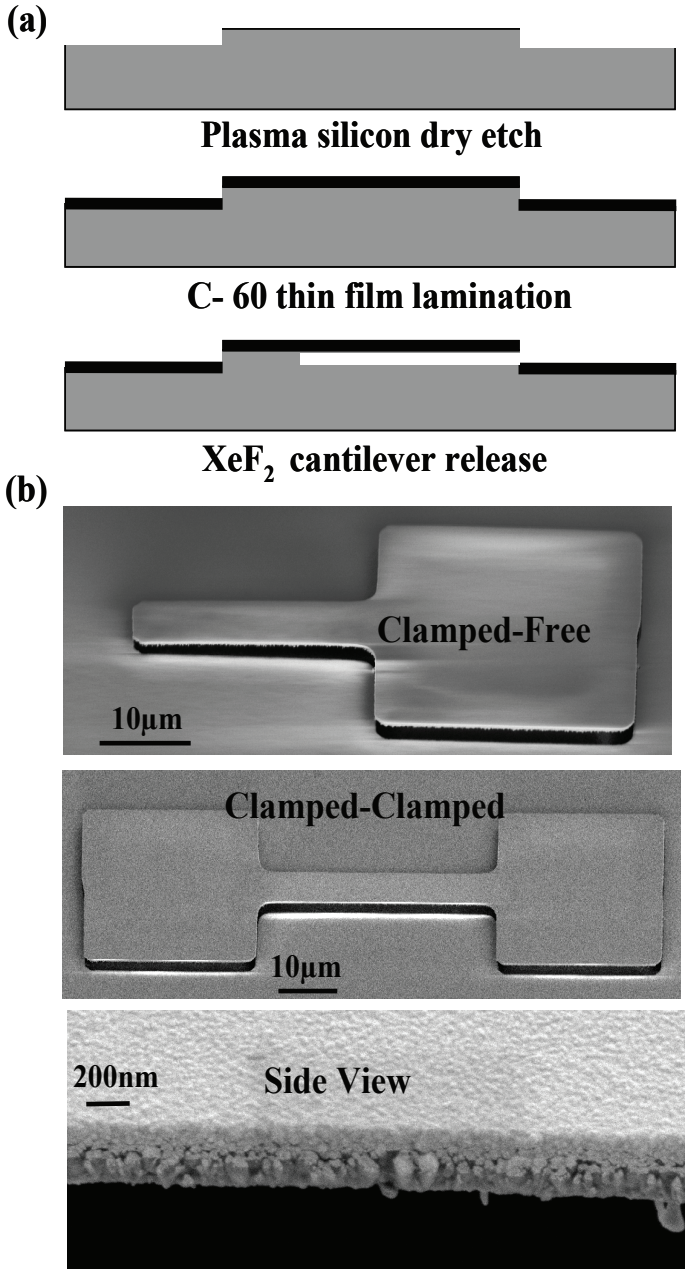

Figure 7.2: (a) Fabrication process (b) SEM images of the C60 clamped-clamped and clamped-free beams

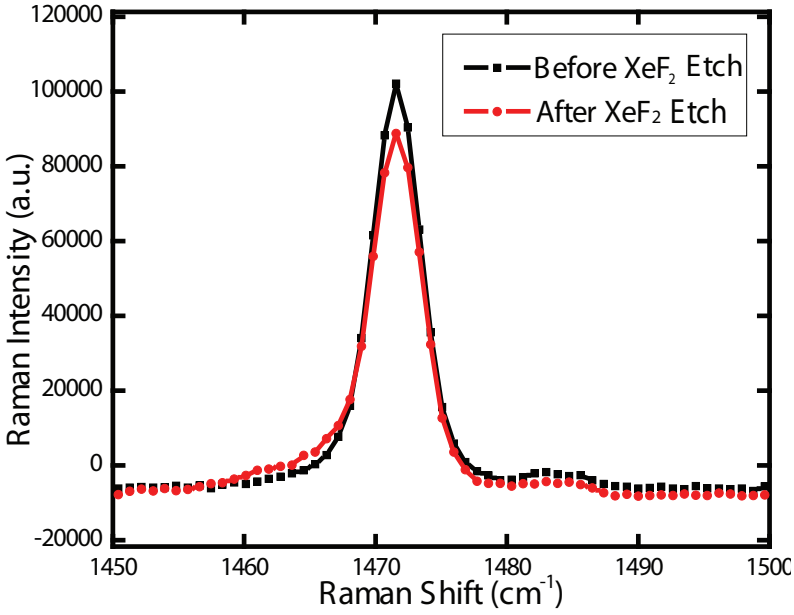

Figure 7.3: Raman spectra of the C60 microstructure measured using Nanonics MV1000

7.1.3 Experiment setup and results

To measure the mechanical resonance response of the cantilevers, a rectangular PZT-4H plate is adhesively bonded to the back of the silicon die, similar to techniques used in [64] . With the PZT plate excited with a low-voltage sinusoidal signal, the motion induced in the C60 structure by the PZT induced body motion was measured using an optical interferometer (Figure 7.4). The mode shape of the cantilever resonances at various frequencies can be obtained with a 2D displacement scan over the cantilever. With a 2-Vpp sinusoid applied to the PZT plate, the vibrations of a 22μm-long, 400nm-thick cantilever are measured using laser interferometer (PolytecTM OFV511), and a maximum motion amplitude of 50nm was obtained. A displacement scan shows a 3rd overtone mode is excited on the cantilever. The combined resonances of the PZT/Si/C60 composite are complicated by the various properties of the PZT plate, adhesion layer, silicon die,

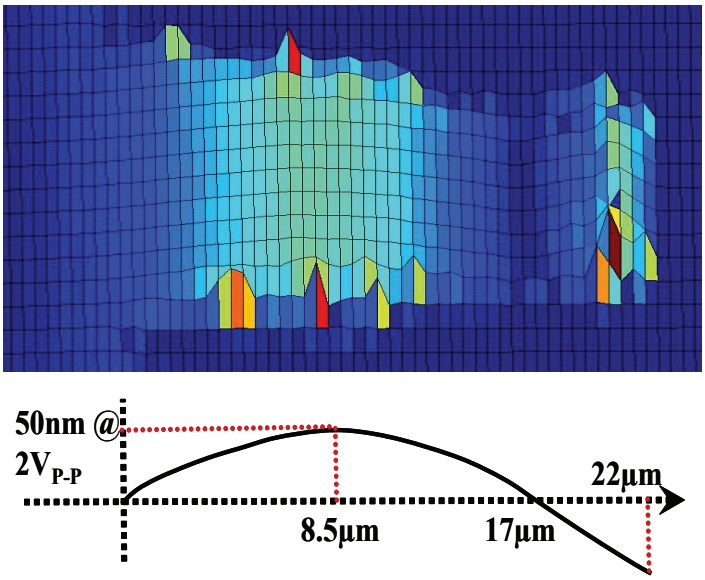

Figure 7.4: Optically scanned3rd overtone mode shape, and the side view sketch of the C60 clamped-free cantilever motion

and C60 structures. Therefore, to isolate C60 cantilever resonances, the signals both from the substrate and the cantilever need to be measured. Cantilever-only resonances can then be found by comparing the two signals.

For a C60 cantilever with length, width, and thickness equal to 30μm, 5μm, and 400nm respectively, the displacement of the beam is measured with the laser interferometer at its tip, while the PZT excitation frequency is varied from 1 KHz to 1.3 MHz with amplitude of 2Vp-p. The frequency spectra from the beam and substrate are both plotted in Figure 7.5. At low excitation frequencies, the fundamental mode of the C60 beam was too close to the thickness modes of the PZT. With lower quality factor while excited in air, it is difficult to distinguish the fundamental mode of the beam from the substrate vibrations. However, the 3rd overtone mode of the C60 cantilever (one displacement node) was identified not to be coupled with bulk modes, so they can be easily identified. As shown in Figure 5, at 1.12MHz, the beam displacement scan shows a resonant peak while the substrate displacement scan results in very little motion, which indicates

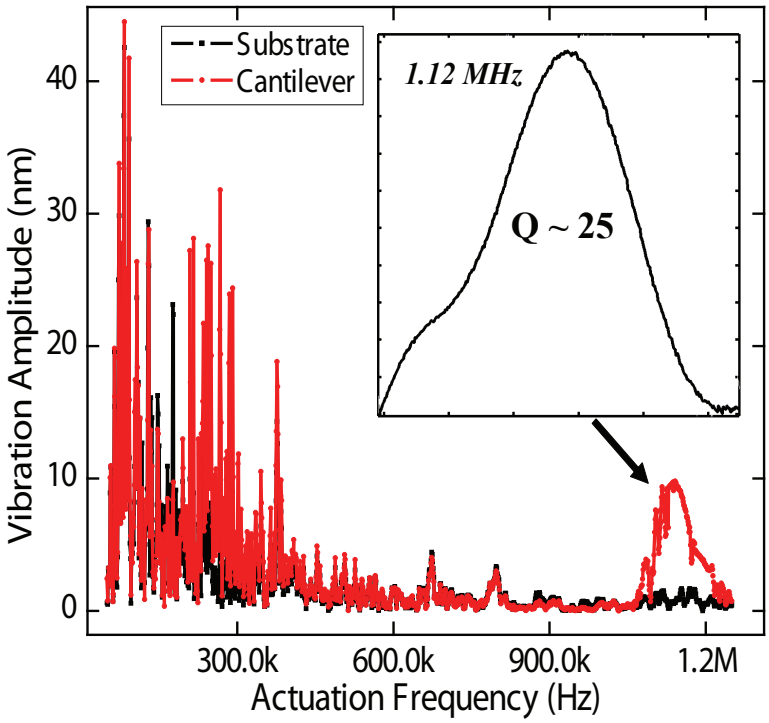

Figure 7.5: Mechanical motion spectra of the C60 cantilever (L=30m), and the substrate near it. Inset shows the expanded 3rd overtone mode with resonance frequency 1.12MHz, where the substrate motion is negligible

that the 1.12MHz resonance is a pure C60 beam resonance. Further 2D scan of the cantilever at 1.12MHz verifies the existence of the 3rd overtone mode. The 3rd overtone resonance has a quality factor of 25 when tested in air. This Q is reasonable as the room-temperature single-crystal C60 Q is around 200 [59]. In the cantilever vibration process, the distance between C60 molecules changes, which could lead to significant spring softening of the structure and loss due to C60-C60 slip motion. However, further analysis with testing in vacuum is needed to identify the loss mechanisms.

To obtain the Young's modulus of the thin film, the 3rd overtone mode resonant frequencies for C60 cantilevers with different lengths are measured with the interferometer. Due to the isotropic XeF_2 release process, there is a 3μm anchor undercut. For the first order approximation, the undercut length is considered as

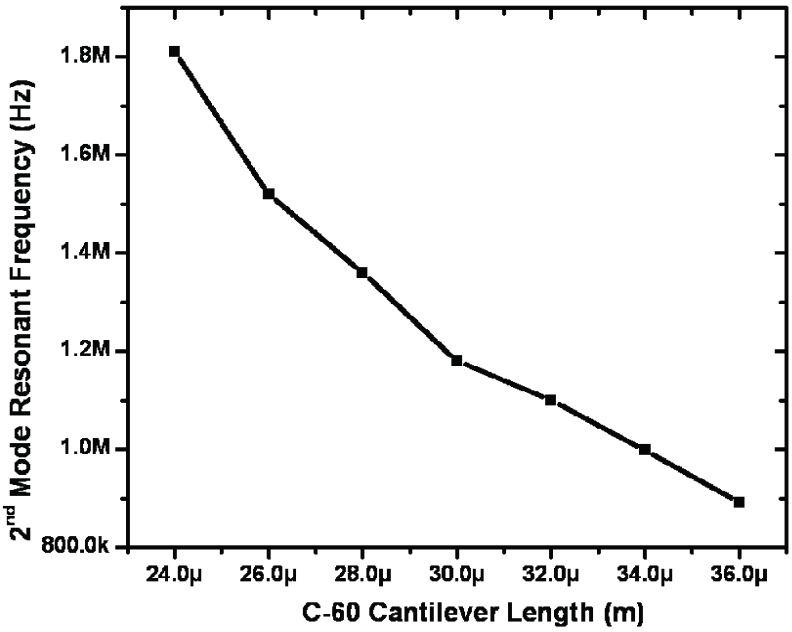

Figure 7.6: Experimentally measured C-60 cantilever3rd overtone mode resonant frequencies with different length

extra beam length added to the designed beam length in the calculation. As show in Figure 7.6, the resonant frequency varies from 1.8MHz for 24μm long beam to 900-kHz for 36um long beam. The resonant frequency of a clamped-free cantilever at this mode can be expressed as [65]:

$$f = 1.01\frac{t}{L^2}\sqrt{\frac{E}{\rho}} \tag{7.5}$$

where t and L are the thickness and length of the beam, E, and are the Young's modulus and density of the film. The resonant frequencies are then plotted as a function of 1/L2, resulting a straight line with slope of 1.07e^{-3} m^2/s (7.7) With film thickness and density measured to be 400nm and 1350 Kg/m^3 respectively, the Young's modulus of the C60 microstructure is 9.47 +/- 0.3GPa, comparable to values reported to bulk [57] [58]. The resulting acoustic impedance $\sqrt{\frac{1}{E\rho}}$ is 3.58 MRayl much lower than other materials used in MEMS, enabling the films to be used in acoustic band gap designs.

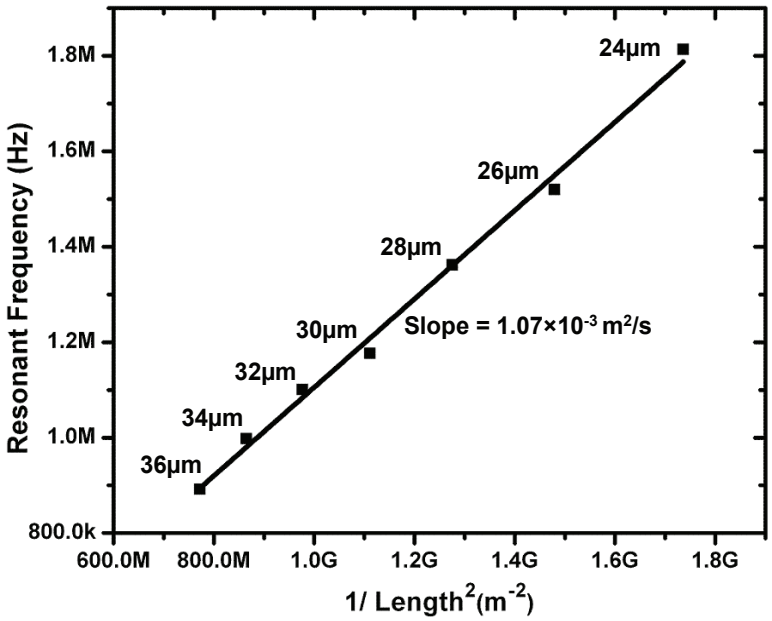

Figure 7.7: Experimentally measured C60 cantilever second-mode resonant frequencies as a function of (1/beam length)^2

7.1.4 Conclusion

In this chapter, we report an all-dry XeF_2 silicon-etch process for C60 (Fullerene) surface micromachining, which maintains the chemical structure of pristine fullerene films. With this process, micron-scale C60 cantilevers are surface-micromachined fabricated for the first time. The resonant and mechanical properties of the MEMS cantilevers are measured, and the C60 film has a Young's modulus of 9.47 +/- 0.3GPa, with low acoustic impedance of 3.58 MRayl.

7.2 Photoresist-Pyrolyzed Carbon Film

Electrical and mechanical properties of photoresist-pyrolyzed carbon film are studied for RF MEMS applications. Carbon film, which is from photoresist pyrolyzation in forming gas at temperatures ranging from 500_oC to 900_oC, is investigated for their properties including thickness, resistivity, Raman spectrum,

stress, and Young's modulus. Free-standing carbon MEMS cantilevers and carbon MEMS RF switches are fabricated, with their resonant frequencies measured using interferometer with PZT actuation. Young's modulus of 13.8GPa is measured from film pyrolyzed at 800oC. Electrochemical properties carbon MEMS structures has been previous reported for applications such as, miniature battery [66], and biological sensors[67]. In this abstract, we focus on the application of pyrolyed carbon film as a new material for RF MEMS with the potential of low pull-down voltage and low stiction, while it has been reported that carbon film has low friction, low wear coefficient, and high contact angle of water[68].

7.2.1 Introduction

Among various methods of depositing carbon film, photoresist pyrolyzation is very attractive because photoresist is CMOS compatible and its patterns can be finely defined using lithography technologies.

7.2.2 Properties of pyrolyzed carbon thin films

In our study, Shipley 1827 photoresist is used instead of thicker AZ4330 or SU-8 used for electrochemical applications. Photoresist, spin-coated on top of silicon wafer with oxide isolation, are pyrolyzed at 400, 500, 700, 800, and 900^{o}C in forming gas. The shrinkage of film at different temperatures is plotted in Figure 7.8. While 60% of original thickness is left if pyrolyzed at 400^{o}C, only 23% is left at 900^{o}C.

Raman spectra are then taken to verify the existence of carbon crystal in different films. No Raman spectra were obtained for films pyrolyzed at 400^{o}C and 500^{o}C degree because they are fluorescent. The data from films pyrolyzed at 700^{o}C, 800^{o}C, and 900^{o}C shows two peaks at approximately 1360cm^{-1} and

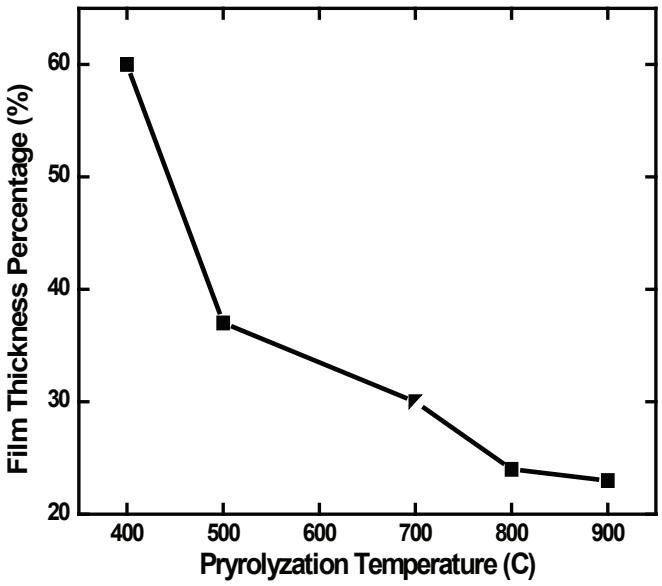

Figure 7.8: Measurement of residue film thickness percentage at different pyrolyzation temperatures

1600cm^{-1} (Figure 7.9), which represent "D" and "E_{2g}" bands respectively [69]. The intensity ratio (D/E_{2g} ratio) has been correlated with disorder of the sp^2 carbon matrix. The ratio increases with pyrolyzation temperature indicates that the carbon crystal size decreases with increasing temperature.

Measured with 4-point probe, the sheet resistance of the film decreases dramatically with increasing the temperature (Figure 7.10), while their values agree with what have been previously reported with SU-8 [70].

Film stress, which is critical for RF MEMS applications, is measured and plotted in Figure 7.11. At low temperatures, the film stress and compressive, and it becomes tensile as temperature increases.

7.2.3 Experiment setup and results

To investigate the Young's modulus of the film, carbon MEMS cantilevers are fabricated with a simple one-mask process at pyrolyzation temperature of 800^{o}C

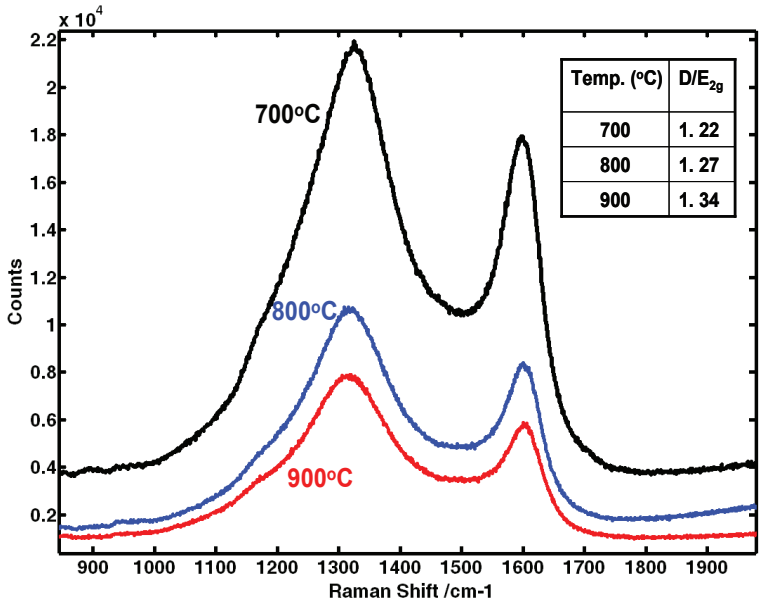

Figure 7.9: Raman spectra of the pyrolyzed carbon film at different pyrolysis temperatures

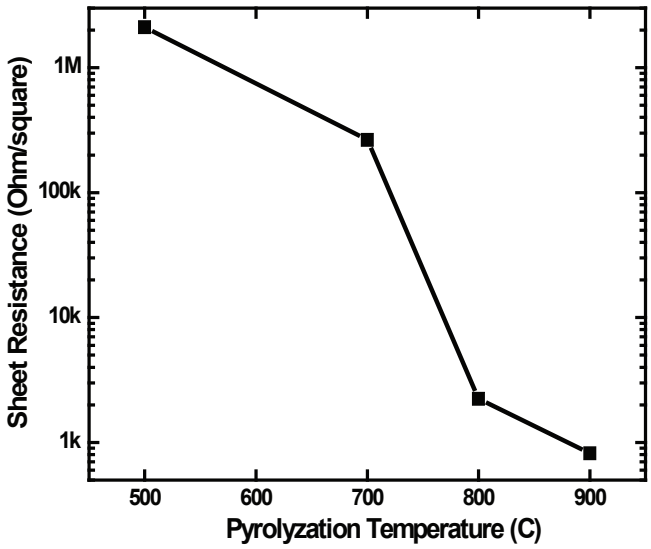

Figure 7.10: Measured carbon film sheet resistance as a function of pyrolysis temperature

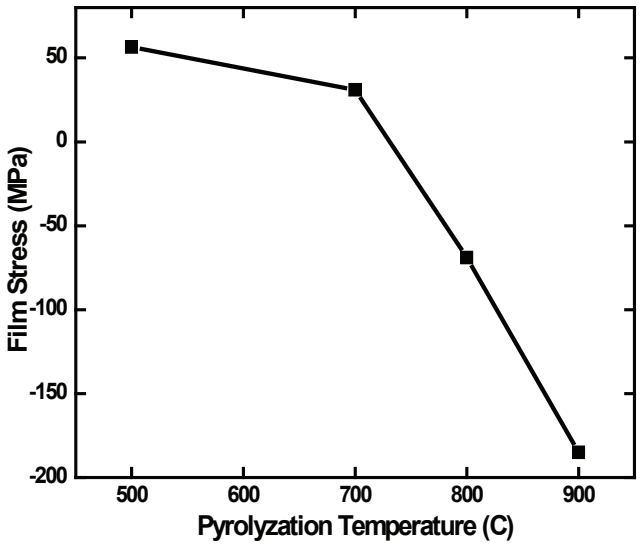

Figure 7.11: Measured carbon stress as a function of pyrolysis temperature

(film with low stress.) Cantilevers, patterned with photoresist on top of a bare silicon wafer, are pyrolyzed, and then released with XeF_2 vapor silicon etch. First-mode resonant frequencies of cantilevers with different lengths are measured with interferometer with PZT actuation on the wafer substrate (Figure 7.12). For clamped-free cantilevers, the first mode resonant frequency can be expressed by

$$f = 0.162 \frac{t}{L^2} \sqrt{\frac{E}{\rho}} \tag{7.6}$$

where t and L are the thickness and length of the cantilevers respectively, E and ρ are the young's modulus and density of the film. With film thickness and density of the film measured to be 810nm and 1528 Kg/m^3 respectively, the Young's modulus of the carbon film pyrolyzed at 800^oC is calculated to be 13.8GPa.

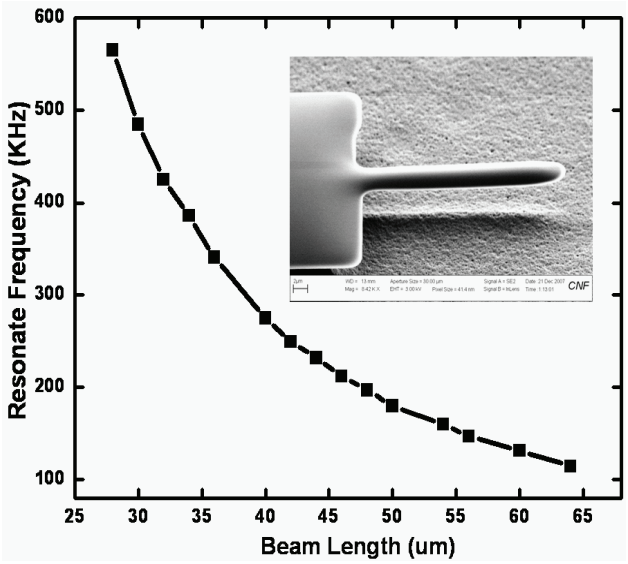

Figure 7.12: SEM image and measured cantilever resonant frequency as a function of length

APPENDIX A

RADIOACTIVE TRUE RANDOM NUMBER GENERATOR WITH UNIFORMLY DISTRIBUTED INTEGER OUTPUT

True randomness and uniformity in generated numbers are achieved in the prototype device, with a output data rate of 6 Kbit/second. The output bit-rate can be dramatically increased by increasing the radioactivity. With a radioactive electron output of 5 million electrons per second, which only equals to a radioactivity of 140 micro-curies, a 4-bit TRNG can provide an output rate of 20 Mbit per second. It is much higher than the latest results reported using other techniques [71], [72], [73]. Low energy radioactive isotopes such as Americium-241 and Promethium-147 have been safely used inside smoke detector and pace-maker respectively since 1970s. Radiation from Nickel-63 has even much less energy than the two isotopes mentioned above. It is perfectly safe to used it to generate TRNs.

We have demonstrated a proof-of-concept of utilizing properties of a Poisson process to generate a radioactive-decay-based TRNG that generates multiple bits per decay event. With high-frequency clocks and counters, hight output bit rate can be achieved by increasing the radioactivity of nickel-63. Since only solid-state electron detector and digital circuit are used in our design, the TRNG can be fabricated on a single chip with nickel-63 radioactive film electrodelessly plated on top of the detector. The TRNG can, therefore, be integrated into mobile device to provide high quality reliable TRNs even when working in harsh environments. Will be added later.

A.1 Introduction

From numerical simulation to data cryptography, random numbers are becoming essential in many applications. While for many of those applications, software-

generated pseudorandom numbers are efficiency enough, applications like data cryptography requires high quality true random numbers (TRNs), which cannot be predicted. True random number generators (TRNGs) are based on physical random processes which result in indeterminate sequence of random numbers. To generate TRNs, different kinds of random noises, such as, thermal noise [74], shot noise [75], and jitter in free running oscillators [76], have been used. However, the performances of those TRNGs are all affected by their working conditions (temperature, noise from power supply, etc). On the other hand, radioactive decay process consumes zero power, and it is independent of outside environment under normal operating conditions [77]. The radioactive decay process is a Poisson process, which has been experimentally verified in many previous works [78], [79]. and [80]. As a memory-less random process, radioactive decay has been previously reported to generate TRNs [81], [82], and [83]. In [81], random numbers are generated by counting the number of decays in a fixed time period. For every random bit, more than 10 decays are needed. By comparing two adjacent interarrival times (the time between two radioactive decays), Figotin,et al. improved the generation efficiency to one random bit every 2 decays [82]. In [83], Alkassar emphet al. improved the efficiency future by using a high frequency clock as reference to measure the interarrival time, and one random bit per decay was reported in their work. In this work, we present a TRNG that fully utilizes the properties of Poisson processes, and as a result, enables multiple random bits output per radioactive decay event.

Probability distributions can be readily transformed into other distributions. However the most readily useful distribution is the uniform distribution of random numbers. We therefore exploit the Poisson properties of the radioactive process to generate uniform random numbers.

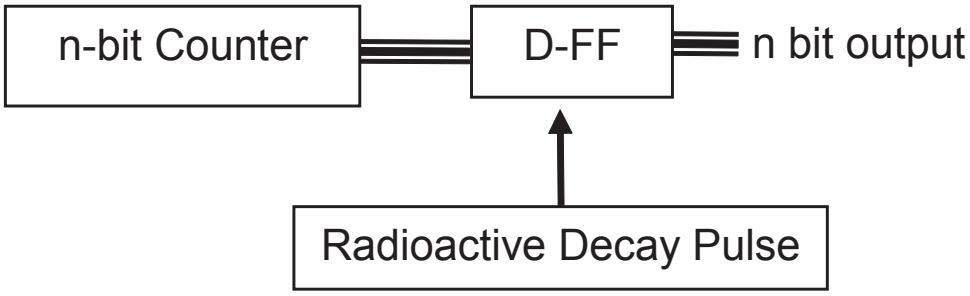

Figure A.1: Illustration figure.

A.2 Uniformly distributed random numbers from a Poisson Process

To design a TRNG with high output rate, the properties of radioactive decay are first explored. As a memory-less Poisson process, the inter-arrival time between two consecutive radioactive decay events is exponentially distributed. Poisson process for radioactive decay is also a discrete-time Markov process, where the future development of the Markov Chain depends only on its present state, not on the sequence of previous states. The one-step transition probability from state i to state j is given by

$$P_{ij} = P(X_1 = j | X_0 = i). \tag{A.1}$$

For illustration, let us consider the system shown in figure A.1. An n-bit counter is counting continuously from 0 to $2^n - 1$ with a time period Δt. The counter output latched using a bank of 3 D-latches, and the latch-enable is provided by the pulse signal from a radioactive source. When a radioactive decay occurs, the pulse signal enables the bank of D-latches that latch the current state of the counter. Since

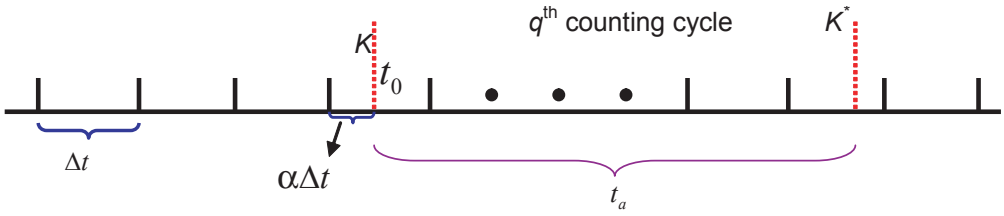

Figure A.2: Arrival time illustration.

the pulse input from radioactive decay is truly random, the n-bit output from the latches is also random with its distribution properties further analyzed as below.

As shown in figure A.2, consider the general case when a decay event occurs at time t_0 with counter output K, and another decay event occurs q cycles later with counter output K^*. The time period between these two decays is t_a .The one-step transition probability from output K to K^* after time t_a is given by

$$P(X_1 = K^*|X = K) = \sum_{q=0}^{\infty} \int_{t_a^-}^{t_a^+} \lambda e^{-\lambda t} dt, \tag{A.2}$$

where t_a is defined as $t_a^- = 8q\Delta t + (K^* - K)\Delta t - \alpha\Delta t$ and $t_a^+ = 8q\Delta t + (K^* - K)\Delta t - \alpha\Delta t + \Delta t$, and $\alpha \in [0, 1]$. Therefore, the one-step transition probability can be calculated as

$$P_{KK^*} = \sum_{q=0}^{\infty} \int_{8q\Delta t+(K^*-K)\Delta t-\alpha\Delta t}^{8q\Delta t+(K^*-K)\Delta t-\alpha\Delta t+\Delta t} \lambda e^{-\lambda t} dt \tag{A.3}$$

$$= \sum_{q=0}^{\infty} e^{-\lambda[8q\Delta t+(K^*-K)\Delta t-\alpha\Delta t]} - e^{-\lambda[8q\Delta t+(K^*-K)\Delta t-\alpha\Delta t+\Delta t]} \tag{A.4}$$

$$= \sum_{q=0}^{\infty} e^{-\lambda[8q\Delta t+(K^*-K)\Delta t-\alpha\Delta t]}(1 - e^{-\lambda\Delta t}). \tag{A.5}$$

If $\frac{1}{\Delta t} \gg \lambda$, then $\alpha\Delta t$ can be ignored, and the system can be modeled as a homogeneous Markov chain with one-step transition probability given by

$$P_{KK^*} = \sum_{q=0}^{\infty} e^{-\lambda[8q\Delta t+(K^*-K)\Delta t]}(1-e^{-\lambda\Delta t}). \tag{A.6}$$

To verify the equation above, we let $k = 0$, then the sum the transition probabilities can be written as

$$\sum_{K^*}^{7} P_{0K^*} = \frac{(1-e^{-\lambda\Delta t})}{(1-e^{-\lambda\Delta t})} = 1. \tag{A.7}$$

For a finite Markov chain with n states, we can show from equation A.6 that

$$\begin{aligned} P_{00} = P_{11} = P_{22} = \ldots = P_{(n-1)(n-1)} &= p_0 \\ P_{01} = P_{12} = P_{23} = \ldots = P_{(n-1)1} &= p_1 \\ &\vdots \\ P_{0(n-1)} = P_{10} = P_{21} = \ldots = P_{(n-1)(n-2)} &= p_{(n-1)} \end{aligned}$$

Therefore, for this n-state Markov chain, the matrix of the one-step transition probabilities is given by

$$P = \begin{bmatrix} p_0 & p_1 & \cdots & p_{(n-2)} & p_{(n-1)} \\ p_{(n-1)} & p_0 & \cdots & p_{(n-3)} & p_{(n-2)} \\ \vdots & & \ldots & & \vdots \\ p_2 & p_3 & \cdots & p_{0)} & p_1 \\ p_1 & p_2 & \cdots & p_{(n-1)} & p_0 \end{bmatrix}. \tag{A.8}$$

Since all the transition probabilities in the matrix are positive, for this stochastic matrix, there is a stationary distribution π (a row vector), which satisfies the equation

$$\pi = \pi P \tag{A.9}$$

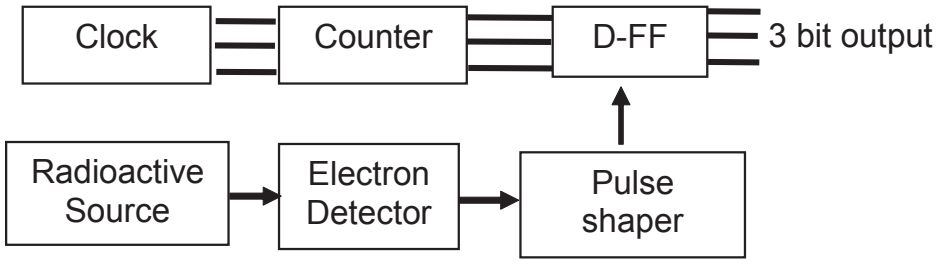

Figure A.3: Block diagram for uniform random number generator.

The Markov chain is also irreducible and aperiodic, so the distribution is unique. Assuming $\pi = \left[\frac{1}{n}, \frac{1}{n}, \frac{1}{n}, \ldots, \frac{1}{n}\right]$, it can be easily shown that $\pi = \pi P$. Therefore, the stationary distribution is uniform. Thus we have a uniform random number output.

A.3 Design and implementation of radioactive TRNG

To experimentally demonstrate the concept, a 3-bit TRNG with uniform integer output was built as shown in the block diagram shown in figure A.3. A clock is running at frequency of 10 MHz, with its output signal fed into a 3-bit counter. The operation principle is the same with the system shown in figure A.2. Radioactive decays are detected by an electron detector, which outputs a pulse that is shaped by a pulse-shaping circuit. The radioactive decay pulse signal from the pulse shaper is plotted in figure A.4(a). The inter-arrival time between pulses, as plotted in figure A.4(b), is exponentially distributed, which agrees with the distribution properties of Poisson process. This pulse is then used to enable the bank of D-Flipflops that latch the current state of the counter. In this implementation, the clock counter is sampled by the rising edge of the radioactive pulse output. In this experiment, the radioactive decay rate is about 2 kHz, which is much smaller than the 10 MHz

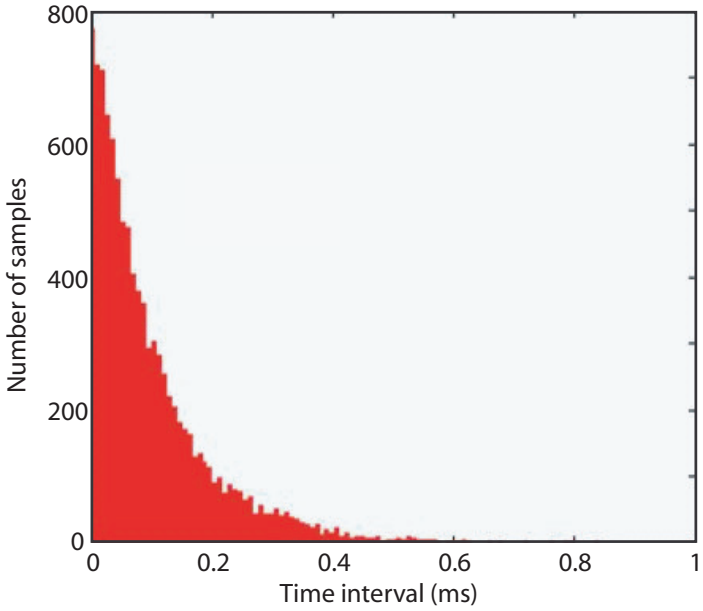

Figure A.4: (a) Radioactive decay pulse signal (b)Histogram of time intervals for 10000 samples for a radioactive source of average rate 27000 Hz .

counter speed.

The signals from the pulse shaper and *D*-flipflop are displayed on an oscilloscope as shown in figure A.5. The counter value is output every time a radioactive decay occurs.

A.4 Results and discussion

A.4.1 Uniformity test

One million random integers are generated by combining the data from all three bit lines. The results are plotted in figure A.6. Excellent uniformity among 8 digits are achieved by this system.

Great randomness and uniformity are achieved in the prototype device, with a output data rate of 6 Kbit/second. The output bit-rate can be dramatically

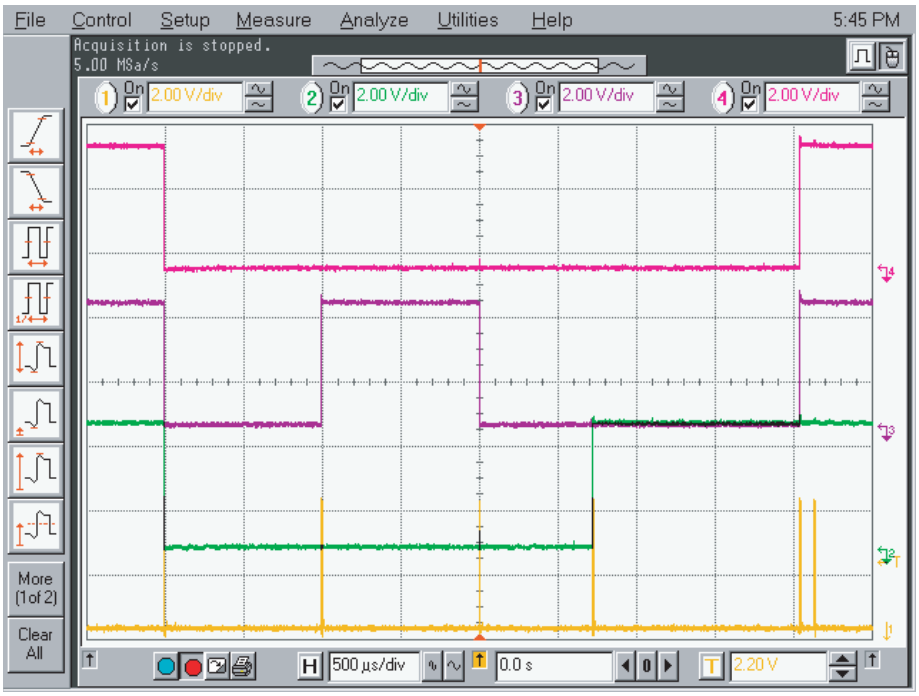

Figure A.5: Oscilloscope display of the random number system.

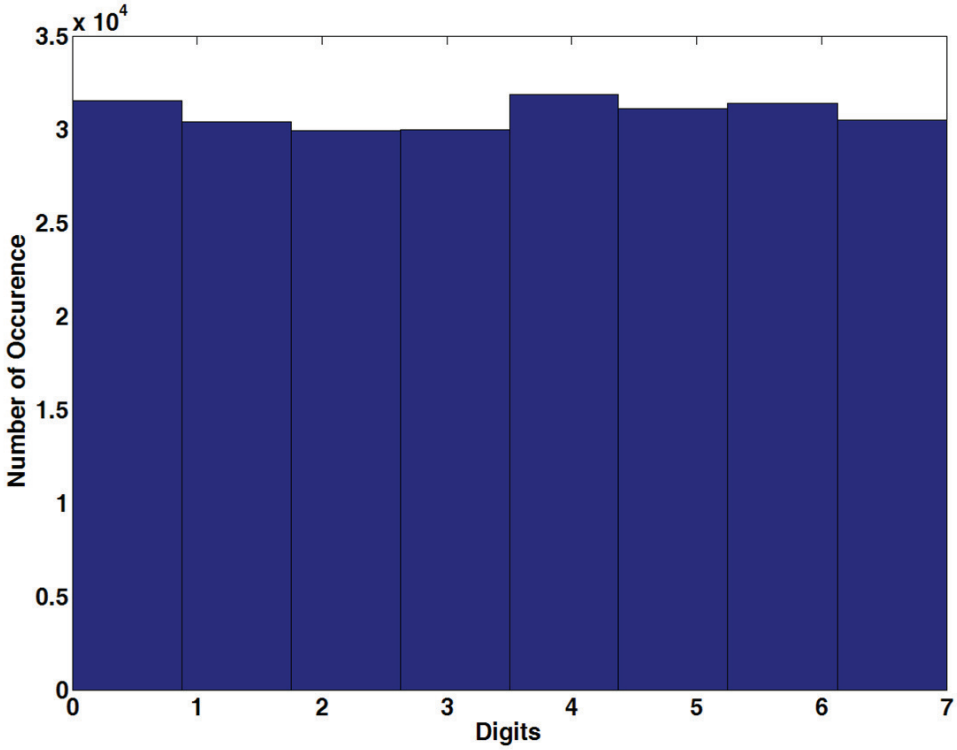

Figure A.6: Output of the uniform number generator.

increased by increasing the radioactivity. With a radioactive electron output of 5 million electrons per second, which only equals to a radioactivity of 140 micro-curies, a 4-bit TRNG can provide an output rate of 20 Mbit per second. It is much higher than the latest results reported using other techniques [71], [72], [73]. Low energy radioactive isotopes such as Americium-241 and Promethium-147 have been safely used inside smoke detector and pace-maker respectively since 1970s. Radiation from Nickel-63 has even much less energy than the two isotopes mentioned above. It is perfectly safe to used it to generate TRNs.

A.5 Conclusions

We have demonstrated a proof-of-concept of utilizing properties of a Poisson process to generate a radioactive-decay-based TRNG that generates multiple bits

per decay event. With high-frequency clocks and counters, hight output bit rate can be achieved by increasing the radioactivity of nickel-63. Since only solid-state electron detector and digital circuit are used in our design, the TRNG can be fabricated on a single chip with nickel-63 radioactive film electrodelessly plated on top of the detector. The TRNG can, therefore, be integrated into mobile device to provide high quality reliable TRNs even when working in harsh environments.

APPENDIX B

INTEGRATABLE ZERO-POWER VOLTAGE BIAS FOR SENSOR APPLICATIONS

A critical requirement for the success of autonomous remote systems is the realization of miniature power sources with long lifetimes, especially for the sensor networks working in harsh, inaccessible environments. While traditional power sources can only work up to several years without replacement or refueling, radioactive-powered DC bias source can work for 100 years with its performance unaffected by outside environment. Furthermore, together with other radioactive power generators we have been working on, a sensor network can be fully self-powered using radioactive source for hundreds of years.

B.1 Design and Analysis

Operating under vacuum, a radioactive DC bias has been previously demonstrated. However, the requirement of vacuum makes that system very difficult to be integrated with sensor chips. In this paper, we demonstrated a DC biasing that operates in air. As shown in figure B.1, the electrons from the nickel radioactive layer traveling through the oxide are collected on the bottom electrode, which leaves the top electrode positively charged, while the bottom electrode is negatively charged. A voltage bias is thus formed across the oxide capacitor.

The device can be electrically modeled with the circuit shown in figure B.2, where ideal current source I_{rad} is the radioactive current through the dielectric layer, C_{di} is the capacitance across the dielectric film, and R_{leak} is leakage resistance of the dielectric film. The maximum output voltage of the device is the voltage V_{out} across the ideal capacitor C_{di}. The output voltage reaches maximum when

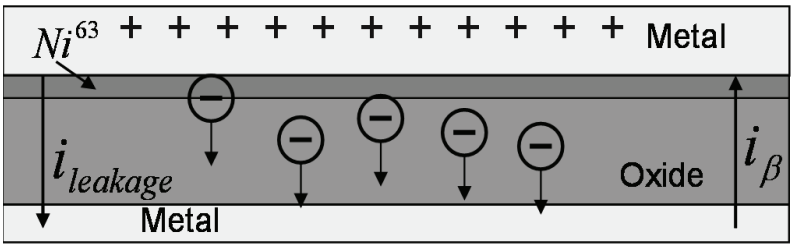

Figure B.1: Radioactive DC bias diagram

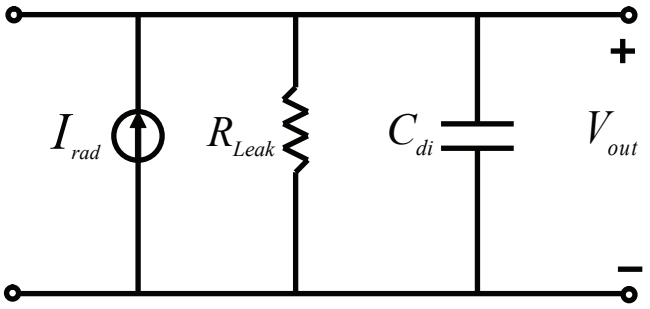

Figure B.2: Circuit model diagram

$$I_{rad} = \frac{V_{out}}{R_{leak}} \tag{B.1}$$

therefore,

$$V_{max} = I_{rad} R_{leak} \tag{B.2}$$

The radioactive current I_{rad} can be written as

$$I_{rad} = I_{rad} A \tag{B.3}$$

where J_{rad} is the radioactive current density, and A is the area of the device. The leakage resistance Rleak can also be expressed as

$$R_{leak} = \frac{\rho_{Al}}{A} \tag{B.4}$$

where ρ_{Al} is the unit-area resistivity. Therefore, equation B.2 can be rewritten as

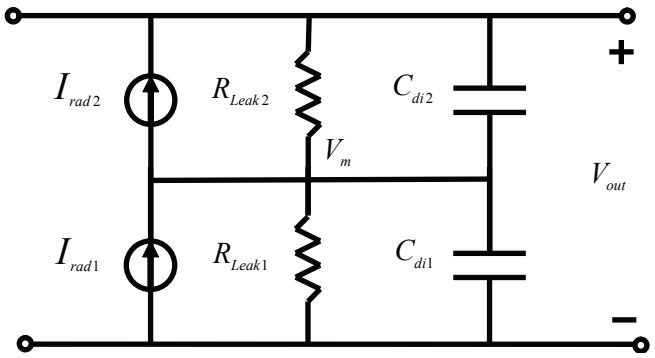

Figure B.3: Circuit model diagram for two RVBs connected in series

$$V_{max} = J_{rad}\rho_{Al} \tag{B.5}$$

Equation B.5shows that the output voltage is independent of device area. Therefore, this design can be miniaturized without compromising its performance, which makes it suitable to be integrated onto sensor chips.

The radioactive current I_{rad} is a function of radioactivity, dielectric property, and dielectric film thickness, while dielectric leakage resistance R_{leak} is a function of film property and film thickness. Since both radioactive current and leakage current are functions of film thickness, the maximum output voltage can be written as:

$$V_{max}(d) = I_{rad}(d)R_{leak}(d) \tag{B.6}$$

In equation B.6, the radioactive current through the dielectric decreases as the film thickness increase, while the leakage resistance increases with the film thickness. For given dielectric leakage properties and given amount of radioactivity, there is an optimal film thickness where maximum output voltage can be obtained.

There are applications that require voltage bias higher than the maximum output voltage a device can obtain. To break that limitation, let's investigate the situation when two of the voltage bias devices are connected in series, as shown in

the circuit diagram in figure B.3. When the output voltage is stabilized, there will be no current flowing towards the capacitors. We can then write:

$$I_2 = \frac{V_{out} - V_m}{R_2} \tag{B.7}$$

where

$$V_m = I_1 R1 \tag{B.8}$$

Combining equation B.7 and equation B.8,we can get

$$V_{out} = I_1 R1 + I_2 R2 = V_{out1} + V_{out2} \tag{B.9}$$

Therefore, when multiple of these devices are connected together in series, the total voltage will be the sum of all the output voltages. This empowers these devices to be used in applications requiring high voltage biases or different voltage biases on a single chip.

B.2 Fabrication and Testing

HCL dry oxide of different thicknesses is grown on ¡100¿ silicon wafers to be used as the dielectric layer. Oxide on the backside of the wafer is then removed using BOE etch, and Ti/Al films of 10nm and 300nm respectively are evaporated on it to provide the bottom electrode. 40nm thick Al film is deposited on top of the front side oxide as positive electrode. Ni-63 radioactive source with output radioactivity of 1.5mCi is put on top of the positive electrode. The devices are tested in air using Keithley 4200 to measure the output voltage.

The output voltages for devices with oxide thicknesses of 50nm and 120nm are plotted in figure B.4, with output values of 700mv and 1.05 V respectively. It takes about 3 hours for the output voltage to stabilize at the maximum values.

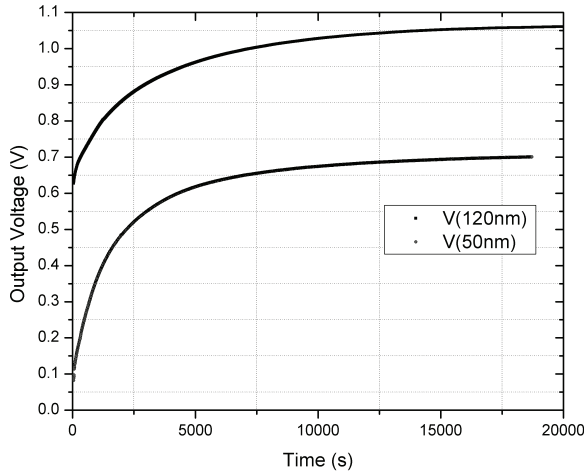

Figure B.4: Output voltage with oxide thicknesses of 50nm and 120nm

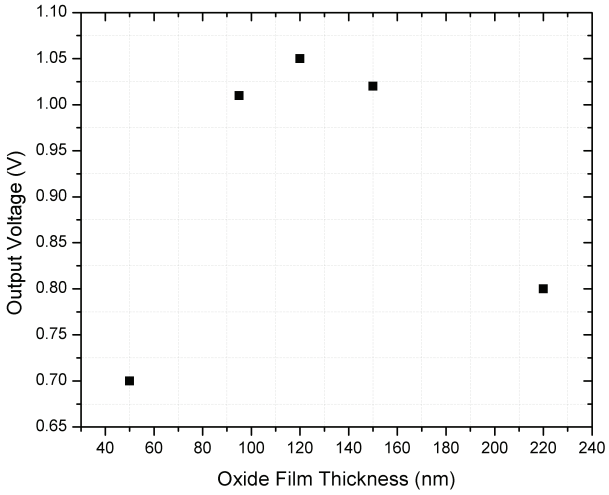

Figure B.5: Output voltage of the radioactive bias with different oxide thickness

The output voltage across the 120nm film is much higher than the voltage across the 50nm one. From equation B.6, there is an optimal thickness for maximum voltage output, so devices with oxide thicknesses of 95nm, 150nm, and 220nm are fabricated and tested with the same radioactive source. The output voltage is plotted against the thickness of the film in Figure B.5. The output voltage is maximizes at 1.05V when oxide thickness is 120nm.

For applications that require voltages above 1.05 volts, equation B.9 shows the voltages will add up if more than one of these devices are connected in series.

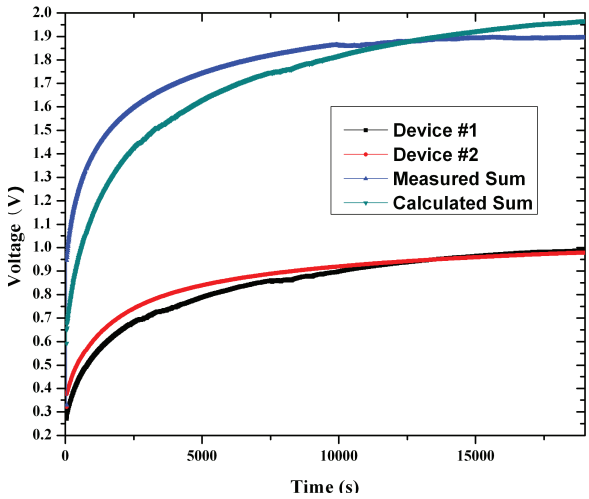

Figure B.6: Output voltage for two devices connected in series

To test the theory, two devices with oxide thicknesses of 120nm are connected in series, and the output voltage is plotted in figure B.6.

The measured output voltage in figure B.6 is very closed to the theoretical output value, which is the voltage sum of the two individual devices. As indicated in equation B.5, the output voltages of our devices are independent of their area. With the devices scaled down to micron sizes, voltages up to hundreds of volts can be achieved in mm^2 area.

To verify the devices in a real circuit, a voltage bias with output voltage of 1.01V is connected to the gate of an nFET transistor as shown in Figure B.7. The drain of the transistor is biased at 5 volts, and the drain current is plotted against time. The drain current levels off at 1.4nA. The transistor is characterized by varying the gate bias voltage, with the output drain-current plotted in Figure B.8. The drain current of 1.4nA measured in figure B.7 corresponds to a gate bias voltage provided of 990mV, which is very closed to the measured voltage of the device, 1.01 volts.

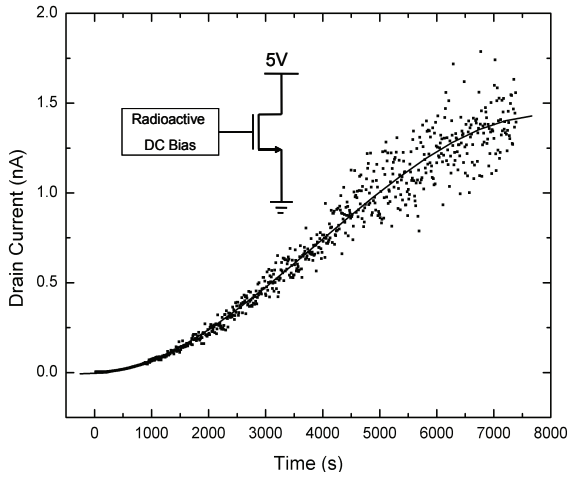

Figure B.7: Output voltage for two devices connected in series

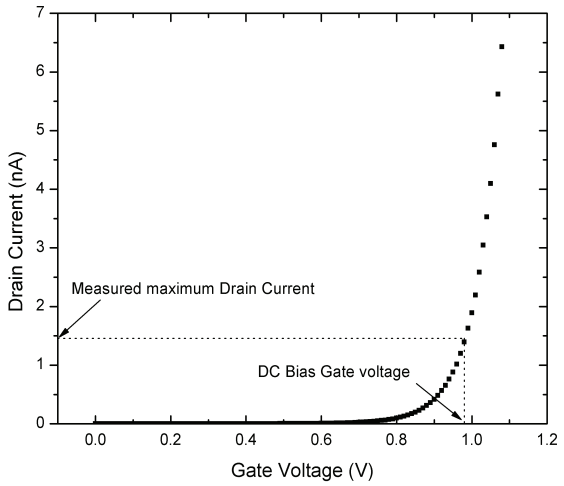

Figure B.8: The V_{gs} -I_d characteristic of the transistor

B.3 Conclusion

As power being one of the major concerns in many sensor applications, in this paper, we have demonstrated a zero active power radioactive powered DC voltage bias device. Together with other power sources we are working on, a sensor node could be totally self-powered for decides without worrying about changing batteries, which is extremely important for remote sensing in harsh environments and implantable devices. ^{63}Ni, a low-energy beta-emitter whose electrons can be stopped by several microns of death skin layer, is used as radioactive source in the device, so the device will not cause any potential environment or health damage. Because the device doesn't require vacuum, and it is scalable, it can be integrated on chip with other sensor devices to reduce the size and cost. Furthermore, the output voltage will add up if multiple devices are connected in series, which makes it suitable for a large range of applications that requires different voltage bias levels.

BIBLIOGRAPHY

[1] R. Duggirala, "Radioisotope thin-film powered,reciprocating electro-mechanical,power generators, zero-power sensors,and 3d betavoltaics," Ph.D. dissertation, Cornell University, 2007.

[2] S. Bonisch, W. Kalkner, and D. Pommerenke, "Modeling of short-gap esd under consideration of different discharge mechanisms," *IEEE Trans. Plasma Sci.*, vol. 31, no. 4, pp. 736–744, 2003.

[3] G. A. Farral, "Electrical breakdown in vacuum," *IEEE Tran. Electrical Insulation*, vol. EI-20, no. 5, pp. 815–841, 1985.

[4] D. Klyachko and D. Chen, "Ordering of c60 on anisotropic surfaces," *Applied Physics Letters*, vol. 75, no. 20, pp. 3693–3696, 1995.

[5] A. C. Fernandez-Pello, "Micropower generation uisng combustion: Issues and approaches," *Proceedings of the Combustion Institute*, vol. 29, pp. 883 – 899, 2002.

[6] G. Harder, *Pocket Guide for Radiological Management.* Perma-Fix Environmental Services, 1999.

[7] R. Szewczyk, E. Osterweil, J. Polastre, M. Hamilton, A. Mainwaring, and D. Estrin, "Habitat monitoring with sensor networks," *Communications of the ACM*, vol. 47, no. 6, pp. 34 – 40, 2004.

[8] K. Martinez, J. Hart, and R. Ong, "Environmental sensor networks," *Computer*, vol. 37, no. 8, pp. 50 – 6, 2004.

[9] J. Lynch and K. Loh, "A summary review of wireless sensors and sensor networks for structural health monitoring," *Shock and Vibration Digest*, vol. 38, no. 2, pp. 91 – 128, 2006.

[10] L. Olsen, "Beta voltaic energy conversion," *Energy Conversion*, vol. 13, no. 4, pp. 117 – 27, 1973.

[11] G. Bloom, K. Murphy, and T. Cox, "An isotope-powered, indwelling intracranial pressure sensor," *Transactions of the American Nuclear Society*, vol. 13, no. 2, pp. 509 – 10, 1970.

[12] A. V. Pattekar and M. V. Kothare, "A microreactor for hydrogen production in micro fuel cell applications," *Journal of Microelectromechanical Systems*, vol. 13, no. 1, pp. 7–18, 2004.

[13] T. Yen, N. Fang, X. Zhang, G. Lu, and C. Wang, "A micro methanol fuel cell operating at near room temperature," *Applied Physics Letters*, vol. 83, no. 19, pp. 4056–4058, 2003.

[14] J. Wainright, R. Savinell, C. Liu, and M. Litt, "Microfabricated fuel cells," *Electrochimica Acta*, vol. 48, pp. 2869–2877, 2003.

[15] A. Epstein and S. Senturia, "Macro power from micro machinery," *Science*, vol. 276, p. 1211, 1997.

[16] H. Cember, *Introduction to health physics*. Pergamon Press, New York, 1983.

[17] S. Littleflower, B. Babu, R. Mukherjee, and B. Baliga, "Inner bremsstrahlung from ^{63}ni," *Journal of Physics G (Nuclear and Particle Physics)*, vol. 16, no. 12, pp. 1873 – 9, 1990.

[18] D. Meier, A. Garnov, J. Robertson, T. Wacharasindhu, and J. Kwon, "Production of 35s for a liquid semiconductor betavoltaic," *Journal of Radioanalytical and Nuclear Chemistry*, 10.1007/s10967-009-0157-9,2009.

[19] D. Sze, A. Hassanein, S. Piet, C. Wong, and W. Bjorndahl, "An assessment of problems associated with tritium containment," vol. 46, New Orleans, LA, USA, 1984, p. 203.

[20] S. Shyamala, G. Udhayakumar, and A. Dash, "Preparation of ^{63}ni electrodeposited special custom-made sources," *BARC Newsletter*, no. 273, pp. 274 – 7, 2006.

[21] S. Roundy, D. Steingart, L. Frechette, P. Wright, and J. Rabaey, "Power sources for wireless sensor networks," in *Proceedings of European Workshop on Wireless Sensor Networks 2004 (EWSN2004)*, Berlin, Germany, 2004, pp. 1–17.

[22] R. Duggirala, S. Tin, and A. Lal, "3d silicon betavoltaics microfabricated using a self-aligned process for 5 milliwatt/cc average, 5 year lifetime microbatteries," in *Proceedings of Transducers 2007*, Lyon, France, 2007, pp. 279–282.

[23] R. Duggirala., A. Polcawich, E. Zakar, M. Dubey, and A. Lal, "Mems radioisotope-powered piezoelectric power generator," in *Proceedings of MEMS 2006*, Istanbul,Turkey, 2006, pp. 94–97.

[24] J. I. Seeger and B. E. Boser, "Charge control of parallel-plate, electrostatic actuators and the tip-in instability," *JMEMS*, vol. 12, no. 5, pp. 656–670, 2003.

[25] L. Castaner and S. D. Senturia, "Speed-energy optimization of electrostatic actuators based on pull-in," *JMEMS*, vol. 8, no. 3, pp. 290–298, 1999.

[26] L. Castaner, J. Pons, R. Nadal-Guardia, and A. Radriguez, "Analysis of the extend operation range of electrostatic actuators by current-pulse drive," *Sensors and Actuators A*, vol. 90, pp. 181–190, 2001.

[27] P. Osmokrovic, N. Arsic, Lazarevic, and N. Z., Kartalovic, "Triggered vacuum and gas spark gaps," *IEEE Transactions on Power Delivery*, vol. 11, no. 2, pp. 858–64, 1996.

[28] Y. Kawada and T. Hosokawa, "Breakdown mechanism of a laser triggered spark gap in a uniform field gap," *Journal of Applied Physics*, vol. 62, no. 6, pp. 2237–42, 1987.

[29] E. Bazelian, *Spark discharge*. Boca Raton: CRC Press, 1998.

[30] H. Golnabi, "The effect of electrical parameters on the simulated spark gap discharge current," *Review of Scientific Instruments*, vol. 73, no. 11, pp. 4014–4021, 2002.

[31] Q. Yuan, S. Liu, and X. Zhang, "The effect of approach speed and charge voltage on an air discharge," *IEEE Trans. Electromagn. Compat.*, vol. 52, no. 4, pp. 985–993, 2010.

[32] K. K., M. S., and F. O., "Influence of electrode surface conditions for the em field radiation in micro gap discharge by the low voltage esd," *Przeglad Elektrotechnizny*, vol. 86, no. 3, pp. 1–4, 2010.

[33] G. Fotis, C. Christodoulou, C. Pippis, and et al., "Measurement of the electromagnetic field radiating by commercial esd generators with the pellegrini target on insulating material," *Measurement*, vol. 42, no. 7, pp. 1073–1081, 2009.

[34] L. Ekonomou, G. Fotis, T. Maris, and et al., "Estimation of the electromagnetic field radiating by electrostatic discharges using artificial neural networks," *Simulation modelling practice and theory*, vol. 15, no. 9, pp. 1089–1102, 2007.

[35] G. Fotis, I. Gonos, and I. Stathopulos, "Measurement of the magnetic field radiating by electrostatic discharges using commercial esd generators," *Measurement*, vol. 39, no. 2, p. 2006, 137-146.

[36] S. Caniggia and F. Maradei, "Numerical prediction and measurement of esd radiated fields by free-space field sensors," *IEEE Trans. Electromagn. Compat.*, vol. 49, no. 3, pp. 494–503, 2007.

[37] "International standard iec 61000-4-2: Electromagnetic compatibility (emc),part 4: Testing and measurement techniques, section 2: Electrostatic discharge immunity test, basic emc publication,," 1995.

[38] P. F. Wilson and M. T. Ma, "Fields radiated by electrostatic discharges," *IEEE Trans. Electromagn. Compat.*, vol. 33, no. 1, pp. 10–18, 1991.

[39] A. Kadish and I. Willam B. Maier, "Electromagnetic radiation from abrupt current changes in electrical discharges," *J. Appl. phys.*, vol. 70, no. 11, pp. 6700–6711, 1991.

[40] M. Masugi, K. Marukawa, N. Kuwabara, and F. Amemiya, "Measurement and analysis of electromagnetic pulses caused by esd," in *IEEE Int. Symp. on EMC*, 1992, pp. 361–365.

[41] O. Fujiwara, "An analytical approach to model indirect effect caused by electrostatic discharge," *IEICE Trans. Commun.*, vol. .E79-B, no. 4, pp. 483–489, 1996.

[42] H. Tomita, "Dependence of current and induced voltage due to spark discharge on gap length," *Electromagnetic Compatibility, 1999 International Symposium on*, pp. 138 – 141, 1999.

[43] S. Bonisch and W. Kalkner, "Influence of the approach speed, charge voltage, and electrode material on the intensity and reproducibility of short gap electrostatic discharge (eds)."

[44] D. Pommerenke, "On the influence of the speed of approach, humidity and arc length on esd breakdown," *Proc. ESD Forum*, p. 103C111, 1993.

[45] D. Ilic, K. Stankovic, M. Vujisic, and P. Osmokrovic, "Avalanche mechanism of vacuum breakdown," *Radiation Effects and Defects in Solids*, vol. 166, no. 2, pp. 137 –149, 2011.

[46] M. Chandrashekhar, C. Thomas, H. Li, M. Spencer, and A. Lal, "Demonstration of a 4h sic betavoltaic cell," *Applied Physics Letters*, vol. 91, no. 5, p. 053551, 2007.

[47] C. Eiting, V. Krishnamoorthy, G. Rodgers, S., R. T., and J. J. D., Brockman, "Demonstration of a radiation resistant, high efficiency sic betavoltaic," *Applied Physics Letters*, vol. 88, no. 6, p. 064101, 2006.

[48] L. Olsen, "Betavoltaic energy conversion," *Energy Conversion*, vol. 13, no. 4, pp. 117–124, 1973.

[49] W. R. Corliss and D. G. Harvey, *Radioisotopic Power Generation*. Englewood Cliffs, New Jersey: Prentice- Hall, Inc, 1964.

[50] D. Linden and T. B. Reddy, *Handbook of Batteries*, 3rd ed. McGraw-Hill Professional, 2002.

[51] W. Sun, N. Kherani, K. Hirschman, L. Gadeken, and P. Fauchet, "A three-dimensional porous silicon p-n diode for betavoltaics and photovoltaics," *Advanced Materials*, vol. 17, no. 10, pp. 1230–1233, 2005.

[52] V. Kaajakari, S. Rodgers, and A. Lal, "Pultrasonically driven surface micromachined motor," in *MEMS 2000*, Miyazaki, Japan, 2000, pp. 40–45.

[53] V. Kaajakari and A. Lal, "Optimization of ultrasonically driven surface micromachined micromotor," in *Ultrasonics Symposium 2001*, Atlanta, 2001, pp. 541–544.

[54] C. Williams and S. Tobias, "Forced undamped non-linear vibrations of imperfect circular discs," *J Mech Eng Sci.*, vol. 5, no. 4, pp. 325–335, 1963.

[55] T. Nayfeh and A. F. Vakakis, "Subharmonic travelling waves in a geometrically non-linear circular plate," *Int. J. Non Lin. Mech.*, vol. 29, no. 2, pp. 233–245, 1994.

[56] L. Girifalco, "Molecular properties of fullerene in the gas and solid phases," *Journal of Physical Chemistry*, vol. 96, no. 2, pp. 858–861, 1992.

[57] F. Bo, "Relationship between the structure of c60 and its lubricity: A review," *Lubrication Science*, vol. 9, no. 2, pp. 181–193, 1997.

[58] R. Morjan, O. Nerushev, M. Sveningsson, F. Rohmund, L. Falk, and E. Campbell, "Growth of carbon nanotubes from c_{60}," *Applied Physics A*, vol. 78, no. 3, pp. 253–261, 2004.

[59] W. Kratschmer, L. D. Lamb, K. Fostiropoulos, and D. R. Huffman, "Solid c_{60}: a new form of carbon," *Nature (London)*, vol. 347, p. 354, 1990.

[60] X. Shi, A. Kortan, J. Williams, A. Kini, B. Savall, and P. Chikin, "Sound velocity and attenuation in single-crystal c60," *Phys. Rev. Lett.*, vol. 68, p. 827, 1992.

[61] S. Hoen, N. Chopra, X.-D. Xiang, R. Mostovoy, J. Hou, W. Vareka, and A. Zettl, "Elastic properties of a van der waals solid: C60," *Physical Review B (Condensed Matter)*, vol. 46, no. 19, pp. 12 737–12 739, 1992.

[62] C. Eom, A. Hebard, L. Trimble, C. G.K., and R. Haddon, "Fabrication and properties of free-standing c_{60} membranes," *Science*, vol. 259, no. 5103, pp. 1887–1890, 1993.

[63] L. Palmetshofer and J. Kastner, "Ion bombardment of c_{60}: Raman study of amorphization and polymerization," *Nuclear Instruments and Methods in Physics Research B*, vol. 96, pp. 343–346, 1995.

[64] V. Kaajakari and L. A., "Parametric excitation of circular micromachined polycrystalline silicon disks," *Applied Physics Letters*, vol. 85, no. 17, pp. 3923–3925, 2004.

[65] K. F. Graff, *Wave Motion in Elastic Solids*. New York: Dover Publications, 1975.

[66] C. Wang, L. Taherabadi, G. Jia, M. Madou, Y. Yeh, and B. Dunnb, "C-mems for the manufacture of 3d microbatteries," *Electrochemical and solid-state letters*, vol. 7, no. 11, pp. A435–A438, 2004.

[67] N. E. Hebert, B. Snyder, R. L. McCreery, W. G. Kuhr, and S. A. Brazill, "Performance of pyrolyzed photoresis carbon films in a microchip capillary electrophoresis device with sinusoidal voltammetric detection," *Anal. Chem*, vol. 75, pp. 4265–4271, 2003.

[68] J. J. Rha, S. C. Kwon, J. R. Cho, W. Y. Shon, and N. Saka, "Creation of ultra-low friction and wear surfaces for micro-devices using carbon films," *Wear*, vol. 259, pp. 765–770, 2005.

[69] S. Ranganathan, R. McCreery, S. Majji, and M. Madou, "Photoresist-derived carbon for microelectrochemical applications," *J. Electrochem. Soc.*, vol. 147, pp. 277–282, 2000.

[70] B. Y. Park, L. Taherabadi, C. Wang, J. Zoval, and M. Madou, "Electrical properties and shrinkage of carbonized photoresist films and the implications for c-mems devices in conductive media," *J. Electrochem. Soc.*, vol. 152, p. J136, 2005.

[71] D. Ranasinghe, D. Lim, S. Devadas, D. Abbott, and P. Cole, "Random numbers from metastability and thermal noise," *ELECTRONICS LETTERS*, vol. 41, no. 16, pp. 13–14, 2005.

[72] R. Brederlow1, R. Prakash, C. Paulus, and R. Thewes, "A low-power true random number generator using random telegraph noise of single oxide-traps," in *ISSCC 2006*, Berlin, Germany, 2006.

[73] B. Sunar, W. Martin, and D. Stinson, "A provably secure true random number generator with built-in tolerance to active attacks," *IEEE Transactions on Computers*, vol. 56, no. 1, pp. 109–119, 2007.

[74] C. Petrie and J. Connelly, "A noise-based ic random number generator for applications in cryptography," *IEEE Trans. Circuits and Systems I*, vol. 47, pp. 615–621, 2000.

[75] S. Kishimoto and M. Fukue, "Generation of physical random digits using diode noise and its statistical properties," *Electronics and Communications in Japan, Part 3 (Fundamental Electronic Science)*, vol. 84, no. 11, pp. 29–36, 2001.

[76] M. Bucci, L. Germani, R. Luzzi, A. Trifiletti, and M. Varanonuovo, "A high-speed oscillator-based truly random number source for cryptographic applications on a smart card ic," *IEEE Trans. Computers*, vol. 52, pp. 403–409, 2003.

[77] G. Emery, "Perturbation of nuclear decay rates," *Annual Review of Nuclear Science*, vol. 22, p. 165, 1972.

[78] J. Berkson, "Do radioactive decay events follow a random poisson-exponential?" *Journal of Applied Radiation and Isotopes*, vol. 26, pp. 543–549.

[79] F. Cannizzaro, G. Greco, S. Rizzo, and E. Sinagra, "Results of the measurements carried out in order to verify the validity of the poisson-exponential distribution in radioactive decay events," *Journal of Applied Radiation and Isotopes*, vol. 29, pp. 649–652.

[80] L. Currie, E. Eijgenhuijsen, and G. Klouda, "On the validity of the poisson hypothesis for low-level countng: Investication of the distributional characteristics of background radiation with the nist individual pulse counting system," *Radiacarbon*, vol. 40, no. 1, pp. 113–127, 1998.

[81] A. Figotin, I. Vitebskiy, V. Popovich, G. Stetsenko, S. Molchanov, A. Gordon, J. Quinn, and N. Stavrakas, "Random number generator based on the spontaneous alpha-decay," *U.S. Patent 10/127,221*, 2003.

[82] C. Vincent, "The generation of truely random binary numbers," *Journal of Physics E: Scientific Instruments*, vol. 3, pp. 594–598, 1970.

[83] A. Alkassar, T. Nicolay, and M. Rohe, "Obtaining true-random binary numbers from a weak radioactive source," in *Computational Science and Its Applications - Proceedings of ICCSA 2005*, Berlin, Germany, 2005, pp. 634–646.